

AN ABSTRACT OF THE DISSERTATION OF

Abdulsalam Mohammed Alhawsawi for the degree of Doctor of Philosophy in Radiation Health Physics presented on September 5, 2017.

Title: Development of a CZT-Silicon Detection System in Support of the Comprehensive Nuclear-Test-Ban Treaty

Abstract approved:

Abi T. Farsoni

The Comprehensive Nuclear-Test-Ban Treaty (CTBT) bans all nuclear explosion tests for military or civilian purposes. The International Monitoring System (IMS) was established to verify compliance with the treaty. It consists of several monitoring stations that detect: seismic activities, hydroacoustic activities, infrasound waves, and radionuclide particles and noble gases. Radioxenon detection provides the most robust evidence of a nuclear weapon test. There are four radioxenon isotopes of interest: ^{131m}Xe ($t_{1/2} = 11.93$ days), ^{133m}Xe ($t_{1/2} = 2.19$ days), ^{133}Xe ($t_{1/2} = 5.25$ days) and ^{135}Xe ($t_{1/2} = 0.38$ days). All of these radioxenons emit beta and gamma radiation in coincidence or conversion electrons and X-rays in coincidence during their decay process.

In this research, a new radioxenon detection system was developed based on Si and CZT detectors. The system is made of the “PIPSBox” silicon gas cell recently developed by Canberra to detect beta and conversion electrons, and two coplanar CZT

detectors to detect X-rays and gamma rays. The PIPSBox silicon gas cell offers many advantages such as: (1) increasing the frequency of air sampling at IMS stations because memory effect does not affect the PIPSBox gas cell like it does with plastic gas cells currently used at IMS stations, (2) reducing the Minimum Detectable Concentration (MDC) for radioxenons due to better energy resolution of silicon, and minimal background interference from previous measurements. The detection system was simulated using MCNP6 and was characterized by ^{131m}Xe to determine optimum operating voltages, proper gain, and the length of the coincidence window.

Pulse waveforms of the silicon and CZT detectors were analyzed using two digital pulse processors: DPP2 and DPP8. DPP2 is a two-channel digital pulse processor with a 200 MHz sampling frequency and a 12-bit ADC resolution. DPP8 is an 8-channel, 125 MHz digital signal processor with a 14-bit ADC resolution. A coincidence firmware was implemented in the on-board FPGA to identify specific coincidences events between silicon and CZT detectors to generate 2D spectra for the four radioxenons of interest.

The resolution of the 129 keV conversion electron was measured to be 16.66% in silicon1 and 16.87% in silicon2. These resolutions are the best-known values reported from other radioxenon detection systems that were included in the literature review of this research.

The minimum detectable concentration (MDC) of PIPSBox/CZT detection system for all radioxenons of interest was measured to be less than the 1 mBq/m³ IMS

requirement. Specifically, 0.25 mBq/m³ for ^{131m}Xe, 0.26 mBq/m³ for ^{133m}Xe, 0.39 mBq/m³ for ¹³³Xe, and 0.72 mBq/m³ for ¹³⁵Xe.

©Copyright by Abdulsalam Mohammed Alhawsawi
September 5, 2017
All Rights Reserved

Development of a CZT-Silicon Detection System in Support of the Comprehensive
Nuclear-Test-Ban Treaty

by
Abdulsalam Mohammed Alhawsawi

A DISSERTATION
Submitted to

Oregon State University

in partial fulfillment of
the requirements for the
degree of

Doctor of Philosophy

Presented September 5, 2017
Commencement June 2018

Doctor of Philosophy dissertation of Abdulsalam Mohammed Alhawsawi presented on September 5, 2017.

APPROVED:

Major Professor, Radiation Health Physics

Head of the School of Nuclear Science and Engineering

Dean of the Graduate School

I understand that my dissertation will become part of the permanent collection of Oregon State University libraries. My signature below authorizes release of my dissertation to any reader upon request.

Abdulsalam Mohammed Alhawsawi, Author

ACKNOWLEDGEMENTS

To my family, thank you for the unconditional support I get from you. I am who I am today because of you.

To my friends, thank you for filling my life with joy and giving me support when I needed it.

To my advisor Dr. Abi Farsoni, thank you for the countless hours you dedicated to help achieve my goal.

To Dr. David Hamby, thank you for always being there when I needed to discuss any aspect of my research.

To my doctoral committee members, Dr. Kenneth Krane, thank you for taking the time to work with me and discuss some of the issues I was facing in my research, Dr. Susan Carozza, thank you for the flexibility you showed throughout my masters and Ph.D., and Dr. Huaping Liu, thank you for helping me with my electrical engineering minor.

Special thank you to my friends and lab mates: Dr. Eric Becker for being there with me through it all. You are a good friend and an exceptional scientist.

Dr. Bemnet Alemayehu for providing the support during my master's years.

Dr. Lily Ranjbar for being a good friend and an expert in radioxenon that I relied on in my research.

Mitch Mannino for all the VHDL discussions. You always listened to my ideas and helped me make them better.

Steve Czyz for helping me with MCNP and allowing me to pick your brain every once and a while.

Harish Gadey for bringing a new perspective to the lab and in my life.

TABLE OF CONTENTS

	<u>Page</u>
1. Introduction.....	1
1.1 Background and Overview	1
1.2 Objective.....	6
2. Literature Review.....	8
2.1 The Comprehensive Nuclear Test-Ban Treaty (CTBT).....	11
2.1.1 Radionuclide Monitoring.....	13
2.1.1.1 Xenon Gas Monitoring.....	13
2.1.2 Available Radioxenon Detection Systems	19
2.1.2.1 The Swedish Automatic Unit for Noble Gas Acquisition (SAUNA)	22
2.1.2.2 Automatic Radioanalyzer for Isotopic Xenon (ARIX).....	27
2.1.2.3 Automated Radioxenon Sampler and Analyzer (ARSA)	30
2.1.2.4 Système de Prélèvement Automatique en Ligne avec l'Analyse du Xénon Atmosphérique (SPALAX).....	35
2.1.2.5 XIA Beta-Gamma Coincidence Phoswich Detector.....	46
2.1.2.6 XIA 24-element Silicon PIN diode detector.....	48
2.1.2.7 Beta-Gamma Coincidence Detectors Developed at OSU.....	51
2.1.2.8 Actively Shielded Phoswich Detector (ASPD).....	52
2.1.2.9 Well-type Actively Shielded Phoswich Detector (WASPD).....	55
2.1.2.10 The Two-Element CZT-Based (TECZT) Radioxenon Detection System	58
2.1.2.11 The CdZnTe, Array of SiPMS, and Plastic Scintillator (CASP) Radioxenon Detection System.....	62
2.1.2.12 Summary of available detection systems Detector	67

TABLE OF CONTENTS (Continued)

	<u>Page</u>
3. Materials and Methods.....	69
3.1 Introduction.....	69
3.2 The PIPSBox/CZT Detection System.....	72
3.2.1 Detector Functionality.....	73
3.3 Detector Simulation.....	74
3.3.1 MCNP Simulations, PTRAC, Expected Coincidence Events.....	74
3.3.1 Simulation Results.....	79
3.3.1.1 ^{131m}Xe	79
3.3.1.1 ^{133m}Xe	80
3.3.1.1 ^{133}Xe	81
3.3.1.1 ^{135}Xe	83
3.3.1.1 Coincidence Detection Efficiency Calculations.....	84
3.4 The 2-Channel Digital Pulse Processor (DPP2.0).....	85
3.5 The 8-Channel Digital Pulse Processor (DPP8.0).....	86
3.5.1 Readout Electronics.....	88
3.5.1.1 Analog Electronics.....	88
3.5.1.2 FPGA Firmware and MATLAB Script.....	89
3.6 Expected Pulse Amplitudes from All Four Detectors.....	94
3.7 Detector Assembly.....	96
4. Results and Discussion.....	99
4.1 Detector Characterization.....	99
4.1.1 CZT Calibration and Detection Parameters.....	99
4.1.2 Silicon Calibration and Detection Parameters.....	106

TABLE OF CONTENTS (Continued)

		<u>Page</u>
4.1.3	CZT and Silicon Spectra in Oscilloscope Free Running Mode using ^{131m}Xe	112
4.1.4	Coincidence Detection Window	115
4.2	Radioxenon Measurements using DPP8	119
4.2.1	^{135}Xe Experimental Results	119
4.2.2	^{133}Xe & ^{133m}Xe Experimental Results	125
4.2.3	^{131m}Xe Experimental Results	134
4.3	Energy Resolution Using DPP8	139
4.4	Radioxenon Measurements Using DPP2.0	140
4.4.1	^{135}Xe Experimental Results Using DPP2.0	140
4.4.2	^{133}Xe and ^{133m}Xe Experimental Results Using DPP2.0	145
4.4.1	^{131m}Xe Experimental Results Using DPP2.0	149
4.5	Energy Resolution Using DPP2	153
4.6	System Background	154
4.7	Minimum Detectable Concentration (MDC)	155
5.	Conclusion	161
6.	Future Work	163
6.1.1	Resolve Coincidence Module Issue with DPP8	163
6.1.2	Electrical Noise Reduction for DPP8	163
6.1.3	Quantification of Memory Effect in the PIPSBox Gas Cell	164
6.1.4	Radioxenon Measurements in Real-Time Using DPP8	164
7.	Bibliography	165
8.	Appendices	171
8.1	PIPSBox Specification Sheet	171

TABLE OF CONTENTS (Continued)

	<u>Page</u>
8.2 PIPSBox with LEMO/BNC Cables	172
8.3 PIPSBox Gas Tube Connections	173

LIST OF FIGURES

<u>Figure</u>	<u>Page</u>
FIGURE 1-1: CURRENT NETWORK OF NOBLE GAS STATION IN THE INTERNATIONAL MONITORING SYSTEM	3
FIGURE 1-2: PROPOSED CZT-SI DETECTION SYSTEM BUILT IN SOLIDWORKS.....	6
FIGURE 2-1: NUCLEAR WEAPON TEST IN 1957, NEVADA USA	8
FIGURE 2-2: ESTIMATED GLOBAL NUCLEAR WARHEAD INVENTORY	9
FIGURE 2-3: DISTRIBUTION OF IMS STATIONS AROUND THE WORLD	13
FIGURE 2-4: SIMPLIFIED DECAY SCHEME OF THE FOUR RADIOXENON OF INTEREST	16
FIGURE 2-5: RADIOXENON DISCRIMINATION BETWEEN A NUCLEAR POWER PLANT RELEASE AND A WEAPON RELEASE BASED ON ACTIVITY RATIOS. THE DASHED REDLINE SEPARATES THE REACTOR DOMAIN (LEFT) FROM THE NUCLEAR TESTING DOMAIN (RIGHT)	18
FIGURE 2-6: SAUNA SAMPLING SYSTEM	22
FIGURE 2-7: SAUNA PROCESSING SYSTEM	23
FIGURE 2-8: SAUNA DETECTION SYSTEM	23
FIGURE 2-9: (A) SAUNA BETA-GAMMA COINCIDENCE SPECTRUM, (B) PROJECTED BETA SPECTRUM, AND (C) PROJECTED GAMMA SPECTRUM. THESE SPECTRA CAME FROM A SAMPLE OF ^{133}Xe AND ^{135}Xe	25
FIGURE 2-10: ARIX AUTOMATED DETECTION SYSTEM UNIT	27
FIGURE 2-11: ARIX RADIOXENON DETECTOR	28
FIGURE 2-12: GATED GAMMA RAY SPECTRUM OF SAMPLE CONTAINING ^{133}Xe AND ^{135}Xe	29
FIGURE 2-13: FIRST ARSA RADIOXENON DETECTION SYSTEM BY PNNL.....	31
FIGURE 2-14: SCHEMATIC OF THE ARSA DETECTION SYSTEM	31
FIGURE 2-15: GENERATED 2-D SPECTRUM FROM THE ARSA SYSTEM	32
FIGURE 2-16: PULSE RISE TIME 2-D SPECTRUM FOR THE ARSA PHOSWICH DETECTOR	34
FIGURE 2-17: SPALAX DETECTION SYSTEM	36

LIST OF FIGURES (Continued)

<u>FIGURE</u>	<u>PAGE</u>
FIGURE 2-18: SCHEMATIC OF THE FULL SPALAX DETECTION SYSTEM	36
FIGURE 2-19. GAMMA SPECTRUM FROM THE SPALAX SYSTEM IN MARSEILLE, FRANCE	37
FIGURE 2-20: SPALAX FIRST BETA-GAMMA COINCIDENCE DETECTION SYSTEM	39
FIGURE 2-21: SPALAX 2-D SPECTRUM COLLECTED AT AN IMS STATION IN OTTAWA, CANADA	40
FIGURE 2-22: GATED GAMMA AND BETA SPECTRA FROM $^{131\text{M}}\text{Xe}$ AND ^{133}Xe	41
FIGURE 2-23: PIPSBOX ON TOP OF THE HPGe DETECTOR	42
FIGURE 2-24: (LEFT) PIPSBOX COUPLED TO THE HPGe DETECTOR, (MIDDLE) SILICON WAFER USED IN THE PIPSBOX, (RIGHT) PIPSBOX DETECTOR.....	43
FIGURE 2-25: (LEFT) CONVERSION ELECTRON ENERGIES MEASURED BY ONE OF THE SILICON DETECTORS, (RIGHT) COINCIDENCE EVENTS BETWEEN THE TWO SILICON DETECTORS FOR A $^{131\text{M}}\text{Xe}$, ^{133}Xe SAMPLE.....	43
FIGURE 2-26: PIPSBOX COUPLED TO TWO HPGe DETECTORS AND A 3M FILTER FOR PARTICLE COLLECTION	44
FIGURE 2-27: PULSE SHAPES GENERATED BY THE PHOSWICH DETECTOR	46
FIGURE 2-28. XIA PHOSWICH DETECTOR 2-D ENERGY SPECTRUM FOR ^{133}Xe SOURCE	47
FIGURE 2-29: DETECTION SYSTEM INSIDE THE ALUMINUM BOX	48
FIGURE 2-30: SIZE OF THE COPPER CUBE	48
FIGURE 2-31: PIN DIODES MOUNTED ON THE CERAMIC HOLDERS	49
FIGURE 2-32: ^{127}Xe 2-D SPECTRUM	49
FIGURE 2-33: GATED SPECTRUM FROM $^{33\text{M}}\text{Xe}$ AND ^{133}Xe USING THE 24-ELEMENT SILICON DETECTORS.....	50
FIGURE 2-34: SCHEMATIC DIAGRAM OF THE ASPD (DIMENSIONS IN MM).....	52
FIGURE 2-35: ASPD ASSEMBLED. SCINTILLATORS ARE WRAPPED IN TEFLON TAPE TO GUIDE THE SCATTERED LIGHT TOWARDS THE PMT	53
FIGURE 2-36. BETA-GAMMA COINCIDENCE ENERGY SPECTRUM USING ^{135}Xe THAT WAS ACTIVATED AT OSU TRIGA REACTOR	53

LIST OF FIGURES (Continued)

<u>FIGURE</u>	<u>PAGE</u>
FIGURE 2-37: SCHEMATIC DIAGRAM OF THE WASPD (DIMENSIONS IN MM)	55
FIGURE 2-38: ASSEMBLED WASPD INSIDE THE PLASTIC HOUSING	56
FIGURE 2-39: BETA-GAMMA COINCIDENCE ENERGY SPECTRUM USING $^{133\text{M}}\text{Xe}$ AND ^{133}Xe THAT WAS ACTIVATED AT OSU TRIGA REACTOR	56
FIGURE 2-40: MDC OF WASPD DETECTION SYSTEM COMPARED TO OTHER BETA-GAMMA DETECTION SYSTEM PROTOTYPES	57
FIGURE 2-41: SCHEMATIC DIAGRAM OF THE TECZT SYSTEM	58
FIGURE 2-42: COPLANAR ANODE ON THE 1 CM X 1 CM X 1 CM CZT CRYSTAL FROM REDLEN TECHNOLOGIES	59
FIGURE 2-43: COMPLETE TECZT SYSTEM	60
FIGURE 2-44: 2-D BETA-GAMMA COINCIDENCE ENERGY SPECTRUM FROM $^{131\text{M}}\text{Xe}$	60
FIGURE 2-45: MDC OF TECZT AND SIX ELEMENT CZT (SECZT) DETECTION SYSTEMS COMPARED TO OTHER BETA-GAMMA DETECTION SYSTEM PROTOTYPES	61
FIGURE 2-46: SCHEMATIC OF THE CASP DETECTION SYSTEM WITH 2 CZT DETECTORS AND THE COINCIDENCE EVENTS OF INTEREST	62
FIGURE 2-47: 3-D CROSS SECTION OF THE CASP PROTOTYPE	63
FIGURE 2-48: CASP DETECTOR INSIDE AN ALUMINUM BOX WITH PREAMPLIFIERS AND OTHER ELECTRONICS	63
FIGURE 2-49: CASP 2-D SPECTRUM FROM ^{135}Xe	64
FIGURE 2-50: GATED GAMMA AND BETA SPECTRA FROM ^{135}Xe	65
FIGURE 2-51: MDC CALCULATION FOR THE CASP PROTOTYPE AND ESTIMATION FOR THE 4 CZT CASP	65
FIGURE 3-1: FINAL DETECTOR ASSEMBLY SHOWING CZT CRYSTALS COUPLED TO THE PIPSBOX GAS CELL	72
FIGURE 3-2: 3-D CROSS SECTION OF THE PIPSBOX/CZT DETECTOR	73
FIGURE 3-3: PIPSBOX/CZT COINCIDENCE SCENARIOS (WITH DETECTOR DIMENSIONS; NOT SCALED)	74
FIGURE 3-4: PIPSBOX SCHEMATIC OBTAINED FROM THE MANUFACTURER WITH ACTUAL DIMENSIONS TO BE USED IN MCNP MODELING	75

LIST OF FIGURES (Continued)

<u>FIGURE</u>	<u>PAGE</u>
FIGURE 3-5: SIMULATED BETA-GAMMA COINCIDENCE EVENTS FOR $^{131\text{M}}\text{Xe}$	80
FIGURE 3-6: SIMULATED BETA-GAMMA COINCIDENCE EVENTS FOR $^{133\text{M}}\text{Xe}$	81
FIGURE 3-7: SIMULATED BETA-GAMMA COINCIDENCE EVENTS FOR ^{133}Xe	82
FIGURE 3-8: SIMULATED BETA-GAMMA COINCIDENCE EVENTS FOR ^{133}Xe AND $^{133\text{M}}\text{Xe}$	83
FIGURE 3-9: SIMULATED BETA-GAMMA COINCIDENCE EVENTS FOR ^{135}Xe	84
FIGURE 3-10: FPGA-BASED DIGITAL PULSE PROCESSOR DPP2.0 WITH 200 MHZ SAMPLING FREQUENCY DEVELOPED AT OSU [66].....	86
FIGURE 3-11: DPP8 WITH THE ANALOG TO DIGITAL CONVERTING BOARD (LEFT) AND THE FPGA BOARD (RIGHT)	87
FIGURE 3-12: DIAGRAM OF THE DPP8 BASIC FIRMWARE ARCHITECTURE	87
FIGURE 3-13. BLOCK DIAGRAM OF THE REQUIRED ELECTRONICS TO READ ONE COPLANAR CZT DETECTOR USED IN THIS RESEARCH, SAME IN RANJBAR ET AL. WORK[66].....	88
FIGURE 3-14: HIGH-LEVEL FLOW CHART OF THE MATLAB SCRIPT USED TO TRANSFER PULSES FROM THE FPGA.....	91
FIGURE 3-15: COINCIDENCE STATE MACHINE INSIDE THE FIRMWARE	92
FIGURE 3-16: PIPSBox/CZT DETECTION SYSTEM AND READOUT ELECTRONICS INSIDE THE ALUMINUM BOX	97
FIGURE 3-17: PIPSBox/CZT INSIDE THE ALUMINUM BOX (CZT1 SIDE).....	98
FIGURE 3-18: PIPSBox/CZT INSIDE THE ALUMINUM BOX (CZT2 SIDE).....	98
FIGURE 4-1: TRIANGULAR FILTER RESPONSE TO A NaI(TL) PULSE WITH 20 NSEC PEAKING TIME IN RED 50 NSEC PEAKING TIME IN BLACK. THE FILTER RESPONSE IS GREATER TO THE SAME PULSE AMPLITUDE WITH A LONGER PEAKING TIME [RHP 537, DIGITAL RADIATION MEASUREMENT AND SPECTROSCOPY, OREGON STATE UNIVERSITY, DR. ABI FARSONI]	101
FIGURE 4-2: ^{137}Cs SPECTRUM WITH AN ASYMMETRIC 30 KEV PEAK	102
FIGURE 4-3: ^{137}Cs SPECTRUM WITH A SYMMETRIC 30 KEV PEAK	103
FIGURE 4-4: ENERGY RESOLUTION AT DIFFERENT TRAPEZOIDAL FILTER FLAT TOP TIMES FOR CZT1 (LEFT) AND CZT2 (RIGHT); PEAKING TIME = 200 SAMPLES (SAMPLING FREQUENCY = 125 MHZ, = 8 NS PERIOD)	104

LIST OF FIGURES (Continued)

<u>FIGURE</u>	<u>PAGE</u>
FIGURE 4-5: ENERGY RESOLUTION AT DIFFERENT TRAPEZOIDAL FILTER PEAKING TIMES FOR CZT1 (LEFT) AND CZT2 (RIGHT); FLAT TOP TIME = 90 SAMPLES (SAMPLING FREQUENCY = 125 MHz, = 8 NS PERIOD)	105
FIGURE 4-6: PEAK CENTROID AT DIFFERENT TRAPEZOIDAL FILTER FLAT TOP TIMES FOR CZT1 (LEFT) AND CZT2 (RIGHT); PEAKING TIME = 200 SAMPLES (SAMPLING FREQUENCY = 125 MHz, = 8 NS PERIOD)	105
FIGURE 4-7: PEAK CENTROID AT DIFFERENT TRAPEZOIDAL FILTER PEAKING TIMES FOR CZT1 (LEFT) AND CZT2 (RIGHT); FLAT TOP TIME = 90 SAMPLES (SAMPLING FREQUENCY = 125 MHz, = 8 NS PERIOD)	105
FIGURE 4-8: ENERGY RESOLUTION FOR CZT1(LEFT) AND CZT2 (RIGHT) AT DIFFERENT GAIN VALUES	106
FIGURE 4-9: AMPLIFICATION CIRCUIT CONNECTED TO THE SILICON DETECTORS OUTPUT	109
FIGURE 4-10: SILICON1 RESPONSE TO ^{131m}Xe WITH AN 800 NS TRAPEZOIDAL PEAKING TIME (LEFT) AND 8 μs TRAPEZOIDAL PEAKING TIME (RIGHT) AND A 1.2 μs FLAT TOP TIME IN BOTH SPECTRA	111
FIGURE 4-11 SILICON2 RESPONSE TO ^{131m}Xe WITH AN 800 NS TRAPEZOIDAL PEAKING TIME (LEFT) AND 8 μs TRAPEZOIDAL PEAKING TIME (RIGHT) AND A 1.2 μs FLAT TOP TIME IN BOTH SPECTRA	111
FIGURE 4-12: ^{131m}Xe GAMMA/X-RAY SPECTRA GENERATED BY THE CZT DETECTORS IN FREE RUNNING MODE	113
FIGURE 4-13: ^{131m}Xe BETA/CONVERSION ELECTRON SPECTRA GENERATED BY THE SILICON DETECTORS IN FREE RUNNING MODE.....	114
FIGURE 4-14: ENHANCED ^{131m}Xe BETA/CONVERSION ELECTRON SPECTRA GENERATED BY THE SILICON DETECTORS IN FREE RUNNING MODE	115
FIGURE 4-15: COINCIDENCE WINDOW DETERMINATION FOR A 1cm^3 CUBE COPLANAR CZT DETECTOR USING A ^{60}Co SOURCE USING DPP8	117
FIGURE 4-16: COINCIDENCE WINDOW DETERMINATION FOR A 1cm^3 CUBE COPLANAR CZT DETECTOR USING A ^{60}Co SOURCE USING DPP2	117
FIGURE 4-17: GAMMA SPECTRA FROM CZT1 (LEFT) AND CZT2 (RIGHT) GENERATED BY ^{135}Xe IN FREE RUNNING MODE .	120
FIGURE 4-18: BETA SPECTRA FROM SILICON1 (LEFT) AND SILICON2 (RIGHT) GENERATED BY ^{135}Xe IN FREE RUNNING MODE	121

LIST OF FIGURES (Continued)

<u>FIGURE</u>	<u>PAGE</u>
FIGURE 4-19: 2-D COINCIDENCE EVENTS FROM ^{135}Xe GENERATED BY THE PIPSBOX/CZT DETECTION SYSTEM	122
FIGURE 4-20: GAMMA EVENTS FROM CZT1 (LEFT) AND CZT2 (RIGHT) GENERATED BY ^{135}Xe IN COINCIDENCE MODE	123
FIGURE 4-21: BETA EVENTS FROM SILICON1 (LEFT) AND SILICON2 (RIGHT) GENERATED BY ^{135}Xe IN COINCIDENCE MODE	124
FIGURE 4-22: TOTAL GAMMA EVENTS FROM CZT1 AND CZT2 GENERATED BY ^{135}Xe IN COINCIDENCE MODE	125
FIGURE 4-23: TOTAL GAMMA EVENTS FROM SILICON1 AND SILICON2 GENERATED BY ^{135}Xe IN COINCIDENCE MODE.....	125
FIGURE 4-24: GAMMA SPECTRA FROM CZT1 (LEFT) AND CZT2 (RIGHT) GENERATED BY ^{133}Xe AND $^{133\text{M}}\text{Xe}$ IN FREE RUNNING MODE.....	126
FIGURE 4-25: BETA SPECTRA FROM SILICON1 (LEFT) AND SILICON2 (RIGHT) GENERATED BY ^{133}Xe AND $^{133\text{M}}\text{Xe}$ IN FREE RUNNING MODE	127
FIGURE 4-26: 2-D COINCIDENCE EVENTS FROM ^{133}Xe AND $^{133\text{M}}\text{Xe}$ GENERATED BY THE PIPSBOX/CZT DETECTION SYSTEM	128
FIGURE 4-27: GAMMA EVENTS FROM CZT1 (LEFT) AND CZT2 (RIGHT) GENERATED BY ^{133}Xe AND $^{133\text{M}}\text{Xe}$ IN COINCIDENCE MODE.....	130
FIGURE 4-28: BETA EVENTS FROM SILICON1 (LEFT) AND SILICON2 (RIGHT) GENERATED BY ^{133}Xe AND $^{133\text{M}}\text{Xe}$ IN COINCIDENCE MODE	130
FIGURE 4-29: TOTAL GAMMA EVENTS FROM CZT1 AND CZT2 GENERATED BY ^{133}Xe AND $^{133\text{M}}\text{Xe}$ IN COINCIDENCE MODE	131
FIGURE 4-30: TOTAL BETA EVENTS FROM SILICON1 AND SILICON2 GENERATED BY ^{133}Xe AND $^{133\text{M}}\text{Xe}$ IN COINCIDENCE MODE	132
FIGURE 4-31: 2-D TRIPLE COINCIDENCE EVENTS FROM ^{133}Xe AND $^{133\text{M}}\text{Xe}$ GENERATED BY THE PIPSBOX/CZT DETECTION SYSTEM.....	133
FIGURE 4-32: GAMMA SPECTRA FROM CZT1 (LEFT) AND CZT2 (RIGHT) GENERATED BY $^{131\text{M}}\text{Xe}$ IN FREE RUNNING MODE	134
FIGURE 4-33: BETA SPECTRA FROM SILICON1 (LEFT) AND SILICON2 (RIGHT) GENERATED BY $^{131\text{M}}\text{Xe}$ IN FREE RUNNING MODE	135

LIST OF FIGURES (Continued)

<u>FIGURE</u>	<u>PAGE</u>
FIGURE 4-34: 2-D COINCIDENCE EVENTS FROM $^{131\text{M}}\text{Xe}$ GENERATED BY THE PIPSBOX/CZT DETECTION SYSTEM.....	136
FIGURE 4-35: GAMMA EVENTS FROM CZT1 (LEFT) AND CZT2 (RIGHT) GENERATED BY $^{131\text{M}}\text{Xe}$ IN COINCIDENCE MODE ..	136
FIGURE 4-36: BETA EVENTS FROM SILICON1 (LEFT) AND SILICON2 (RIGHT) GENERATED BY $^{131\text{M}}\text{Xe}$ IN COINCIDENCE MODE	137
FIGURE 4-37: TOTAL GAMMA EVENTS FROM CZT1 AND CZT2 GENERATED $^{131\text{M}}\text{Xe}$ IN COINCIDENCE MODE.....	137
FIGURE 4-38: TOTAL BETA EVENTS FROM CZT1 AND CZT2 GENERATED $^{131\text{M}}\text{Xe}$ IN COINCIDENCE MODE	138
FIGURE 4-39: GAMMA SPECTRUM FROM CZT1 GENERATED BY ^{135}Xe IN FREE RUNNING MODE	141
FIGURE 4-40: BETA SPECTRA FROM SILICON1 GENERATED BY ^{135}Xe IN FREE RUNNING MODE	142
FIGURE 4-41: 2-D COINCIDENCE EVENTS FROM ^{135}Xe GENERATED BY THE PIPSBOX/CZT DETECTION SYSTEM USING DPP2.0	143
FIGURE 4-42 : COINCIDENCE GAMMA SPECTRUM FROM CZT1 GENERATED BY ^{135}Xe USING DPP2.....	144
FIGURE 4-43: COINCIDENCE BETA SPECTRUM FROM SILICON1 GENERATED BY ^{135}Xe USING DPP2	144
FIGURE 4-44: GAMMA SPECTRUM FROM CZT1 GENERATED BY ^{133}Xe AND $^{133\text{M}}\text{Xe}$ IN FREE RUNNING MODE.....	145
FIGURE 4-45: BETA SPECTRUM FROM SILICON1 GENERATED BY ^{133}Xe AND $^{133\text{M}}\text{Xe}$ IN FREE RUNNING MODE	146
FIGURE 4-46: 2-D COINCIDENCE EVENTS FROM ^{133}Xe AND $^{133\text{M}}\text{Xe}$ GENERATED BY THE PIPSBOX/CZT DETECTION SYSTEM USING DPP2.0	147
FIGURE 4-47: COINCIDENCE GAMMA SPECTRUM FROM CZT1 GENERATED BY ^{133}Xe AND $^{133\text{M}}\text{Xe}$ USING DPP2	148
FIGURE 4-48: COINCIDENCE BETA SPECTRUM FROM SILICON1 GENERATED BY ^{133}Xe AND $^{133\text{M}}\text{Xe}$ USING DPP2	148
FIGURE 4-49: GAMMA SPECTRUM FROM CZT1 GENERATED BY $^{131\text{M}}\text{Xe}$ IN FREE RUNNING MODE.....	149
FIGURE 4-50: BETA SPECTRUM FROM SILICON1 GENERATED BY $^{131\text{M}}\text{Xe}$ IN FREE RUNNING MODE.....	150
FIGURE 4-51: 2-D COINCIDENCE EVENTS FROM $^{131\text{M}}\text{Xe}$ GENERATED BY THE PIPSBOX/CZT DETECTION SYSTEM USING DPP2.0	151
FIGURE 4-52: COINCIDENCE GAMMA SPECTRUM FROM CZT1 GENERATED BY $^{131\text{M}}\text{Xe}$ USING DPP2.....	152
FIGURE 4-53: COINCIDENCE BETA SPECTRUM FROM SILICON1 GENERATED BY $^{131\text{M}}\text{Xe}$ USING DPP2.....	152

LIST OF FIGURES (Continued)

<u>FIGURE</u>	<u>PAGE</u>
FIGURE 4-54: 2-D BACKGROUND SPECTRUM GENERATED FROM THE PIPSBOX/CZT DETECTION SYSTEM OVER 48 HOURS	154
FIGURE 4-55: COMPARISON OF MDC FOR THE CZT-PIPSBOX AGAINST CURRENT OSU AND IMS DETECTION SYSTEMS.	160

LIST OF TABLES

<u>Table</u>	<u>Page</u>
TABLE 2-1: GLOBAL NUCLEAR WEAPONS INVENTORY, 1945-2010	10
TABLE 2-2: CHARACTERISTIC ENERGIES OF THE DECAY OF THE RELEVANT RADIOXENON IN ADDITION TO RADON DAUGHTERS	15
TABLE 2-3: MINIMUM REQUIREMENTS FOR DETECTION SYSTEMS AT RADIONUCLIDE IMS STATIONS	21
TABLE 2-4: MDC RESULTS OBTAINED BY THE SAUNA SYSTEM	26
TABLE 2-5: ENERGY RESOLUTION FOR GAMMA AND X-RAYS FROM ALL FOUR RADIOXENONS FOR CASP AND OTHER DETECTION SYSTEMS.....	66
TABLE 2-6: SUMMARY OF DISCUSSED DETECTION SYSTEMS WITH MDC RESULTS	67
TABLE 3-1: DESCRIPTION OF MCNP FILES USED TO SIMULATE THE CZT-PIPSBOX DETECTOR.....	76
TABLE 3-2: COINCIDENCE SCENARIOS FOR ALL RADIOXENONS OF INTEREST.....	78
TABLE 3-3: ENERGIES OF THE CHARACTERISTIC X-RAYS AND K EDGES OF Cd, Zn, AND Te	80
TABLE 3-4: SIMULATED COINCIDENCE DETECTION EFFICIENCY FOR THE PIPSBOX/CZT SYSTEM.....	85
TABLE 3-5. EXPECTED AMPLITUDES FROM INCIDENT RADIATION ON THE SILICON AND CZT DETECTORS.....	95
TABLE 4-1: ENERGY RESOLUTION OF PHOTONS IN THE PIPSBOX/CZT DETECTION SYSTEM USING DPP8	139
TABLE 4-2: ENERGY RESOLUTION OF CONVERSION ELECTRONS IN THE PIPSBOX/CZT DETECTION SYSTEM USING DPP8 .	139
TABLE 4-3: ENERGY RESOLUTION OF THE PIPSBOX/CZT DETECTION SYSTEM USING DPP2	153
TABLE 4-4: CALCULATED MDC VALUES FOR THE CZT-PIPSBOX DETECTION SYSTEM (1x1x1 cm ³ CZT).....	158
TABLE 4-5: CALCULATED MDC VALUES FOR THE CZT-PIPSBOX DETECTION SYSTEM (3.46 x 3.46 x 1 cm ³ CZT).....	159

1. Introduction

1.1 Background and Overview

In September of 1996, the United Nations General Assembly voted in favor of the Comprehensive Nuclear-Test-Ban Treaty (CTBT), which bans all nuclear explosion tests for military or civilian purposes. The goal of the treaty was to make it more challenging and difficult for countries that don't have nuclear weapons to develop them, or for countries that have nuclear weapons to develop new ones or improve the ones they have. The treaty consists of three pillars: (1) the International Data Center, (2) on-site inspections, and (3) advancing tsunami warning centers. The Comprehensive Nuclear-Test-Ban Treaty has a unique verification comprehensive regime to detect nuclear explosions. This includes detecting underground tests, underwater tests, tests in the atmosphere, and tests on the earth's surface. The International Monitoring System (IMS) was established to verify compliance with the treaty. It consists of monitoring stations that detect: seismic activities, hydroacoustic activities, infrasound waves, and radionuclide particles and noble gases. There are 80 radionuclide stations, half of which are designated to measure and detect noble gases [1], [2]. Figure 1-1 shows existing noble gas stations that are part of IMS.

Currently, there are three main detection systems installed in radionuclide noble gas stations: SAUNA, ARIX, and SPALAX. These systems are used to detect xenon gas (radioxenon), which is released to the atmosphere following a nuclear weapon detonation. Radioxenon is also released from other civilian sites such as nuclear power

plants and medical isotope generators. The amount of radionuclide background in areas that have large number of nuclear reactors and isotope generators like Europe and North America is 3 to 10 mBq/m³ [3]. Radionuclide releases from underground weapon tests are much less than that. Thus, detection systems must be able to quantify very small amounts of radionuclide in the atmosphere to discriminate between the sources of release. The sensitivity threshold for any detection system to be considered for installation in IMS stations is called the Minimum Detectable Concentration (MDC).

The MDC value should be less than 1 mBq/m³. To understand how small this amount is, it is equivalent to detecting a concentration of 0.1 g of radionuclide uniformly distributed within the Earth's atmosphere [4]. Current detection systems that meet this criterion are: The Swedish Automatic Unit for Noble Gas Acquisition (SAUNA) [5], the Russian Analyzer of Xenon Radioisotopes (ARIX) [6], and the French Système de Prélèvements et d'Analyse en Ligne d'Air pour quantifier le Xénon (SPALAX) [7]. The SAUNA and ARIX system use beta-gamma coincidence technique to quantify the amount of radionuclide in the atmosphere. The French SPALAX system utilizes high resolution gamma spectroscopy using high-purity germanium detectors (HPGe's) but have recently developed two detection systems that utilize beta-gamma coincidence technique [8], [9].

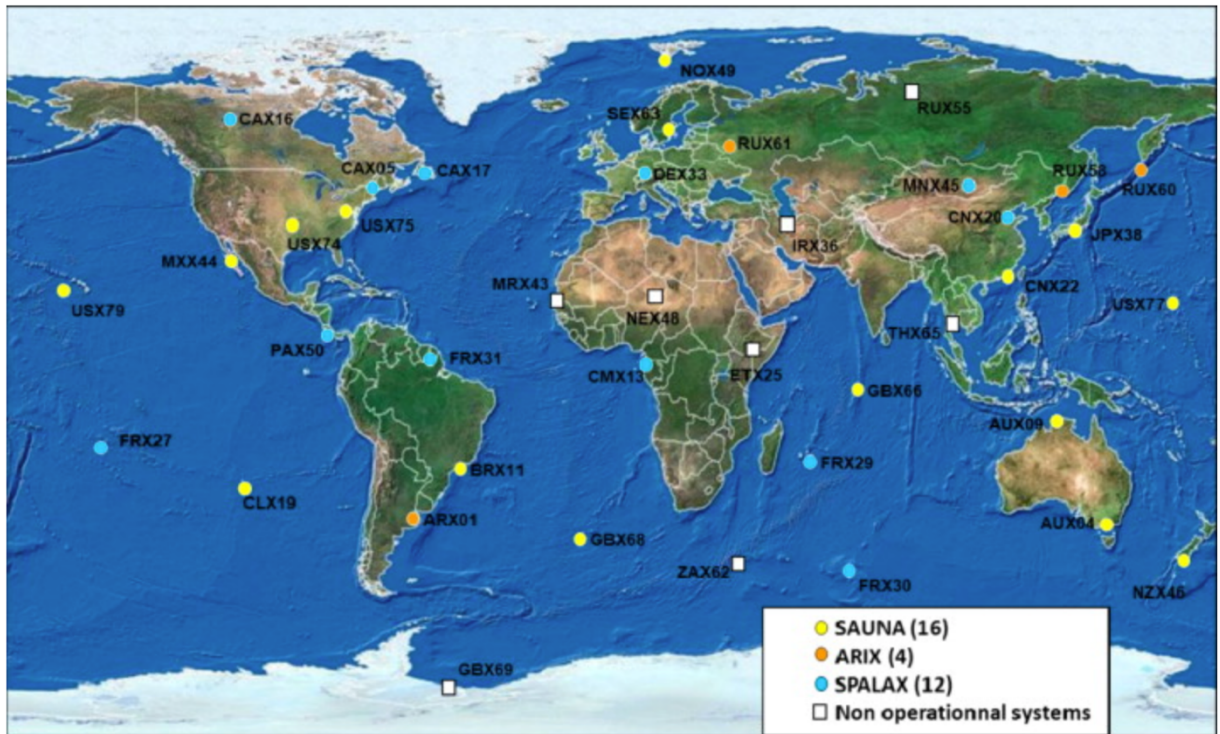


Figure 1-1: Current network of noble gas station in the International Monitoring System

The development of ultra-sensitive detection systems is essential for the success of radionuclide monitoring stations to support IMS. Most of the detectors recently under development are based on beta-gamma coincidence technique. The United States of America developed The Automated radioxenon Sampler and Analyzer (ARSA), which is based on beta-gamma coincidence. The ARSA system was developed at Pacific Northwest National Laboratory (PNNL) and is installed there on site. It has not been installed yet in IMS radionuclide monitoring stations but it's being tested at some IMS locations. The three main systems cited earlier are capable of detecting radioxenon releases and have been tested in recent years.

In 2006, the Democratic People's Republic of Korea conducted an underground nuclear weapon test that was detected by IMS stations. Three more tests were conducted by North Korea in 2010, 2013, and 2016. All these tests were detected by IMS radionuclide stations [10]–[19]. Radioxenon releases from the Fukushima accident site in Japan in 2011 were detected by the ARSA system at PNNL [20], [21].

Even though detection systems at IMS stations that rely on beta-gamma coincidence technique are capable of quantifying small amounts of radioxenon in the atmosphere, they all suffer from a common problem called the memory effect. Memory effect reduces the sensitivity of detection systems because radioxenon diffuses into gas cells that are made of organic plastic scintillators, which raises the background for subsequent measurements. The current protocol requires radioxenon samples to be flushed from detection systems every 24 hours. Tests are underway to reduce the frequency of vacuuming to 10 hours with an ultimate goal of 8 hours vacuuming, because simulation suggest that this frequency will result in a substantial gain in signal amplitude [8]. Multiple methods have been implemented to solve the memory effect that will be discussed later. The latest was the introduction of a new type of detector/gas cell made of silicon. This detector was developed by Canberra in cooperation with the French Atomic Agency (CEA) in 2013 [8]. It effectively reduced the memory effect to less than 0.05%, which is below CTBT requirement (5%) [9]. The silicon detector was coupled at first to a NaI(Tl) and then to an HPGe. The measured MDC was found to be less than 1 mBq/m^3 [8], [9]. The Radiation Detection Group at Oregon State University have been building phoswich detection systems based on beta-gamma detection

technique since 2007 [22]–[29]. Earlier designs used cylindrical organic plastic scintillators to detect beta particles and conversion electrons, and inorganic scintillators to detect gamma and X-rays. The group then moved to designing well type plastic scintillators that act as both gas cell and beta detectors. Memory effect was an issue with these designs but it was mitigated by depositing a thin layer of AlO_2 on the cylindrical plastic scintillator to reduce the memory effect. Then efforts shifted towards building detection systems based on semiconductor technology. In a novel research study, two CZT detectors were placed in a plastic holder and gas was injected inside a sealed cavity between the detectors [30], [31]. The goal of that design was to take advantage of the excellent energy resolution of semiconductors and operate the system at room-temperature, which will make it easier to be installed and maintained in remote areas. Unfortunately, it was difficult to distinguish between radionuclides because of a backscattering effect that resulted from high-energy beta particles and conversion electrons interacting with the high Z CZT detectors. This research was initiated because of the exceptional performance obtained by CZT detectors in terms of resolution, and as a continuation of utilizing semiconductor technology. Instead of using the CZT to detect both beta and gamma rays, CZT's will be coupled to the latest silicon gas cell made by Canberra, which will be responsible for detecting beta and conversion electrons. Figure 1-2 shows a 3-D model of the proposed detection system built in SolidWorks. It is expected that this detection system will have minimal memory effect and will meet the MDC requirement for CTBT detectors. In addition, the detection

system should have low maintenance requirements when compared to systems with HPGe detectors.

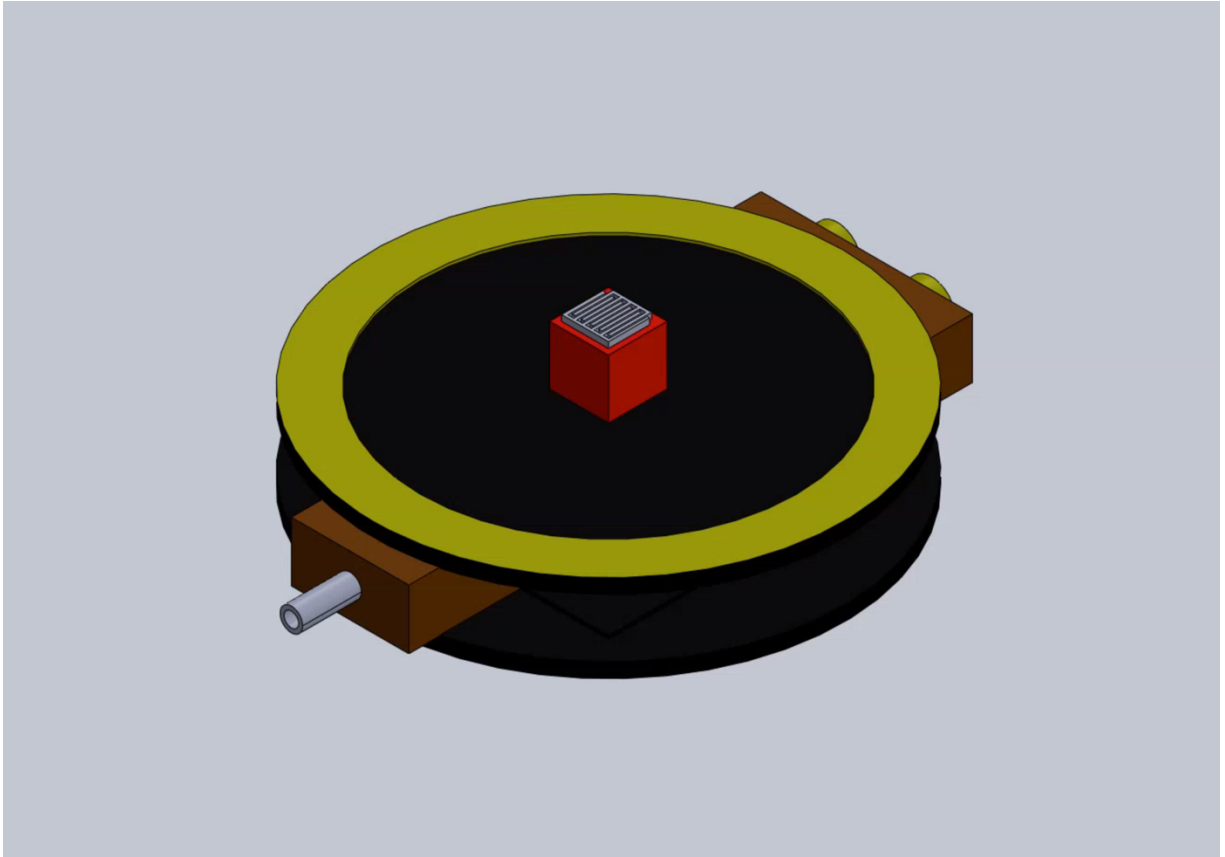


Figure 1-2: Proposed CZT-Si detection system built in SolidWorks

1.2 Objective

The objective of this work is to build, characterize, and test a radiation detection system to monitor radionuclides in the atmosphere using the silicon gas cell detector (PIPSBox) recently developed by Canberra in cooperation with the French Atomic Agency (CEA). The PIPSBox will be coupled to two coplanar CZT detectors and mounted inside an aluminum box to shield it from light and electromagnetic radiation. The detector signals will be processed using two digital signal processors, the newly 8-

channel digital pulse processor (DPP8) under development at Oregon State University (OSU) and a two-channel digital pulse processor (DPP2) that was previously developed and used to with previous radioxenon detectors at OSU.

2. Literature Review

Between 1945 and 1996, over 2000 nuclear tests were carried out by nuclear states. The majority were performed by the United States, an example shown in Figure 2-1, and the Soviet Union [32]. About 500 of these tests were in the atmosphere so there was international concern over radioactive fallout because of these tests. One



Figure 2-1: Nuclear weapon Test in 1957, Nevada USA

atmospheric test carried out by the United States resulted in both civilian and servicemen contamination. Unfortunately, that did not stop nuclear states from testing. Instead, they decided to carry out: high-altitude nuclear testing, underwater testing and underground testing [32]. There was a race between nuclear weapon states on who can stock up more weapons. Table 2-1 shows the global weapon inventory between 1945 and 2010 [33]. The number of nuclear weapons went up to more than 6900 weapons. Talks, agreements and treaties between nuclear states, specifically the U.S. and Russia, aimed at reducing the number of nuclear weapons possessed by nuclear states and preventing new countries from becoming nuclear states [34]. The following list names a few of these agreements: (1) The Strategic Arms Limitation Talks (SALT I and SALT II), (2) The Strategic Arms Reduction Treaty (START I, START II, and START III), (3) The Strategic Offensive Reductions Treaty (SORT or Moscow Treaty), and (4) The

Comprehensive Nuclear-Test-Ban Treaty (CTBT). Fortunately, these negotiations and treaties resulted in tremendous reduction in the number of nuclear weapons over the past two to three decades. Figure 2-2 depicts a recent world map with current nuclear states and the number of weapons they own [35]. This work will focus on mostly on CTBT as its relevant to this research.

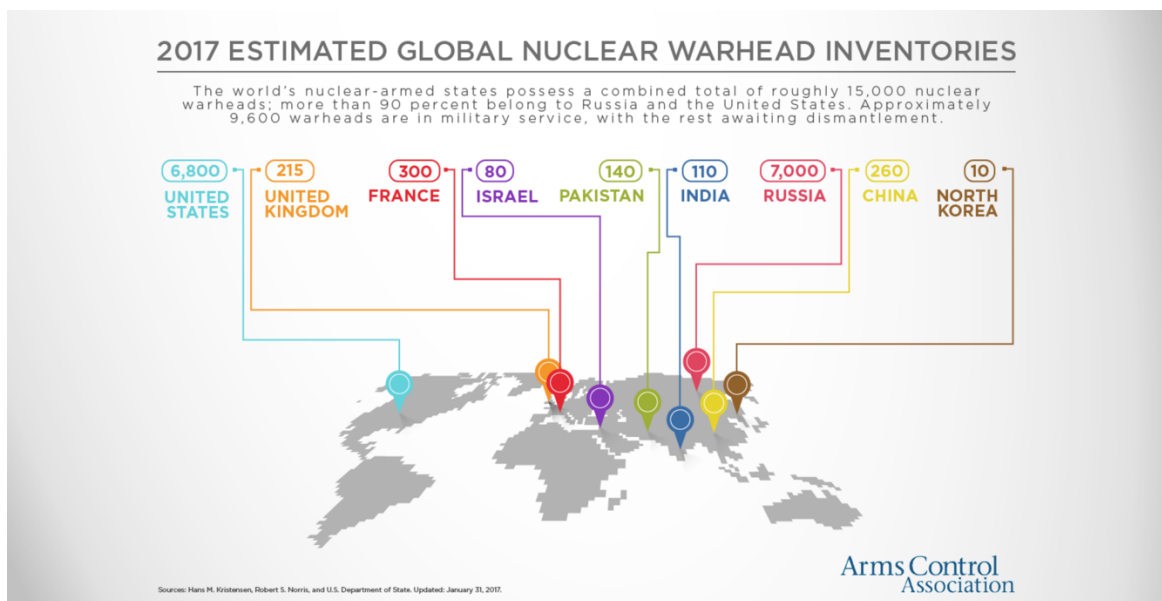


Figure 2-2: Estimated global nuclear warhead inventory

Table 2-1: Global Nuclear Weapons Inventory, 1945-2010

YEAR	UNITED STATES	RUSSIA	UNITED KINGDOM	FRANCE	CHINA	ISRAEL	INDIA	PAKISTAN	TOTAL
1945	2								2
1946	9								9
1947	13								13
1948	50								50
1949	170	1							171
1950	299	5							304
1951	438	25							463
1952	841	50							891
1953	1,169	120	1						1,290
1954	1,703	150	7						1,860
1955	2,422	200	14						2,636
1956	3,692	426	21						4,139
1957	5,543	660	28						6,231
1958	7,345	869	31						8,245
1959	12,298	1,060	35						13,393
1960	18,638	1,605	42						20,285
1961	22,229	2,471	70						24,770
1962	25,540	3,322	288						29,150
1963	28,133	4,238	394						32,765
1964	29,463	5,221	436	4	1				35,125
1965	31,139	6,129	436	32	5				37,741
1966	31,175	7,089	380	36	20				38,700
1967	31,255	8,339	380	36	25	2			40,037
1968	29,561	9,399	394	36	35	4			39,429
1969	27,552	10,538	433	36	50	6			38,615
1970	26,008	11,643	394	36	75	8			38,164
1971	25,830	13,092	309	45	100	11			39,387
1972	26,516	14,478	309	70	130	13			41,516
1973	27,835	15,915	387	116	150	15			44,418
1974	28,537	17,385	457	145	170	17			46,711
1975	27,519	19,055	492	188	180	20			47,454
1976	25,914	21,205	492	212	180	22			48,025
1977	25,542	23,044	492	228	180	24			49,510
1978	24,418	25,393	492	235	190	26			50,754
1979	24,138	27,935	492	235	195	29			53,024
1980	24,104	30,062	492	250	205	31			55,144
1981	23,208	32,049	492	274	225	33			56,281
1982	22,886	33,952	471	274	235	35			57,853
1983	23,305	35,804	450	279	240	38			60,116
1984	23,459	37,431	380	280	249	40			61,839
1985	23,368	39,197	422	360	243	42			63,632
1986	23,317	45,000	422	355	230	44			69,368

1987	23,575	43,000	422	420	230	47			67,694
1988	23,205	41,000	422	410	240	49			65,326
1989	22,217	39,000	422	410	238	51			62,338
1990	21,392	37,000	422	505	232	53			59,604
1991	19,008	35,000	422	540	234	56			55,260
1992	13,708	33,000	422	540	234	58			47,962
1993	11,511	31,000	422	525	234	60			43,752
1994	10,979	29,000	352	510	234	62			41,137
1995	10,904	27,000	422	500	234	63			39,123
1996	11,011	25,000	422	450	234	64			37,181
1997	10,903	23,000	366	450	232	66			35,017
1998	10,732	22,500	281	450	232	68	2	3	34,268
1999	10,685	22,000	281	450	232	70	8	8	33,734
2000	10,577	21,500	281	470	232	72	14	13	33,159
2001	10,526	21,000	281	350	235	74	20	18	32,504
2002	10,457	20,000	281	350	235	76	26	23	31,448
2003	10,027	19,000	281	350	235	78	32	28	30,031
2004	8,570	18,000	281	350	235	80	38	33	27,587
2005	8,360	17,000	281	350	235	80	44	38	26,388
2006	7,853	16,000	281	350	235	80	50	43	24,892
2007	5,709	15,000	225	350	235	80	60	50	21,709
2008	5,273	14,000	225	300	235	80	70	60	20,243
2009	5,113	13,000	225	300	240	80	80	70	19,108
2010	5,000*	12,000	225	300	240	80	80	70	17,995*

2.1 The Comprehensive Nuclear Test-Ban Treaty (CTBT)

The Comprehensive Nuclear-Test-Ban Treaty (CTBT) was negotiated in Geneva between 1994 and 1996. It was a result of multiple efforts during the cold war to ban nuclear tests. About 183 countries signed the treaty including France, the Russian Federation, and the United Kingdom. The Preparatory Commission for the Comprehensive Nuclear-Test-Ban Treaty Organization is based in Vienna, and has an annual budget of around \$130 million [36]. The treaty prohibits nuclear explosion tests for military and peaceful purposes. This includes earth's surface, the atmosphere, underwater, and underground tests. The treaty makes it hard for countries to develop new weapons or test the ones they already have. Additionally, it includes a unique

comprehensive verification regime to detect nuclear explosions. There are three major pillars supporting the treaty: The International Data Center, On-Site Inspection, and helping Tsunami Warning Centers better understand oceans, volcanoes, etc [36]. The International Data Center processes data and distributes it to CTBT members. On-Site Inspection could be initiated in an area, where nuclear explosion is suspected. Studying the data from Tsunami warning centers will provide information about underwater earthquakes and seismic events [36].

Nuclear weapon tests release enormous amounts of energy that affect the surrounding environment of the test location. This includes underground waves that are detected by seismic detectors, hydroacoustic waves that are detected by underwater detectors, infrasound waves that are detected by sound detectors. Another important outcome of a nuclear weapon test are radionuclides and noble gasses. These are detected by radiation and gas detectors. To be able to verify compliance and detect nuclear weapon tests, treaty pillars rely on the information provided by several stations and laboratories distributed all over the world. These facilities are part of the International Monitoring System. There are more than 300 facilities around the world that uses four distinct technologies: (1) seismic monitoring, (2) hydroacoustic monitoring, (3) infrasound monitoring, and (4) radionuclide monitoring [36]. These facilities are strategically distributed globally and are displayed in Figure 2-3 [37]. The next section focuses on radionuclide monitoring; and specifically explains how radionuclide detectors work, and what kind of detectors are currently available.

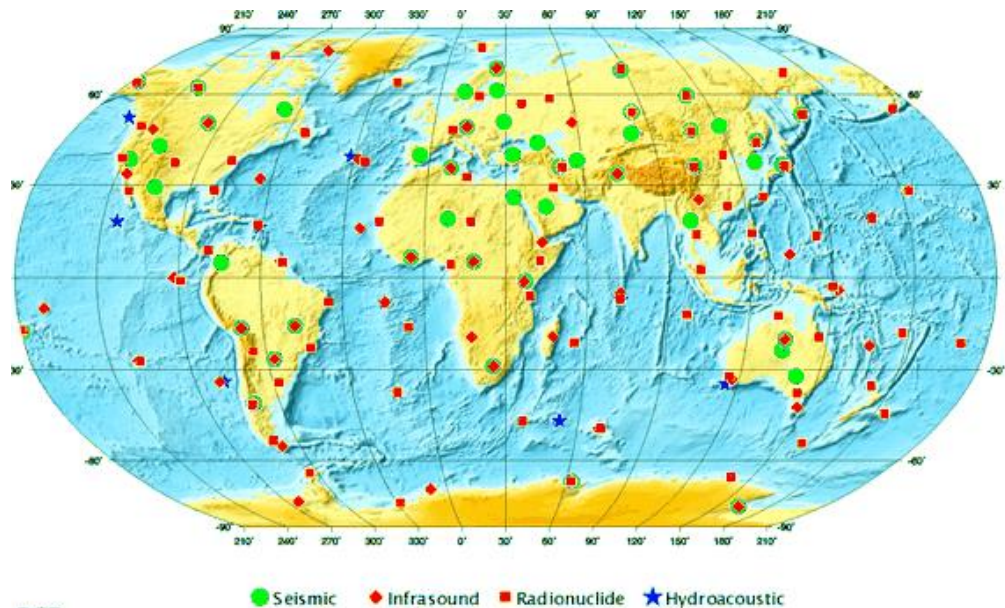


Figure 2-3: Distribution of IMS stations around the world

2.1.1 Radionuclide Monitoring

There are 80 radionuclide stations that specialize in detecting radioactive particulates and noble gases produced from a nuclear explosion. Half the stations are dedicated for radioactive particle measurements and the other half measure noble gases. Noble gas measurements give the most reliable and clear indication that an explosion was nuclear or not. All stations are supported by 16 radionuclide laboratories that provide independent analysis of samples when needed [36].

2.1.1.1 Xenon Gas Monitoring

Nuclear weapons are comprised of special nuclear material such as uranium and plutonium. The fission of these elements results in several isotopes and significant amounts of noble gases. In the case of atmospheric testing, radionuclide stations can

pick up radioactive particles released from the blast. Radioactive noble gases such as xenon and radon are also released and can be measured by radionuclide stations. Therefore, in a perfect scenario, radionuclide stations can pick up both radioactive particles and radioxenon. Countries that are not complying with CTBT started testing their weapons underground to contain and trap radioactive particles. However, they cannot contain noble gasses since they are chemically inert and will escape the test site. The issue here is that nuclear power plants and medical isotope generators also release radioxenon [38]. Nonetheless, radionuclide stations can distinguish between radioxenon resulting from a weapon test and radioxenon released by nuclear power plants and medical isotope generators by measuring the ratios of certain radioxenon isotopes.

There are four radioxenon isotopes that are of interest to distinguish between nuclear weapon testing and nuclear power plants/medical isotopes generators: (1) ^{131m}Xe [$t_{1/2} = 11.93$ days], (2) ^{133m}Xe [$t_{1/2} = 2.19$ days], (3) ^{133}Xe [$t_{1/2} = 5.25$ days] and (4) ^{135}Xe [$t_{1/2} = 0.38$ days [39], [40]. Table 2-2 shows the characteristic energies and decay modes of all four radioxenons. The half-lives of these isotopes are vital because it allows detection systems at IMS stations to identify a weapon test days or even weeks after the incident [41]–[43].

Table 2-2: Characteristic energies of the decay of the relevant radioxenon in addition to radon daughters

	Decay energy (keV)	Branching ratio (%)
^{131m} Xe		
X-rays	29.46	15.4
	29.78	28.6
	33.60	10.2
	34.61	1.85
Gamma rays	163.93	1.95
Conversion electrons	129.4	61
Coincident decays	Sum of 29.46 to 34.61 keV X-rays and 129 keV e ⁻	56.1
¹³³ Xe		
X-rays	30.62	14.1
	30.97	26.2
	35.00	9.4
	36.01	1.7
Gamma rays	80.99	37.0
Conversion electrons	45	55.1
Betas (maximum energy)	346	100
Coincident decays	31.63 keV X-ray + 45 keV e ⁻ + 346 keV beta	48.9
	80.98 keV gamma + 346 keV beta	37.2
^{133m} Xe		
X-rays	29.46	16.1
	29.78	29.8
	33.60	10.6
	34.61	1.9
Gamma rays	233.2	10.0
Conversion electrons	198.7	64
Coincident decays	Sum of 29.46–34.61 keV X-rays and 199 keV e ⁻	58.4
¹³⁵ Xe		
X-rays	30.62	1.45
	30.97	2.69
	35.00	0.97
	36.01	0.185
Gamma rays	249.8	90
	608.2	2.90
Conversion Electrons	214	5.7
Betas (maximum energy)	910	100
Coincident Decays	31.63 keV X-ray + 214 keV e ⁻ + 910 keV beta	5.7
	249.8 gamma + 910 keV beta	90
²¹⁴ Pb		
X-rays	74.82	4.8
	77.11	8.0
	86.83	1.0
	87.35	1.8
	89.78	0.67
	90.07	0.17
Gamma rays	241.95	7.43
	351.95	37.6
²¹⁴ Bi		
X-rays	79.29	0.98

Figure 2-4 shows a simplified decay scheme of all four radioxenons of interest [3].

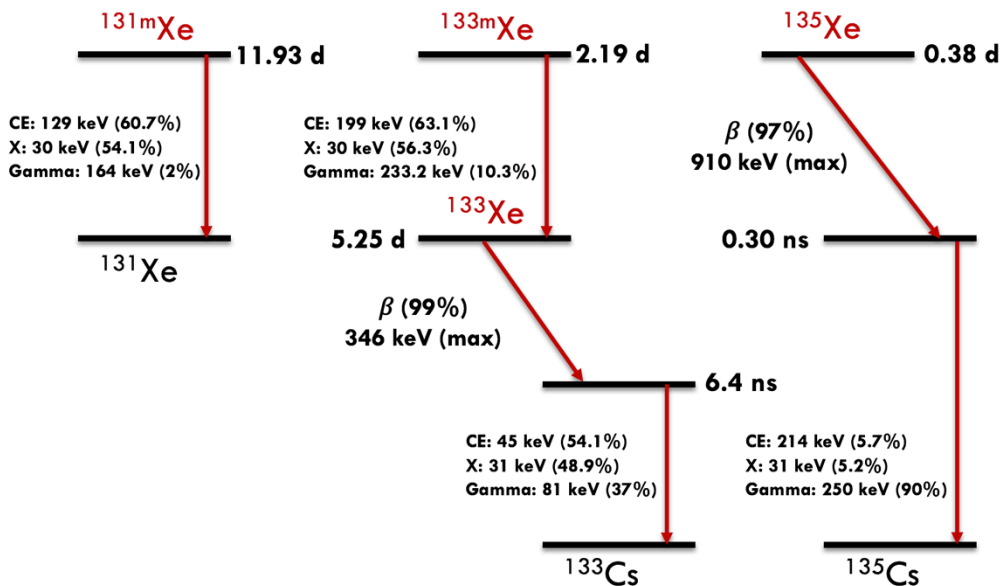


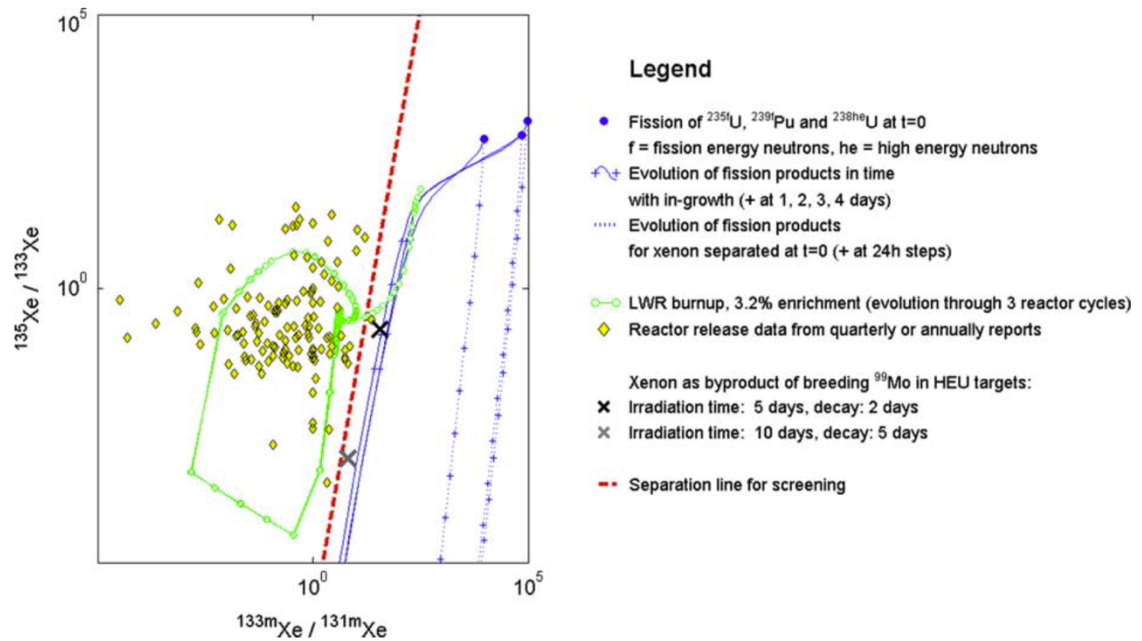
Figure 2-4: Simplified decay scheme of the four Radioxenon of interest

As stated earlier, detecting one of the four relevant radioxenon is not enough to identify a nuclear weapon test. Two ratios are of importance here: ^{133m}Xe to ^{133}Xe and ^{135}Xe to ^{133}Xe . The ratio of $^{133m}\text{Xe}/^{133}\text{Xe}$ is 100 times greater in the case of a weapon test than the ratio generated by nuclear power plants/medical isotopes generators. In the case of the $^{135}\text{Xe}/^{133}\text{Xe}$ ratio, it is 10,000 times greater in the case of a weapon test than the ratio generated by nuclear power plants/medical isotopes generators.

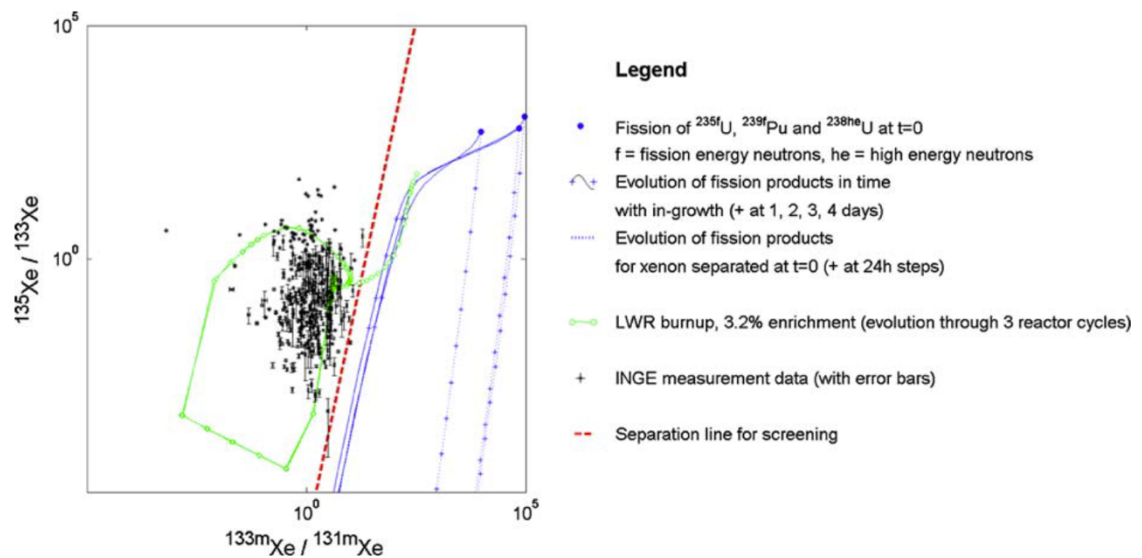
The method of measuring the ratios between radioxenon have been proven effective in the past several years. Stations at the IMS have been able to detect both unusual radioxenon releases from civilian activities and radioxenon releases from weapon tests carried out by rogue states [44], [45]. Figure 2-5 illustrates the distinction between a nuclear power plant release and a nuclear weapon test release [46]. It should be noted that ^{133}Xe is the most dominant isotope from nuclear power plants [38], [47],

[48]. A few examples of successful identification for both civilian and weapon explosions are stated next.

The first example was the detection of high levels of ^{133}Xe following the tragic accident at Fukushima Dai-ichi nuclear power plants in Japan. The ARSA system at Pacific Northwest National Laboratory (PNNL) was able to detect ^{133}Xe releases from the accident site few days after the incident [49].



(a) Based on reactor emission data.



(b) Based on atmospheric detections.

Figure 2-5: Radioxenon discrimination between a nuclear power plant release and a weapon release based on activity ratios. The dashed redline separates the reactor domain (left) from the nuclear testing domain (right)

Stations in China detected the accident release of ^{133}Xe and $^{131\text{m}}\text{Xe}$ approximately two weeks after the incident [21], [50]. Another IMS station in Darwin Australia picked up ^{133}Xe one month after the incident [20].

The second example was detecting radioxenon releases from a nuclear weapon test performed by North Korea. The test was carried out in 2006 and was confirmed by IMS station in South Korea [18]. The test was also confirmed in an IMS station in Canada, which showcased the astonishing capability possessed by detection systems installed at IMS stations to identify compliance with CTBT [11], [17]. Two more tests were performed by North Korea in 2010 and 2013 and both tests were confirmed by several IMS stations [12]–[14], [51]. Detection systems operated at IMS stations showed that it can positively identify changes in radioxenon ratios whether it is high unusual amounts of Radioxenon in the case of Fukushima, or very low amounts in the case of North Korea's underground weapon tests. Several detection systems prototypes have been developed to be considered for installation at IMS stations. The next section describes how these detection systems work and what techniques they rely on.

2.1.2 Available Radioxenon Detection Systems

Several radioxenon detection systems have been developed during the past few years. There are two main techniques these systems rely on: (1) Beta-gamma coincidence technique, (2) High-resolution gamma spectroscopy. The Swedish Automatic Unit for Noble gases (SAUNA), the Automated Radioxenon Sampler and Analyzer (ARSA) Analyzer of Xenon Radioisotopes (ARIX) all use Beta-Gamma

coincidence technique. The French *Système de prélèvements et d'analyse en ligne d'air pour quantifier le xenon (SPLAX)* uses high resolution gamma spectroscopy [6], [52]–[54]. These are the four systems currently installed or being tested at radionuclide stations as shown earlier in Figure 1-1 [55]. More detector prototypes are under development by various institutes around the world to help improve the state of existing technology and build better detection systems to support the efforts of detecting underground nuclear weapon tests. Table 2-3 shows the minimum requirements for detection systems that are to be installed at IMS radionuclide stations. The most important parameter is the Minimum Detectable Concentration (MDC), which determines the system's sensitivity to detect ^{131m}Xe , ^{133m}Xe , ^{133}Xe , and ^{135}Xe and distinguish them from background events. Memory effect is another huge factor in determining the MDC of the system. It also affects the frequency at which the system can flush and reanalyze air samples.

To understand why memory effect is a factor for the detection system installed at IMS stations, we must point out that most of the systems that use beta-gamma coincidence technique utilize organic plastic scintillators as their gas cell and electron detector simultaneously. The issue here is that xenon gas diffuses into the gas cells, which are made of an organic material. radioxenon will remain in the walls of the cell after evacuating the gas, which will affect subsequent measurements by increasing the background level of the system, thus increasing the MDC of the detection system. Increasing the background will interfere with future measurements and degrade the

sensitivity of the detection system. This becomes especially important at IMS stations close to nuclear power plants and medical isotope generators [16], [56].

Table 2-3: Minimum requirements for detection systems at radionuclide IMS stations

Characteristic	Minimum requirement
Air flow	0.4 m ³ /h
Total volume of sample	10 m ³
Collection time	≤ 24 h
Measurement time	≤ 24 h
Time before reporting	≤ 48 h
Reporting frequency	Daily
Isotopes measured	^{131m} Xe, ¹³³ Xe, ^{133m} Xe, ¹³⁵ Xe
Measurement mode	Beta-gamma coincidence or high resolution gamma-ray spectroscopy
Minimum detectable concentration	1 mBq/m ³ for ¹³³ Xe
State-of-health	Status display transmitted to IDC
Communication	Two-way
Data availability	95%
Down time	≤ 7 consecutive days, ≤ 15 days annually

To eliminate memory effect, scientists started making gas cells made of semiconductor detectors, which remarkably reduces the memory effect problem. A few examples of detectors utilizing semiconductor detectors will be discussed in the following section in addition to the three main systems installed currently at IMS stations.

2.1.2.1 The Swedish Automatic Unit for Noble Gas Acquisition (SAUNA)

This system was designed and developed by the Swedish defense research agency (FOI). It is a complete detection system that can be installed at IMS stations and perform: air sampling, sample processing and detecting radioxenon. In other words, it's a complete solution. Air sampling, sample processing and radioxenon detection are performed automatically. The way the system works is it collects air samples and extracts radioxenon, radioxenon is then sampled and purified, and finally radioxenon is counted to identify the xenon isotopes in the sample and the activity of those isotopes. Ultimately, ratios of radioxenon that were mentioned previously will be calculated to determine whether or not it was a weapon test [5]. Figure 2-6, Figure 2-7, and Figure 2-8 shows the sampling system, processing system and the detection system used in SAUNA. The detection system will be described more for the purposes of this document.

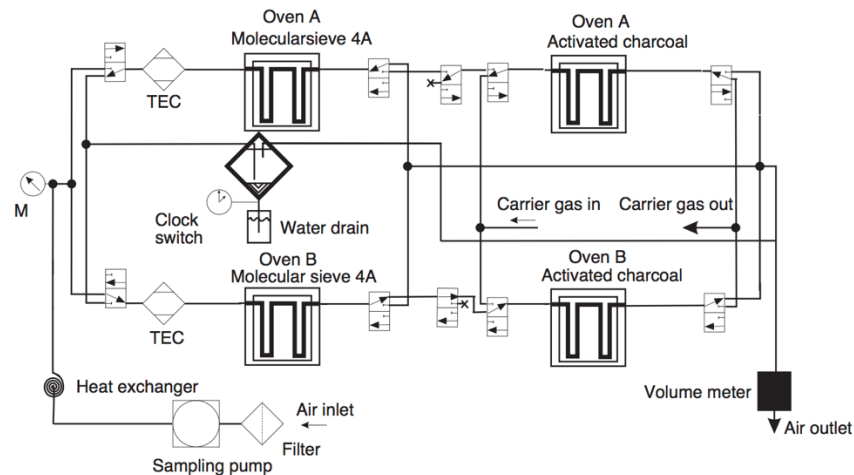


Figure 2-6: SAUNA sampling system

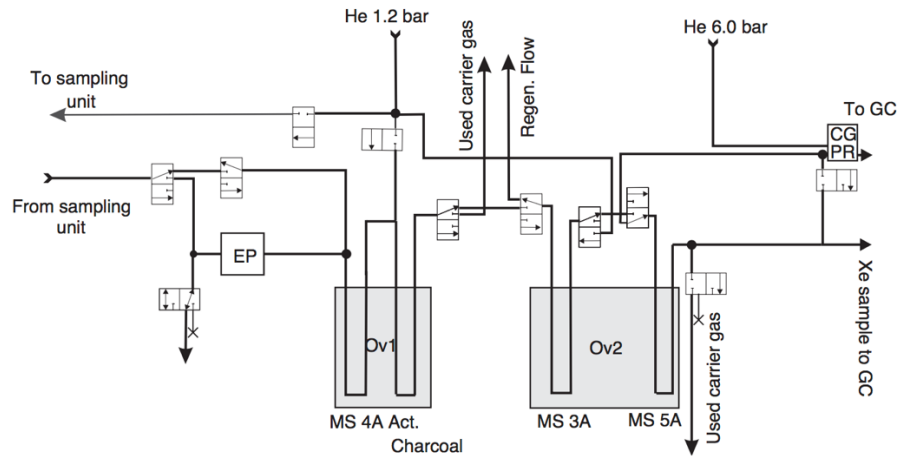


Figure 2-7: SAUNA processing system

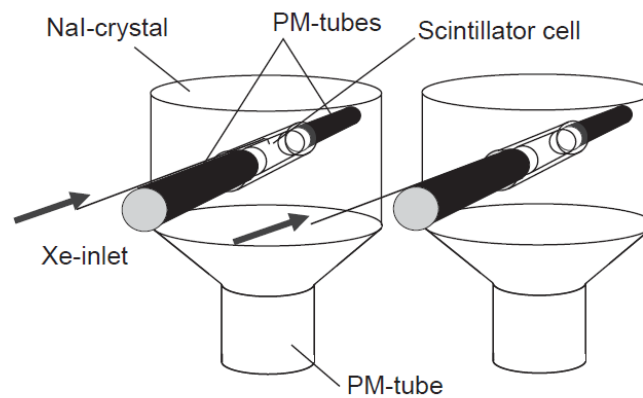


Figure 2-8: SAUNA detection system

The detection system is made of two plastic scintillators (BC404) surrounded by two NaI (TI) crystals. As mentioned before, plastic scintillators act as both gas cells and beta/conversion electron detectors. The detection volume is 6.4 cm³. The plastic scintillator is thick enough to stop the 346 keV beta particle emitted by ¹³³Xe. The gas cells/plastic scintillators are viewed by two PMT's. On the other hand, photons (gammas

and X-rays) are detected by a cylindrical NaI(Tl) inorganic scintillator. The SAUNA system has two identical detectors that are placed inside a lead-copper radiation shielding to remove ambient background and light. The copper layer is there to eliminate the 70 keV lead X-ray.

The SAUNA system uses standard analog readout electronics: NIM Bins and CAMAC. To determine coincidence, as soon as one of the plastic scintillator PMTs is triggered, a timing window is initialized. The system delays this trigger to wait for the other plastic PMT. Once that occurs, the system waits for the NaI(Tl) PMT to trigger and form a triple coincidence between all PMT's. The data readout is controlled via windows NT-based software, KmaxNT [5]. The signal generated by the beta PMT's is summed up and combined with the NaI (Tl) signal to generate a two-dimensional beta-gamma energy spectrum that can identify which radioxenon is in that sample. Figure 2-9 shows an example of a spectrum for an air sample that contained ^{133}Xe and ^{135}Xe [52]. Figure 2-9 (a) shows the 2D beta-gamma coincidence spectrum. We can observe three distributions: the top is for 250 keV gamma and 910 keV beta emitted by ^{135}Xe , the one in the middle is from 81 keV gamma and 346 keV beta emitted by ^{133}Xe , and the bottom one is from 30 keV and 346 keV beta emitted by ^{133}Xe . The dark shaded area belongs to the 910 keV beta particle in Figure 2-9 (b), where the light spectrum is for the 346 keV beta. The gamma spectrum, Figure 2-9 (c) shows the 30 keV X-ray, 81 keV gamma from ^{133}Xe , and the 250 keV from ^{135}Xe . The SAUNA MDC results meet CTBT requirements and are shown in Table 2-4. It should be noted that memory effect is a problem in this system, where station operators must deal with high background after

evacuating the system from previous samples. In addition to memory effect, the system has three PMT's, which makes maintaining, calibrating and matching the gains of these PMT's more laborious for IMS station operators.

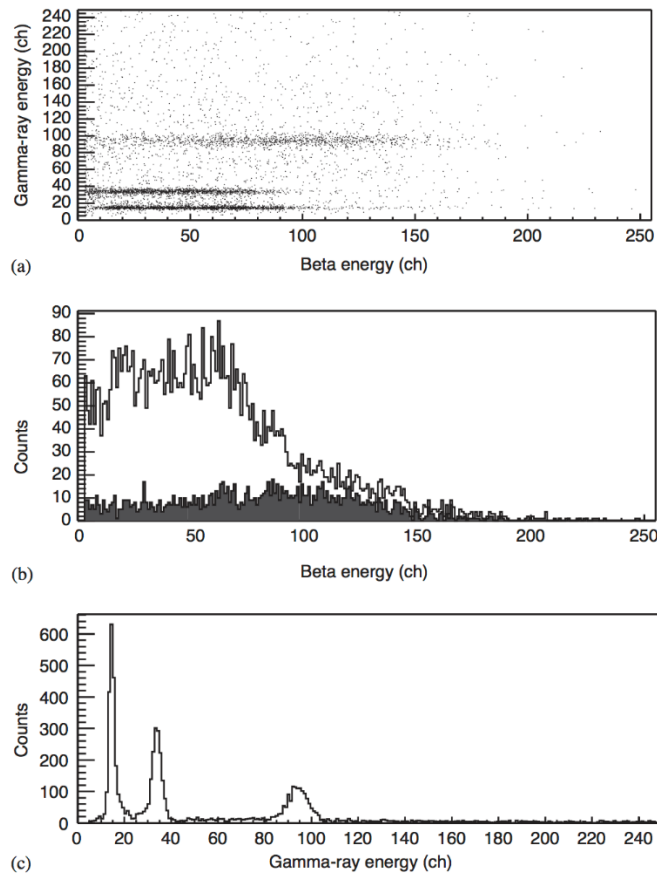


Figure 2-9: (a) SAUNA beta-gamma coincidence spectrum, (b) projected beta spectrum, and (c) projected gamma spectrum. These spectra came from a sample of ^{133}Xe and ^{135}Xe

Table 2-4: MDC results obtained by the SAUNA system

Isotope	Observed	Average conc. (mBq/m ³)	Average MDC (mBq/m ³) (12 h samples)
¹³³ Xe	Yes	1.5	0.93
^{131m} Xe	Yes	1.1	0.71
^{133m} Xe	No	—	0.57
¹³⁵ Xe	No	—	0.90

2.1.2.2 Automatic Radioanalyzer for Isotopic Xenon (ARIX)

The ARIX system was developed in Russia by the Khlopin Radium Institute. The detection system automatically extracts radioxenon from air samples and examines what type of radioxenon is in the sample and how much activity is there similar to the SAUNA system [6], [54]. Figure 2-10 shows the complete ARIX detection system.



Figure 2-10: ARIX automated detection system unit

The ARIX detection system uses beta-gamma coincidence technique to identify the radioxenon of interest. The detector has a well-type NaI(Tl) scintillation crystal for gamma and X-ray detection, and a thin plastic organic scintillator (polystyrene) coating the inside of the measuring chamber for beta and conversion electron detection as shown in Figure 2-11. The gas cell has a volume of 7.3 cm^3 [57]. The system uses two PMTs,

one viewing the NaI(Tl) crystal and the other one views the plastic scintillator [57].

Figure 2-12 shows the gated gamma spectrum generated by a sample of ^{133}Xe and ^{135}Xe .

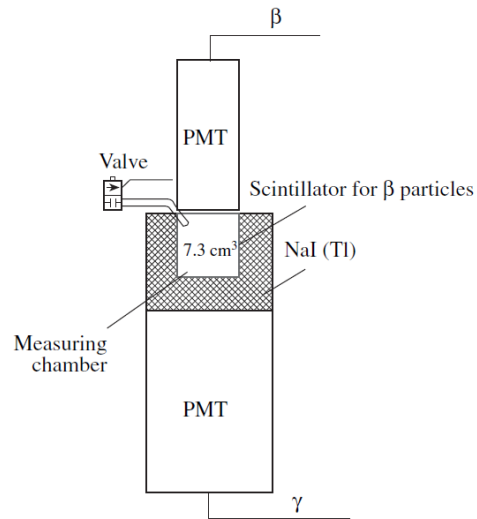


Figure 2-11: ARIX radioxenon detector

The peaks on the spectrum shown in Figure 2-12 correspond to 30 keV, 81 keV from ^{133}Xe and 250 keV from ^{135}Xe . The MDC of the ARIX detection system was measured to be 0.2-0.3 mBq/m³ for ^{133}Xe [39]. The literature around the ARIX system doesn't talk about memory effect. It is assumed that the system has the same memory effect problem the SAUNA system had because it is using a plastic scintillator and radioxenon will leak into the plastic as well.

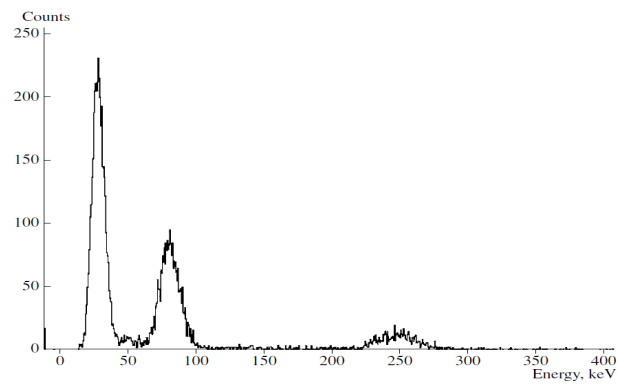


Figure 2-12: Gated gamma ray spectrum of sample containing ^{133}Xe and ^{135}Xe

2.1.2.3 Automated Radioxenon Sampler and Analyzer (ARSA)

Pacific Northwest National Lab (PNNL) have designed two radioxenon detection systems. The first detector had multiple PMTs, which made it difficult to maintain and calibrate at IMS stations. The second detector was a phoswich detector that had one PMT viewing more than one scintillator.

First ARSA Design

The first ARSA uses beta-gamma coincidence technique. It was made of 4 organic scintillators that act as gas cells (Bicron BC-404) to detect beta and conversion electrons, and two NaI(Tl) for gamma and X-ray detection. The reason behind using 4 gas cells is to allow the system to collect samples frequently and mitigate the memory effect problem. Using all four cells, it is capable of collecting samples every 8 hours, which reduces the amount of radioxenon seeping into the plastic scintillators, but at the same time allows to use a new gas cell that is almost free of xenon from previous measurements [58]. The ARSA system is shielded from background radiation using lead shielding lined with copper to remove the 70 keV lead X-ray similar to the SAUNA system. The shield provides a low background environment to allow for better detection of coincidence events. Figure 2-13 and Figure 2-14 shows a picture of the actual detection system and a schematic of the system respectively. The ARSA system uses standard NIM bin modules. Even though the design mitigates the memory effect problem and is capable of sampling every 8 hours, it is extremely difficult to maintain this system since it has 12 PMT's that should be gain matched each time the system needs calibration.

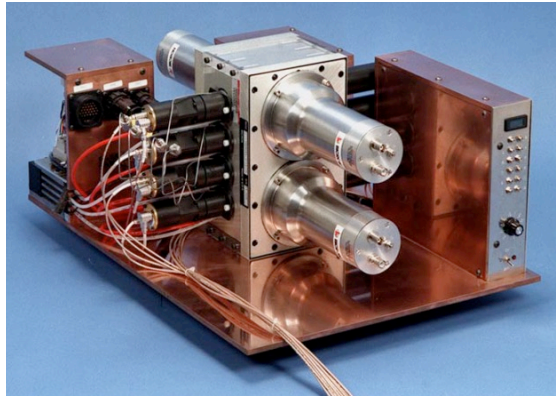


Figure 2-13: First ARSA radioxenon detection system by PNNL

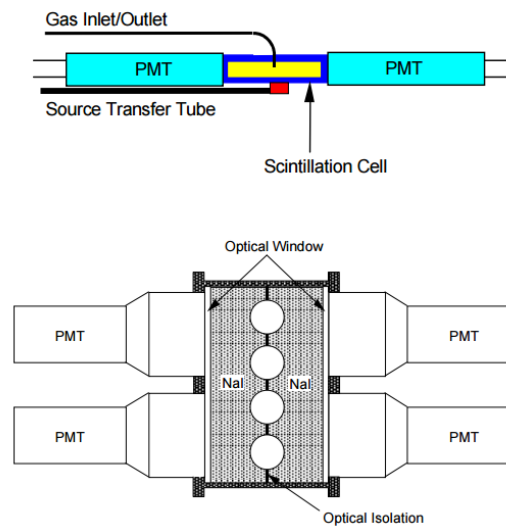


Figure 2-14: Schematic of the ARSA detection system

Figure 2-15 shows the 2D spectrum generated by the ARSA system. The detector was injected with all four radioxenons. The highlighted areas surrounded by blue rectangles are for regions of interest (ROI) that should be looked at when analyzing the spectrum.

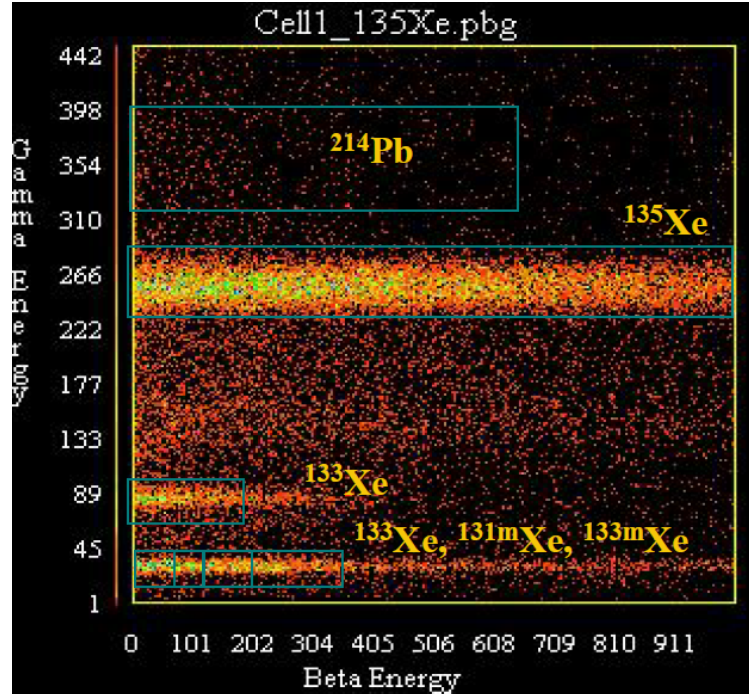


Figure 2-15: Generated 2-D spectrum from the ARSA system

The use of multiple PMTs consume additional power, which is a drawback for the SAUNA, ARIX, and ARSA systems. Some of IMS stations are in remote areas where it is difficult to provide extra power to these systems. It is also difficult to use multiple PMTs because they are fragile and need delicacy when dealing with them. To overcome the problem of multiple PMTs, Phoswich detectors were built at PNNL where one PMT views multiple scintillators. The advantage of this detector is that both photons and electrons generate a signal by the same PMT which solves the problem of gain matching. Events are identified using pulse shape discrimination techniques to discriminate between beta and gamma incidents. Phoswich detectors reduce the system power consumption and complexity of the whole design.

Second ARSA Design

The ARSA phoswich detection system was made of a NaI(Tl) cylindrical crystal for gamma and X-ray detection and a calcium fluoride (CaF₂(Eu)) thick enough for full energy deposition of beta and conversion electrons [59]. As mentioned before, pulse shape discrimination is needed to identify photons and electrons depositing energy in a phoswich detector. The PMT has an integrating preamplifier to generate fast or slow rising pulses depending on which scintillator the event had occurred. Gammas and X-rays have a rise time of 250 ns because they mostly deposit their energy in the NaI(Tl) crystals where beta particles and conversion electrons have a rise time of 940 ns since they interact in the CaF (Eu) [59]. Rise time is the amount of time it takes the pulse to go from 10% to 90% of the maximum pulse height.

Figure 2-16 shows the 2-D spectrum from radioxenon with two prominent regions: fast rising pulses are at the bottom and slow rising pulses are at the top. Pulses between those regions are due to beta-gamma coincidence interactions. Looking at the 2-D spectrum, it is extremely difficult, almost impossible, to quantify the amount of energy deposited by photons and electrons from coincidence events using this detector [59].

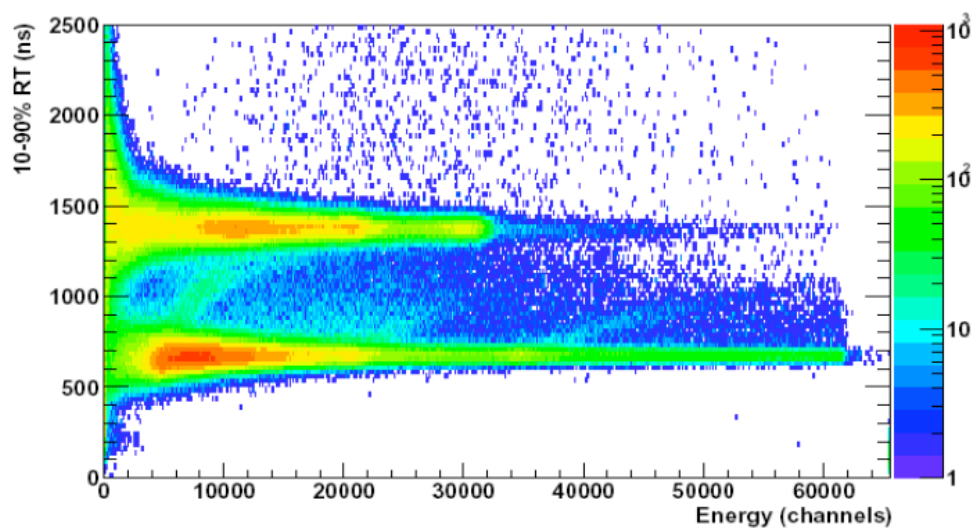


Figure 2-16: Pulse rise time 2-D spectrum for the ARSA phoswich detector

2.1.2.4 Système de Prélèvement Automatique en Ligne avec l'Analyse du Xénon Atmosphérique (SPALAX)

The SPALAX detection system was the only detection system that uses high resolution gamma spectroscopy at IMS radionuclide stations. It was developed by the French Atomic Energy Commission (CEA). In 2013, CEA decided to develop a detection system based on beta-gamma coincidence technique. Both detection systems will be discussed next.

SPALAX High Resolution Gamma Spectroscopy System (Gen. 1)

The SPALAX detection system offers a complete solution for detecting radioxenon similar to the SAUNA, ARIX, and ARSA systems. The system collects air samples, purifies the samples, concentrates the xenon and measures the activity in the sample. The detector used in the system is a High Purity Germanium detector (HPGe), specifically the Broad Energy Germanium (BEGe) spectrometer made by Canberra. Its capable of producing sharp energy peaks for gamma and X-ray energies generated by radioxenon. The spectrum generated by the HPGe detector will identify which radioxenon is present in the sample [7]. The complete SPALAX system is shown in Figure 2-17. A schematic diagram of the SPALAX system is shown in Figure 2-18. The schematic is comprised of the sampling unit, purification part, concentration part, and the radioxenon detector.



Figure 2-17: SPALAX detection system

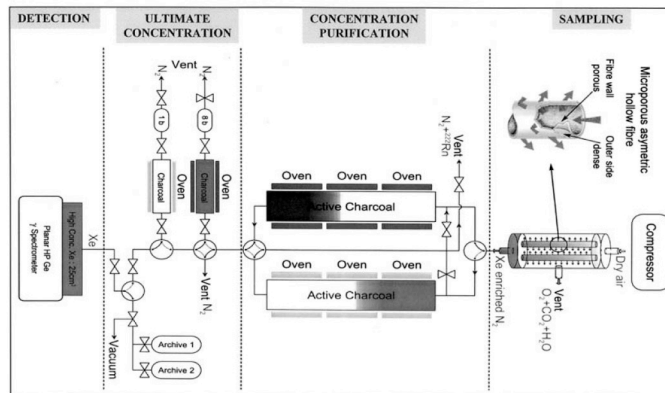


Figure 2-18: Schematic of the full SPALAX detection system

Figure 2-19 shows an example of the spectrum generated by the SPALAX system. The system was injected with an air sample that has ^{133}Xe .

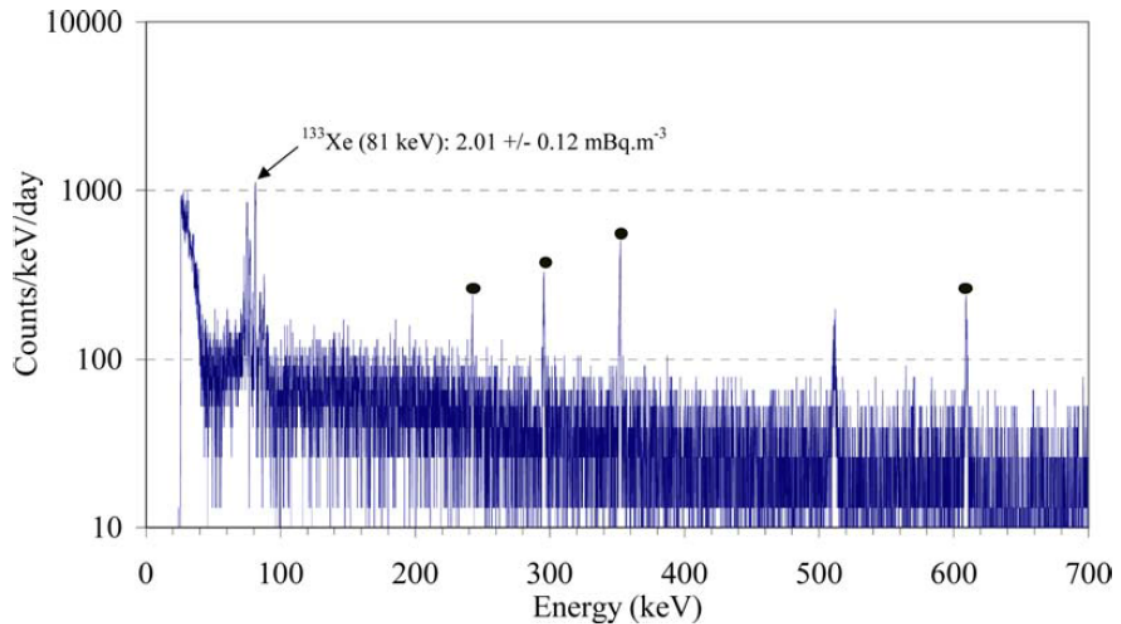


Figure 2-19. Gamma spectrum from the SPALAX system in Marseille, France

The SPALAX purification units do a great job preventing any gases other than radon and xenon to be measured. Thus, the generated spectrum is easy to interpret, which makes radioxenons identification very simple. The detector suffers when it comes to metastable radioxenons, ^{131m}Xe and ^{133m}Xe . The intensity of the gammas emitted by metastable radioxenons is so low, it is difficult to identify them. Observing the X-rays generated by the metastable isotopes is not enough to distinguish between them. Instead, the 233 keV gamma emitted by ^{133m}Xe is used to distinguish between the two metastable isotopes since it has a higher intensity [39]. If the 233 keV gamma is present in the spectrum, then ^{133m}Xe is present in the sample. Given that both gammas emitted by the metastable isotopes have intensities of 10.00% in the case of ^{133m}Xe and 1.95% for ^{131m}Xe , the SPALAX system is not as sensitive as it is to ^{133}Xe and ^{135}Xe . This is one of the issues with the SPALAX system. Another disadvantage is that detecting 30 keV

X-rays is not trivial since they are at the low energy end of the gamma spectrum, which contains a lot of background events [60]. A special software, Aatami, is used to establish a background baseline under the spectrum so it could be subtracted, which will make the X-ray peaks more pronounced. To overcome this problem, CEA decided to build a beta-gamma coincidence system based on a gas cell made of silicon detectors manufactured by Passivated Implanted Planar Silicon (PIPS) technology, developed by Canberra.

SPALAX Beta-gamma Detection System, First Attempt (Gen. 2)

The new SPALAX beta-gamma detection system was developed by CEA in cooperation with Canberra. The gas cell is made of two silicon detectors called PIPSBox based on PIPS technology that has several advantages over other silicon growing methods. These advantages will be detailed later in the materials and methods chapter. The active volume of the gas cell is 11.7 cm^3 . The PIPSBox detector was coupled to a NaI(Tl) scintillator to test the beta-gamma coincidence capability of the system. The main goal of the design was to improve the detection sensitivity, especially for metastable isotopes [8]. Figure 2-20 shows the detection system on the left, where the PIPSBox is placed inside the NaI(Tl) crystal. The right side of the figure shows components that make the PIPSBox and where the gas cell is. The detector used NaI(Tl) because it has excellent detection efficiency for both gamma rays and X-rays.

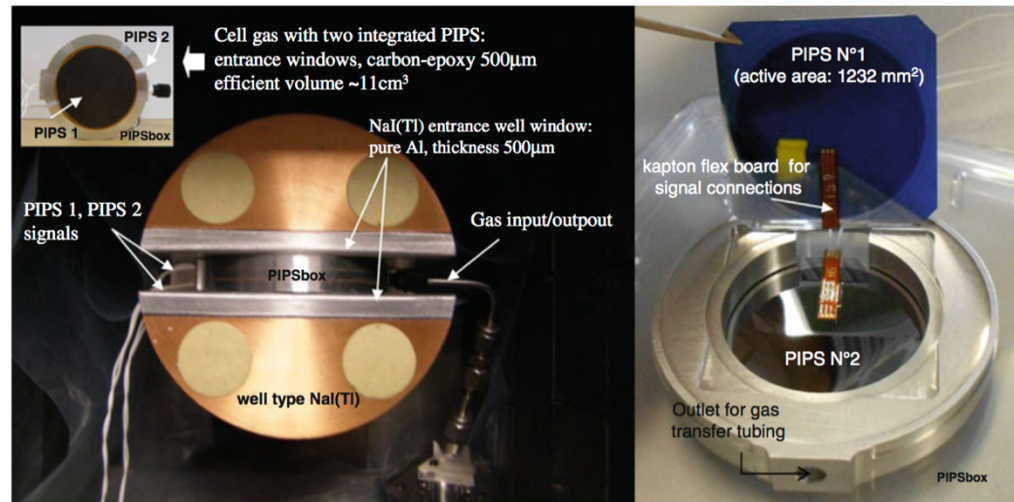


Figure 2-20: SPALAX first beta-gamma coincidence detection system

Figure 2-21 shows a 2-D spectrum generated by the SPALAX beta-gamma coincidence system. The gas cell was injected with an air sample containing ^{131m}Xe and ^{133}Xe . The spectrum shows a distribution along the 81 keV line that extends up to the 346 keV energy on the PIPSBox energy. Clusters of events are concentrated at the 30 keV energy on the NaI(Tl) and is concentrated at the 129 keV along the PIPSBox energy line, which corresponds to coincidence events from ^{131m}Xe . It should be noted that the air sample was injected at an IMS station in Ottawa, Canada.

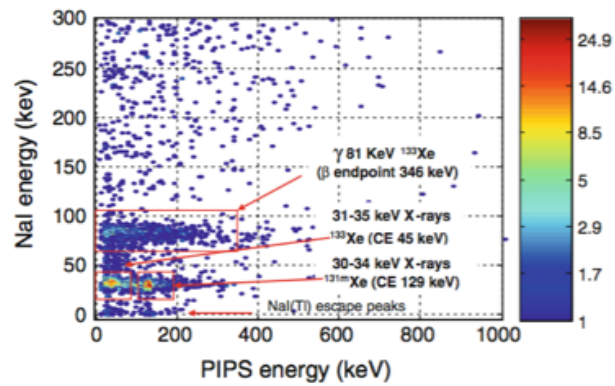


Figure 2-21: SPALAX 2-D spectrum collected at an IMS station in Ottawa, Canada

Figure 2-22 (top) shows the gated gamma spectrum of the sample generated by the NaI(Tl) crystal. The gamma spectrum shows the 30 keV peak from $^{131\text{m}}\text{Xe}$ and the 81 keV peak from ^{133}Xe . The bottom section of the figure shows the PIPSBox gated electron energy. The spectrum shows the 45 keV conversion electron peak from ^{133}Xe , the 129 keV peak from $^{131\text{m}}\text{Xe}$ and the 346 keV beta distribution from ^{133}Xe .

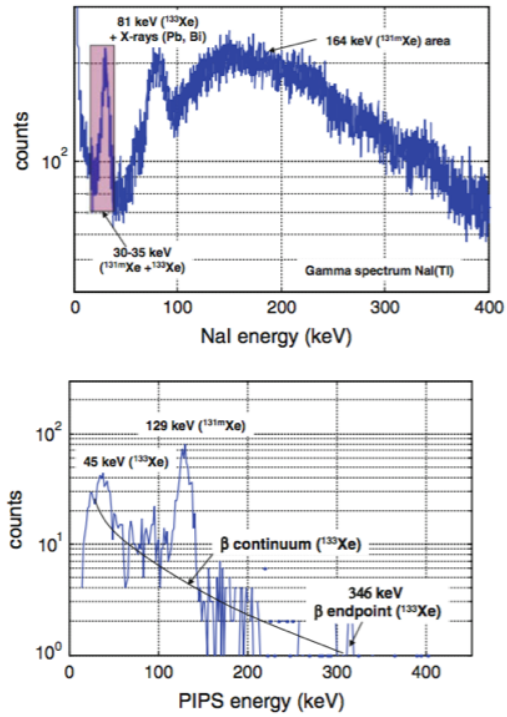


Figure 2-22: Gated gamma and beta spectra from ^{131m}Xe and ^{133}Xe

Reported MDCs for ^{131m}Xe and estimated for ^{133m}Xe have been found to be $(1.8 \pm 0.3) \cdot 10^{-4} \text{ Bq} \cdot \text{m}^{-3}$ based on 1 day measurements [8]. Precise measurements for ^{133}Xe and ^{133}Xe have not been performed with detector.

SPALAX Beta-gamma Detection System, Second Attempt (Gen. 3)

The second SPALAX Beta-Gamma detection system used the same PIPSBox gas cell but coupled it to an HPGe detector. The reason behind using the germanium detector was to precisely calculate the MDC for all four radioxenons (^{131m}Xe , ^{133m}Xe , ^{133}Xe , and ^{135}Xe). Figure 2-23 shows the PIPSBox coupled to the HPGe before they're placed inside the SPALAX system. Figure 2-24 shows both detectors next to the cooling unit for the HPGe detector.



Figure 2-23: PIPSBox on top of the HPGe detector

In this work, a 2-D spectrum was generated using the PIPSBox detector for a sample containing ^{131m}Xe and ^{133}Xe . Figure 2-25 shows the generated PIPSBox 2-D spectrum in addition to a spectrum of one of the silicon detectors.



Figure 2-24: (left) PIPSBox coupled to the HPGe detector, (middle) silicon wafer used in the PIPSBox, (right) PIPSBox detector

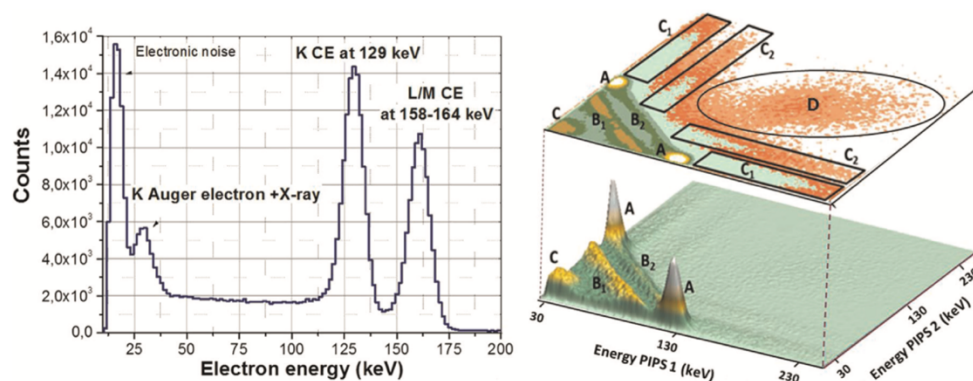


Figure 2-25: (left) Conversion electron energies measured by one of the silicon detectors, (right) Coincidence events between the two silicon detectors for a ^{131m}Xe , ^{133}Xe sample

The events labeled on the coincidence spectrum were described in that research as follows [9]:

“(A) events are ^{131m}Xe K-Conversion Electrons (K-CE) in coincidence with either xenon K-Auger electrons or K X-rays.

(B1) and (B2) events are ^{131m}Xe electrons (respectively K-CE and L-, M- or N-CE) depositing energy in both Si-PIN detectors at the same time. These events can be characterized as rebounding electrons.

(C) events are ^{133}Xe K-CE in coincidence with either cesium K-Auger electrons or K X-rays.

(C1) and (C2) events are ^{133}Xe β^- electrons in coincidence either with cesium K-Auger electrons or K X-rays (for C1), or with ^{133}Xe photons (for C2)”

MDCs were found to be 0.1 mBq/m³ for ^{131m}Xe , ^{133m}Xe , ^{133}Xe and 0.4 mBq/m³ for ^{135}Xe for a single HPGe configuration. This detection system can be used with one HPGe detector as shown in Figure 2-24 or with two HPGe detectors as shown in Figure 2-26.

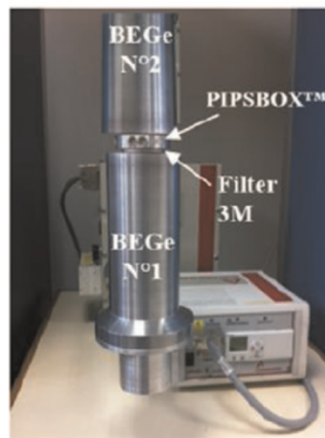


Figure 2-26: PIPSBox coupled to two HPGe detectors and a 3M filter for particle collection

Memory effect was 0.05% following a 24 h vacuum process, and 0.1% following an 80 min vacuum process. Both results comply with CTBT requirement, which is 5%.

2.1.2.5 XIA Beta-Gamma Coincidence Phoswich Detector

XIA developed a phoswich detector to detect radionuclides using Beta-Gamma coincidence technique. The detector is made of plastic scintillator (BC-404) to detect beta and conversion electrons. The plastic is coupled to a CsI(Tl) scintillator to detect gamma and X-rays. One PMT is used to generate signals from both detectors, which is directly connected to a high-speed digital pulse processor (XIA DGF Pixie-4) [61], [62]. Figure 2-27 shows the pulses generated by the plastic scintillator (fast pulses) and the pulses generated by the CsI(Tl) (slow pulses) and coincidence pulses that have both fast and slow components. The pulses were generated using a ^{60}Co source.

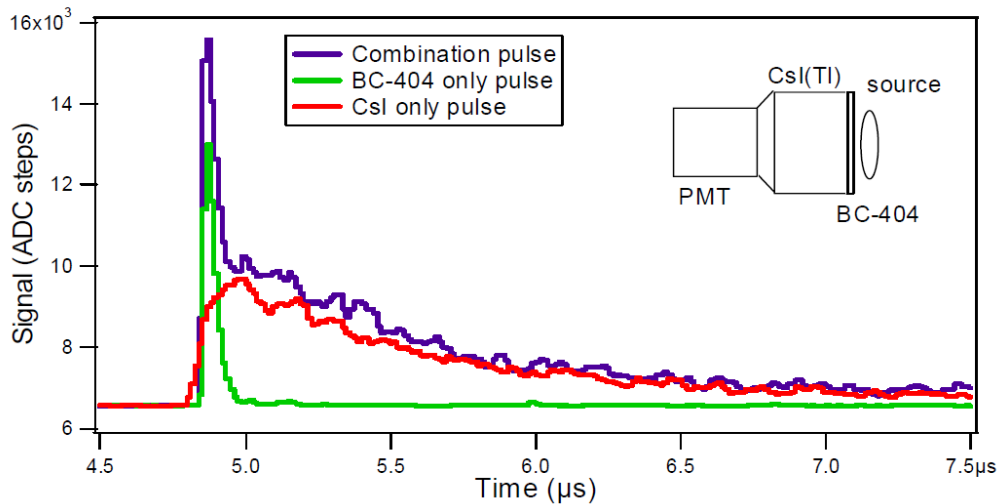


Figure 2-27: Pulse shapes generated by the phoswich detector

The key to successfully using a phoswich detector is to use scintillators with different decay to so that pulse shape discrimination is possible. Figure 2-28 shows the 2-D energy spectrum generated by ^{133}Xe . The y-axis represents CsI(Tl) energy and the x-axis represents the BC-404 energy. A digital trapezoidal filter is used to calculate the

amount of energy deposited in each scintillator. The trapezoidal filter was implemented in a field programmable gate array (FPGA) in Pixie-4.

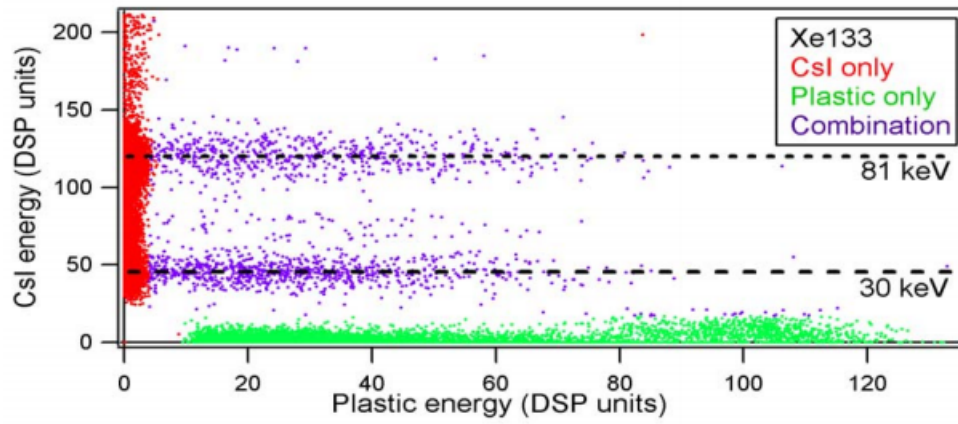


Figure 2-28. XIA phoswich detector 2-D energy spectrum for ^{133}Xe source

2.1.2.6 XIA 24-element Silicon PIN diode detector

XIA devolved another beta-gamma coincidence system using 24 silicon PIN diode detectors. The detector measures beta particles, conversion electrons, and X-rays. The gas cell is made from copper. The active detection area is 600 mm². The detector and preamplifiers are placed inside an airtight Aluminum housing that is also sealed from light. Dry nitrogen gas is used to stop vapor condensation on the PIN diode outer surfaces and to cool the diodes down to reduce thermal background [63]. Figure 2-29, Figure 2-30 and Figure 2-31 shows different angles of the detection system.

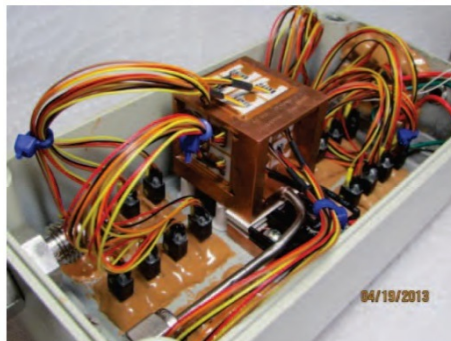


Figure 2-29: Detection system inside the aluminum box

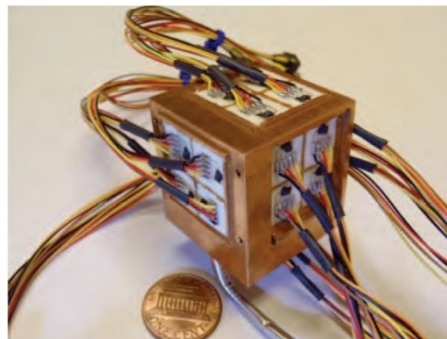


Figure 2-30: Size of the copper cube

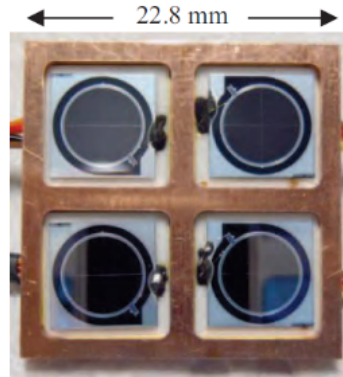


Figure 2-31: PIN diodes mounted on the ceramic holders

Figure 2-32 shows coincidence between the PIN diode detectors when that gas was injected with ^{127}Xe and ^{37}Ar , which are used for calibration purposes in remote IMS station. Each point on this spectrum represents a coincidence event between two PIN diodes. ^{127}Xe has a 30 keV X-ray and multiple conversion electrons with energies at 112 keV, 139 keV, 170 keV and 198 keV.

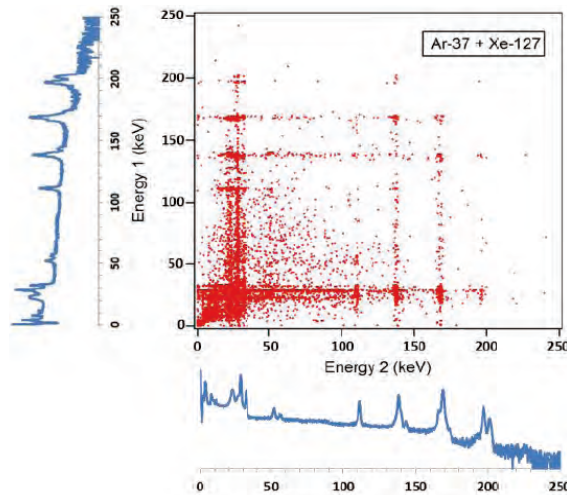


Figure 2-32: ^{127}Xe 2-D spectrum

Figure 2-33 shows a gated spectrum from a ^{133}Xe and $^{133\text{m}}\text{Xe}$. 29 keV and 30 keV X-ray peaks are visible with excellent energy resolution. Also, 45 keV conversion electrons can be seen and 81 keV peak is barely noticeable at the high-energy end of the spectrum. This detector has a disadvantage because it is not suitable to detect gammas from ^{133}Xe and ^{135}Xe .

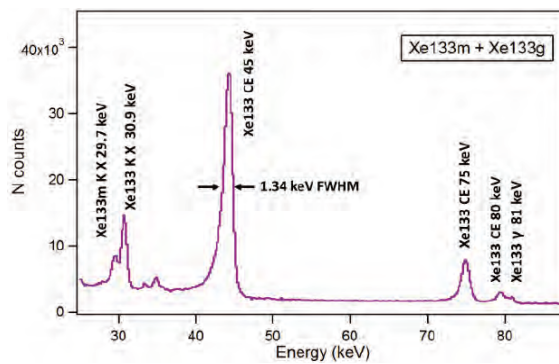


Figure 2-33: Gated spectrum from $^{133\text{m}}\text{Xe}$ and ^{133}Xe using the 24-element silicon detectors

2.1.2.7 Beta-Gamma Coincidence Detectors Developed at OSU

The School of Nuclear Science and Engineering at Oregon State University (OSU) have been designing prototypes for beta-gamma coincidence detectors since late 2006. The radiation detection group, led by Dr. Abi Farsoni, designed more than 6 detection systems. Details about earlier designs can be found at these references [24], [64], [65]. In the next section, a description of OSU's most recent designs will be discussed. Two phoswich detectors with similar scintillators, one was planar and the other a well-type phoswich detector, the second one was for a two element CdZnTe (CZT) detector, and the last one coupled a CZT detector with a plastic scintillator. The plastic scintillator was read using a silicon photomultiplier (SiPM), which marks the first time an SiPM instead of a PMT was used in radioxenon detection systems.

2.1.2.8 Actively Shielded Phoswich Detector (ASPD)

The actively shielded phoswich detector (ASPD) was made of three scintillators: plastic scintillator (BC-400) to detect beta and conversion electrons, CsI(Tl) crystal to detect gamma and X-rays, and a well-type BGO crystal that acts as a passive/active shield from ambient background and Compton events respectively. Suppressing Compton events was performed by pulse processing, where it reduced the Compton continuum of the gamma spectrum [26]. The plastic scintillator was coated with a layer of aluminum to minimize the memory effect [27]. A schematic diagram of the ASPD is shown in Figure 2-34.

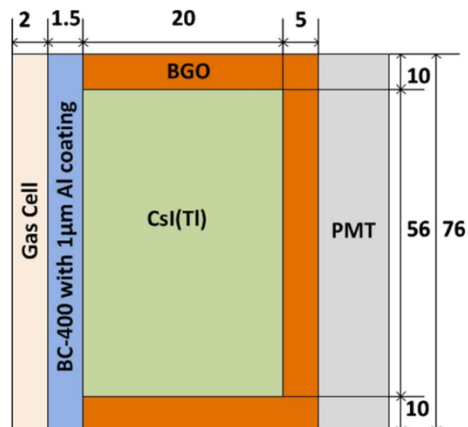


Figure 2-34: Schematic diagram of the ASPD (dimensions in mm)

A picture of the assembled detector is shown in Figure 2-35. The crystals are wrapped in Teflon tape to reflect the light inside the crystal assembly and are coupled to one PMT.

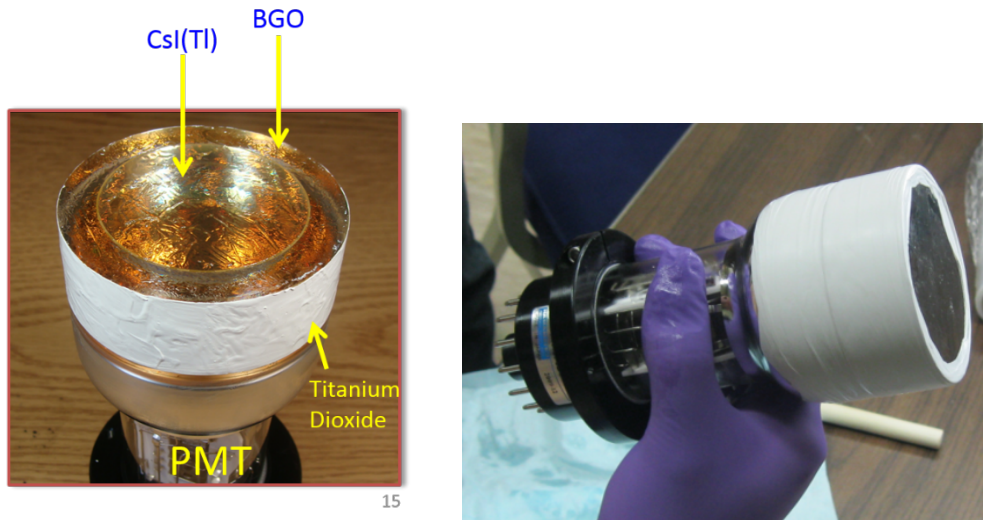


Figure 2-35: ASPD assembled. Scintillators are wrapped in Teflon tape to guide the scattered light towards the PMT

Photomultiplier tube anode pulses were analyzed using a digital pulse processor with an FPGA on board. Figure 2-36 shows a 3-D beta-gamma coincidence energy plot of ^{135}Xe

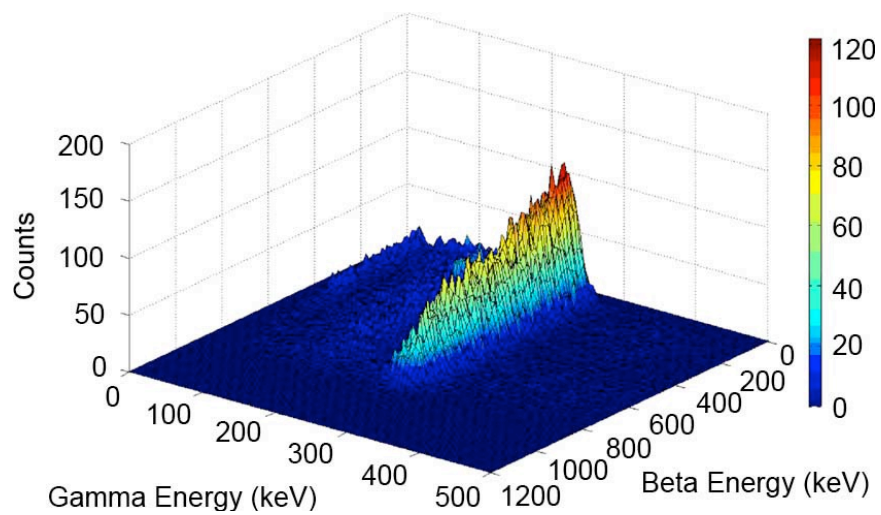


Figure 2-36. Beta-gamma coincidence energy spectrum using ^{135}Xe that was activated at OSU TRIGA reactor

The spectrum shows events along the 250 keV gamma energy and is distributed until the 910 keV maximum beta energy, which is what we expect from a ^{135}Xe sample. One issue with this detection system is that the detection solid angle is half of 4π . It means that more than half of the radiation emitted by radioxenon will not be detected.

2.1.2.9 Well-type Actively Shielded Phoswich Detector (WASPD)

This design was developed to improve on the ASPD, since the detection solid angle was not maximized. The same scintillators were used in this design but in well-type design to increase the detection solid angle. The gas cell was made of a well-type plastic scintillator. Like ASPD, it is also used to detect beta and conversion electrons. The CsI(Tl) was also a well-type and is used to detect gamma and conversion electrons. The BGO crystal was also well-type and is used as a passive/active shield for the gamma and beta detectors. A schematic diagram of the detection system is shown in Figure 2-37. Using well-type scintillators improves the detection efficiency of the detection system [22].

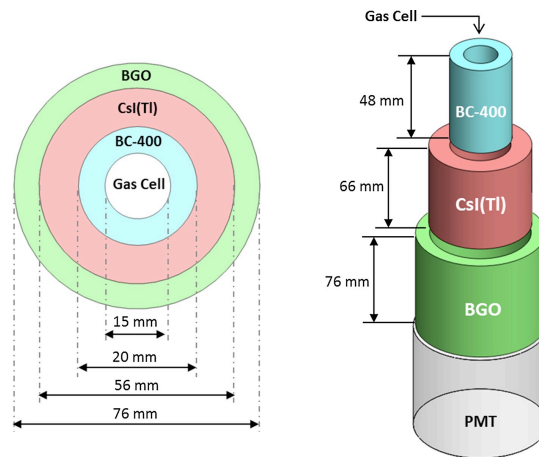


Figure 2-37: Schematic diagram of the WASPD (dimensions in mm)

A picture of the assembled WASPD detector is shown in Figure 2-38. The crystals are wrapped in Teflon tape to reflect the light inside the crystal assembly and are coupled to one PMT surrounded by a plastic detector housing.

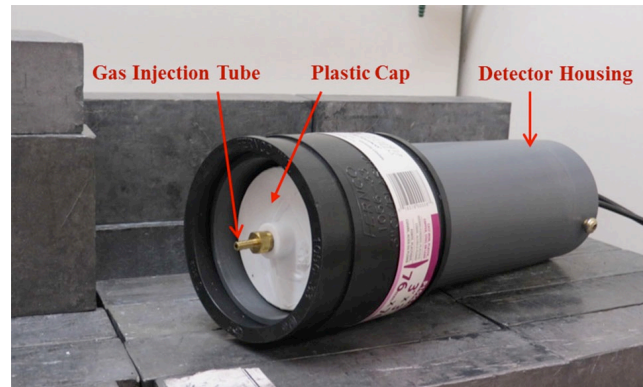


Figure 2-38: Assembled WASPD inside the plastic housing

Like the APSD, PMT anode pulses were analyzed using a similar digital pulse processor with an FPGA on board (RX1200) designed by Instruments LLC. Figure 2-39 shows a 3-D beta-gamma coincidence energy plot of $^{133\text{m}}\text{Xe}$ and ^{133}Xe [22].

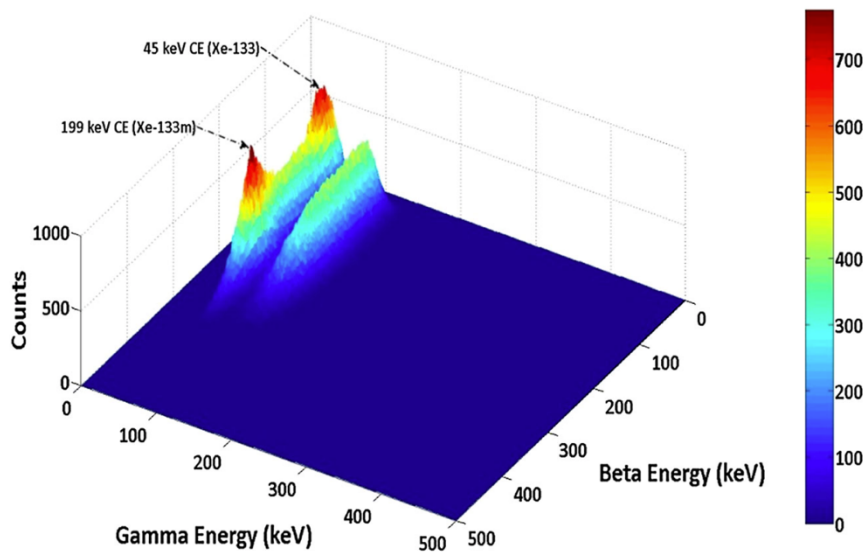


Figure 2-39: Beta-gamma coincidence energy spectrum using $^{133\text{m}}\text{Xe}$ and ^{133}Xe that was activated at OSU TRIGA reactor

Pulse shape discrimination and other pulse processing functions were implemented in the FPGA for real time analysis. The WASPD MDC met CTBT requirements ($< 1 \text{ mBq/m}^3$) as shown in Figure 2-40. The plastic scintillator for this detector was not coated with an aluminum layer, so memory effect was a problem for this detector.

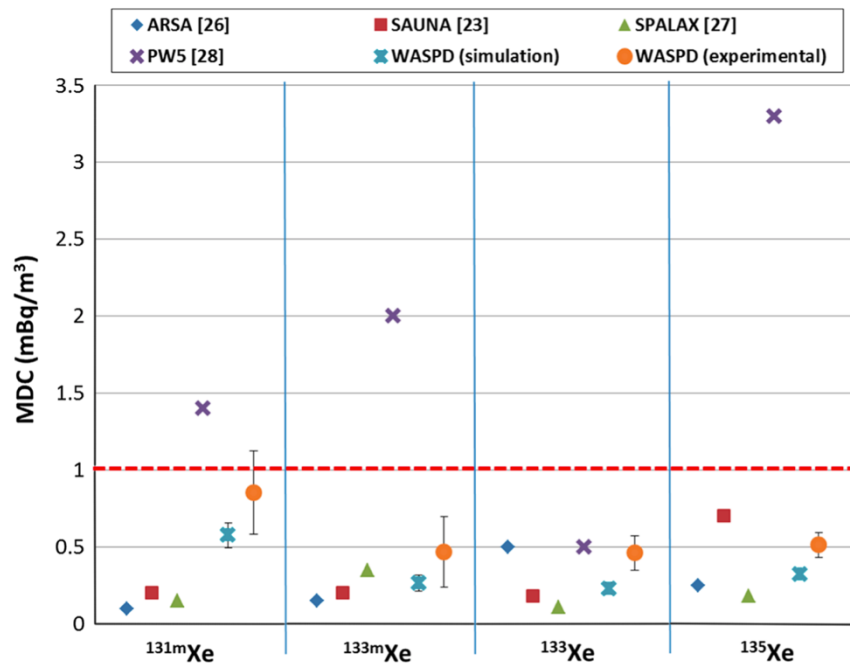


Figure 2-40. MDC of WASPD detection system compared to other beta-gamma detection system prototypes

2.1.2.10 The Two-Element CZT-Based (TECZT) Radioxenon Detection System

The TECZT prototype was proposed to overcome several problems: memory effect, improve MDC by using semiconductor detectors that have better energy resolution when compared to scintillators, low power consumption, and compactness with less complexity for remote IMS stations. The prototype had two CZT crystals with an ultimate goal of using six CZT crystals for the best detection solid angle. The TECZT uses beta-gamma coincidence technique to identify radioxenon [66]. Figure 2-41 shows a schematic of the TECZT detection system.

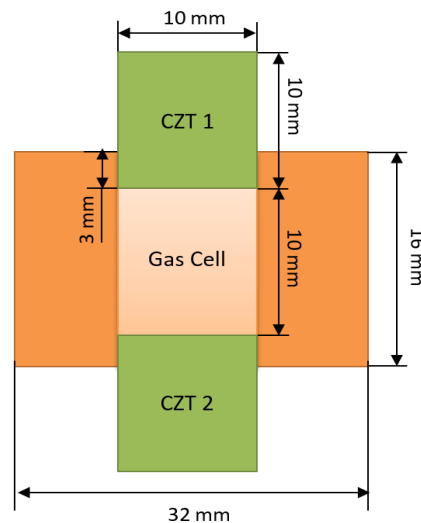


Figure 2-41: Schematic diagram of the TECZT system

The CZT crystals used in this system have coplanar anodes (shown in Figure 2-42) to simplify the radioxenon detection process.

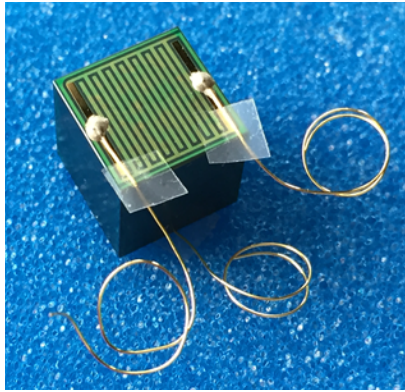


Figure 2-42: Coplanar anode on the 1 cm x 1 cm x 1 cm CZT crystal from Redlen technologies

The detection system (Figure 2-43) was simulated and the simulation results were very promising. However, experimental results showed a drawback for this system where electrons and beta particles were depositing partial energy in one CZT and scattering back to the other CZT, which left a tail in the region of interest for each radioxenon, especially the metastable isotopes. Figure 2-44 shows the 2-D spectrum obtained by ^{131m}Xe . It shows the regions where partial energy deposition from conversion electrons interaction with both CZTs created a tail along the 30 keV line in coincidence with the 129 keV.

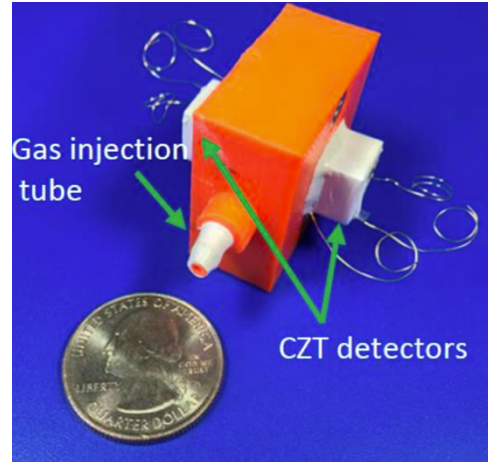


Figure 2-43: Complete TECZT system

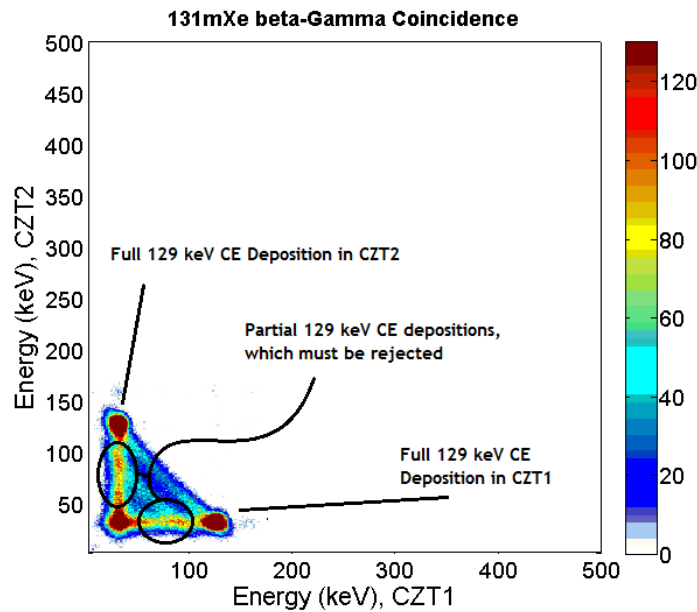


Figure 2-44: 2-D beta-gamma coincidence energy spectrum from ^{131m}Xe

Minimum detectable concentration (MDC) of this system for ^{133}Xe met the requirements of CTBT. However, the remaining three radioxenons had MDCs higher than the 1 mBq/m^3 threshold set by CTBT. Increasing the number of CZT crystals to 6 will decrease the MDC for all radioxenons and will bring it down to less than 1 mBq/m^3 as shown in Figure 2-45 [66].

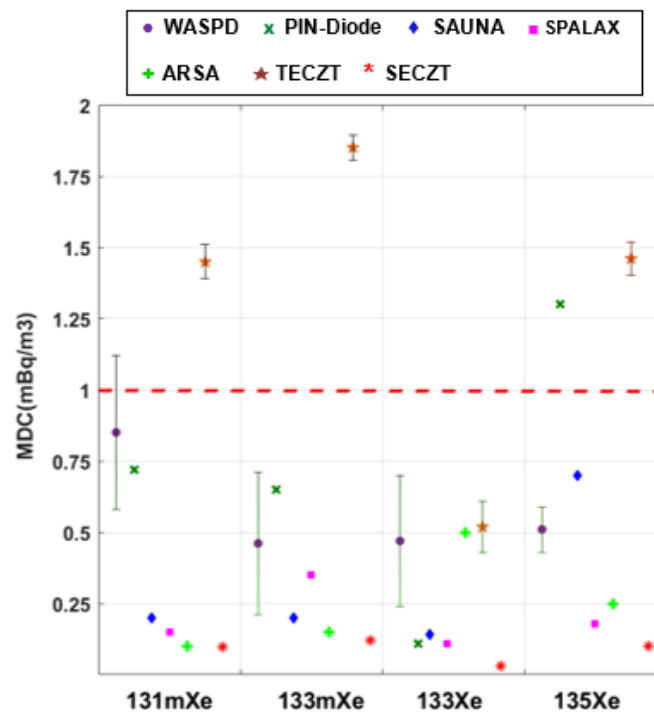


Figure 2-45: MDC of TECZT and Six Element CZT (SECZT) detection systems compared to other beta-gamma detection system prototypes

2.1.2.11 The CdZnTe, Array of SiPMs, and Plastic Scintillator (CASP) Radioxenon Detection System

This detection system was developed right after the TECZT system. The goal was to take advantage of the excellent CZT resolution from CZT's but get rid of the electron backscattering problem. A coplanar CZT detector was coupled to a plastic scintillator (EJ-212) matched to an SiPM. The prototyped had only one CZT detector, but the final system would've had 2 or 4 CZT detectors to increase the detection solid angle. Figure 2-46 shows a schematic of the detection system with 2 CZT detectors, and the coincidence events of interest from radioxenons [67].

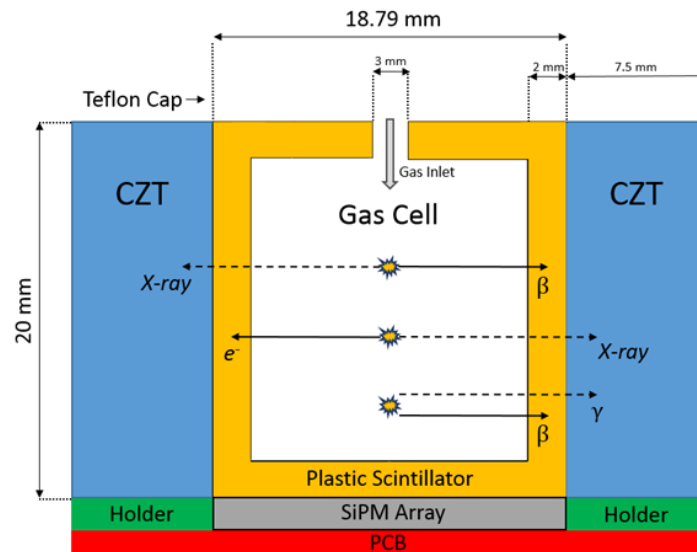


Figure 2-46: Schematic of the CASP detection system with 2 CZT detectors and the coincidence events of interest

A 3-D cross section made in Solidworks for the prototype is shown in Figure 2-47.

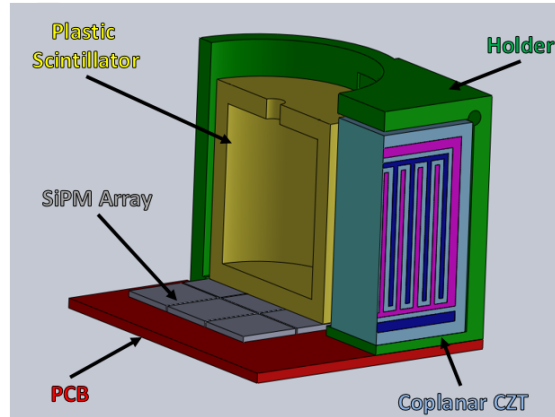


Figure 2-47: 3-D cross section of the CASP prototype

The CASP system with preamplifiers and other electronics is shown in Figure 2-48 inside an aluminum box to shield it from light and electromagnetic radiation. The plastic scintillator was wrapped in Teflon and black tape to stop light from leaving the plastic and light from going inside the gas cell respectively.



Figure 2-48: CASP detector inside an aluminum box with preamplifiers and other electronics

Figure 2-49 shows the CASP 2-D spectrum generated from injecting the gas cell with ^{135}Xe . The figure shows events along the 250 keV gamma line with a distribution up to the 910 keV maximum beta energy. At the bottom of the figure, there is a cluster of events resulting from high energy beta particles triggering the SiPM, which creates false positive coincidences. These events can be removed by pulse processing but it keeps the system busy with false pulses.

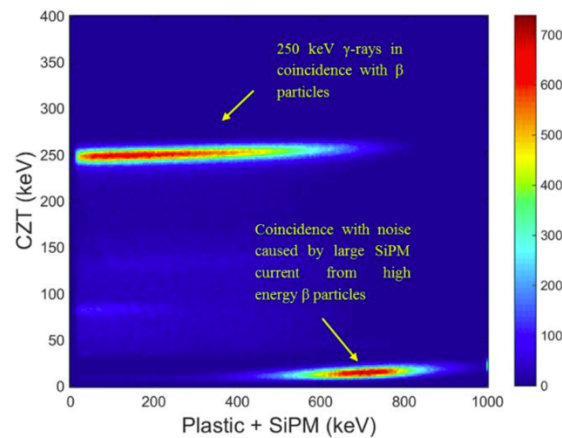


Figure 2-49: CASP 2-D spectrum from ^{135}Xe

Figure 2-50 shows the CZT and plastic scintillator gated spectra. The gamma spectrum shows the 250 keV peak with a peak at the low end of the energy spectrum from electronic noise. The beta spectrum shows a beta distribution with a maximum energy of 910 keV, which is what we expect from this radioxenon.

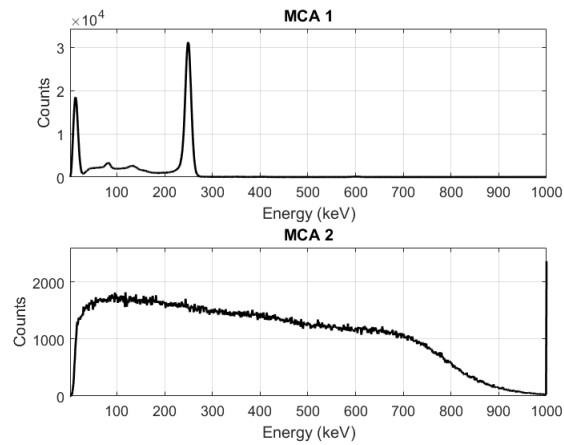


Figure 2-50: Gated gamma and beta spectra from ^{135}Xe

The MDC from the CASP system, both prototype and with 4 CZT detectors is shown in Figure 2-51. The figure compares the CASP system with previous OSU detectors and other radioxenon detectors available today. ¹

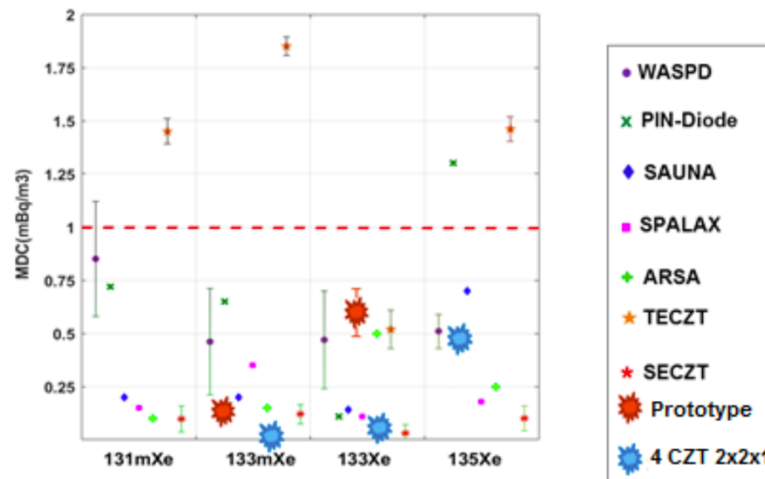


Figure 2-51: MDC calculation for the CASP prototype and estimation for the 4 CZT CASP

One of the important conclusions to the TECZT and CASP systems is that CZT detectors have excellent resolution compared to other photon detectors in radioxenon detection systems. Table 2-5 shows a comparison between the resolution of CASP, TECZT and other OSU and available radioxenon detection systems.

Table 2-5: Energy resolution for gamma and X-rays from all four radioxenons for CASP and other detection systems

	Gamma Energy (keV)	CASP (this work)	TECZT [11]	WASPD [55]	Phoswich [55]	SAUNA [6] [8]	ARSA [8] [56]	BGW [37] [57]
Energy Resolution (FWHM, %)	30 (¹³³ Xe)	33.4	48.2	47.7	46	23-30	32	18
	81 (¹³³ Xe)	12.4	12.5	27.6	24	13	25	13
	250 (¹³⁵ Xe)	5.7	4.4	19.3	13	N/A	9.6	N/A

2.1.2.12 Summary of available detection systems Detector

A summary of the reviewed detection systems and MDC results are shown in Table 2-6.

Table 2-6: Summary of discussed detection systems with MDC results

Detection System	Technique	Detectors Used	Memory Effect	MDC ^{133}Xe (mBq/m³)
SAUNA	Beta-Gamma Coincidence	Scintillators	yes	0.18
ARIX	Beta-Gamma Coincidence	Scintillators	yes	0.2-0.3
ARSA Gen.1	Beta-Gamma Coincidence	Scintillators	yes	0.5
ARSA Gen.2	Beta-Gamma Coincidence	Scintillators	yes	N/A
SPALAX Gen.1	High-resolution Gamma Spectroscopy	Semiconductor	no	0.15
SPALAX Gen.2	Beta-Gamma Coincidence	Scintillators/Semiconductors	no	N/A
SPALAX Gen.3	Beta-Gamma Coincidence	Semiconductors	no	0.4
XIA Phoswich	Beta-Gamma Coincidence	Scintillators	yes	0.5

XIA Diodes	Beta-Gamma Coincidence	Semiconductors	no	0.11
OSU ASPD	Beta-Gamma Coincidence	Scintillators	no	0.18
OSU WASPD	Beta-Gamma Coincidence	Scintillators	yes	0.46
OSU TECZT	Beta-Gamma Coincidence	Semiconductors	no	0.57-1.26
OSU CASP Prototype	Beta-Gamma Coincidence	Scintillators/ Semiconductors	yes	0.64

3. Materials and Methods

3.1 Introduction

The goal of this work is to build a radioxenon detection system prototype capable of mitigating problems that exist in current detection systems installed in IMS stations, yet produce an MDC result that meets CTBT requirements. Using the research knowledge obtained at OSU labs, it is obvious that semiconductor detectors make better candidates for radioxenon detection systems due to their excellent energy resolution, and their resistance to memory effect, which will decrease the MDC for all four radioxenons. The IMS is also looking to increase the frequency of air sampling from 24 hours down to 8 hours because simulations revealed that reducing the sampling times to 8 hours increases the sensitivity to changes of radioxenons in the atmosphere [8]. Using a gas cell made of a semiconductor detector will help meet this goal since memory effect is not an issue with semiconductors [9]. The main project objective of the new design can be summarized as follows:

1. Improve detection sensitivity of current radioxenon detection systems
2. Build a detection system appropriate for use in remote areas
3. Couple CZT detectors with silicon gas cell, a novel approach that has never been done before
4. Increase the frequency of air sampling at IMS stations

Therefore, this work centers around building a detection system made of the recently developed PIPSBox gas cell coupled to two coplanar CZT detectors. This detection system will have mitigated the memory effect problem as we saw in the

SPALAX Gen.3 detection system, and will be less complex, compact and much easier to deploy and maintain in remote IMS stations. It is expected to generate comparable results to the PIPSBox/HPGe detector without the need for liquid nitrogen in remote stations or the extra power needed in the case of using electrical cooling.

The two coplanar CZT detector will detect gamma and X-rays, where the silicon detectors in the PIPSBox will detect beta and conversion electrons. The PIPSBox detector gas cell detector is made of two silicon wafers made by a new technology called Passivated Implanted Planar Silicon. The novel Passivated Implanted Planar Silicon (PIPS) detectors are a new family of detectors made specially to detect charged particles. Advantages of PIPS technology over other silicon growing methods are [68]:

1. *“All junction edges are buried – no epoxy edge sealant is needed or used.*
2. *Contacts are ion-implanted to form precise, thin, abrupt junctions for good alpha resolution.*
3. *Entrance window is stable and rugged – it can be cleaned readily and reliably.*
4. *Leakage current is typically 1/8 to 1/100 of that of SSB and DJ detectors.*
5. *Dead layer (window) thickness is less than that of comparable SDB or DJ detectors.*
6. *Standard detectors are bakeable to 100 °C – higher for special models.”*

Two digital signal processors will be used to evaluate the signals coming of the PIPSBox/CZT detection system, DPP 8.0 and DPP 2.0. The first processor DPP8 is the latest processor being developed here at OSU. The processor is an eight-channel digital signal processor, hence the name DPP8. It has a Kintex 7 FPGA, a 125 MHz sampling frequency, a 14-bit resolution analog-to-digital converter (ADC), an on-board digital-

to-analog converter (DAC) for offset modification, and USB 3.0 technology for data transfer and communication between the FPGA and the PC side. The other processor DPP2 is a two-channel digital signal processor with a Spartan 3 FPAG, 200 MHz sampling frequency, a 12-bit resolution ADC, an on-board DAC, and USB 2.0 technology for communication between the FPGA and the PC side. In this work, an FPGA firmware will be developed to evaluate the performance of DPP8 in addition to multiple MATLAB scripts for data acquisition and processing. The PIPSBox/CZT detection system will be characterized using DPP8. Once the characterization process is completed, DPP8 will be used in radioxenon measurements to evaluate the performance of the processor to all four radioxenons of interest. Subsequently, DPP2 will be used to evaluate the response of the detection system to all four radioxenons since this processor is fully developed and have been used in the two-element CZT detection system and the CASP system, both developed here at OSU [31], [66], [67]. Finally, energy resolution, background measurement, and MDC will be calculated for all four radioxenons using results obtained from DPP2 and DPP8.

3.2 The PIPSBox/CZT Detection System

The PIPSBox/CZT detection system is made of the recently developed PIPSBox gas cell detector from Canberra and two $1 \times 1 \times 1 \text{ cm}^3$ coplanar CZT crystals from eV products. The silicon detectors inside the PIPSBox are two square wafers with a 1200 mm^2 active area each as it was shown in Figure 2-24. The wafers are $500 \mu\text{m}$ thick and are placed inside an aluminum holder with a 70 mm circular window in diameter. More information and pictures for the PIPSBox are provided in the appendix section.

Figure 3-1 shows the PIPSBox inside a custom made plastic holder with two CZTs coupled to the sides of the silicon detectors.

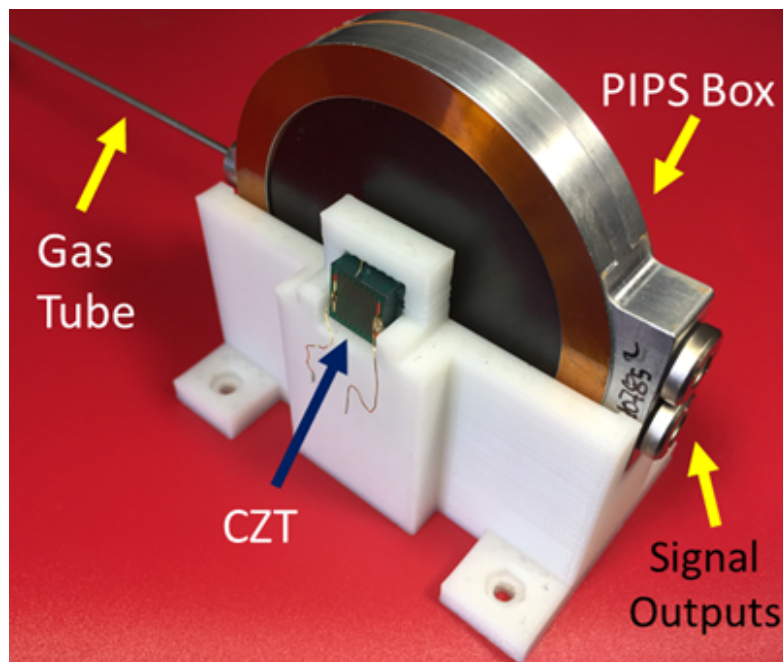


Figure 3-1: Final detector assembly showing CZT crystals coupled to the PIPSBox gas cell

3.2.1 Detector Functionality

Figure 3-2 shows a 3-D cross section for the PIPSBox/CZT detection system showing the gas cell, all four detectors, gas inlet and signal readout for the PIPSBox.

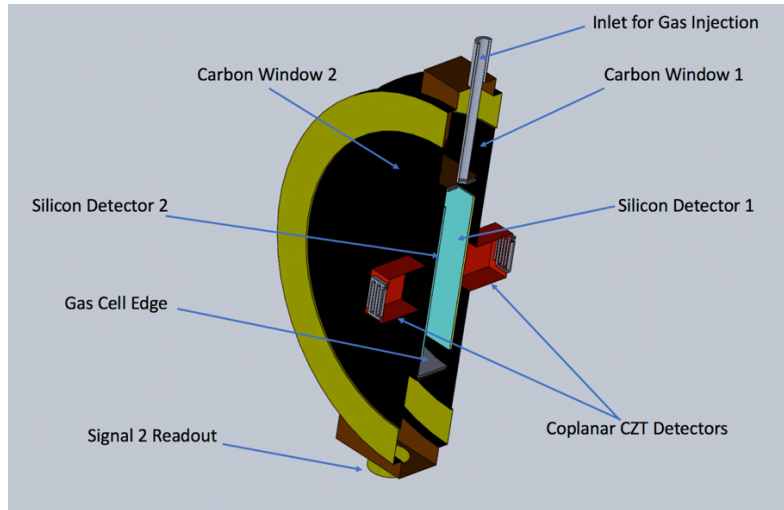


Figure 3-2: 3-D cross section of the PIPSBox/CZT detector

Figure 3-3 shows potential scenarios of beta-gamma coincidence events that can be observed inside the PIPSBox/CZT detection system. The digital processor will be sensitive to when these events occur in addition to triple coincidence events in the case of ^{133}Xe , and transfer pulse waveforms to MATLAB for plotting and further processing.

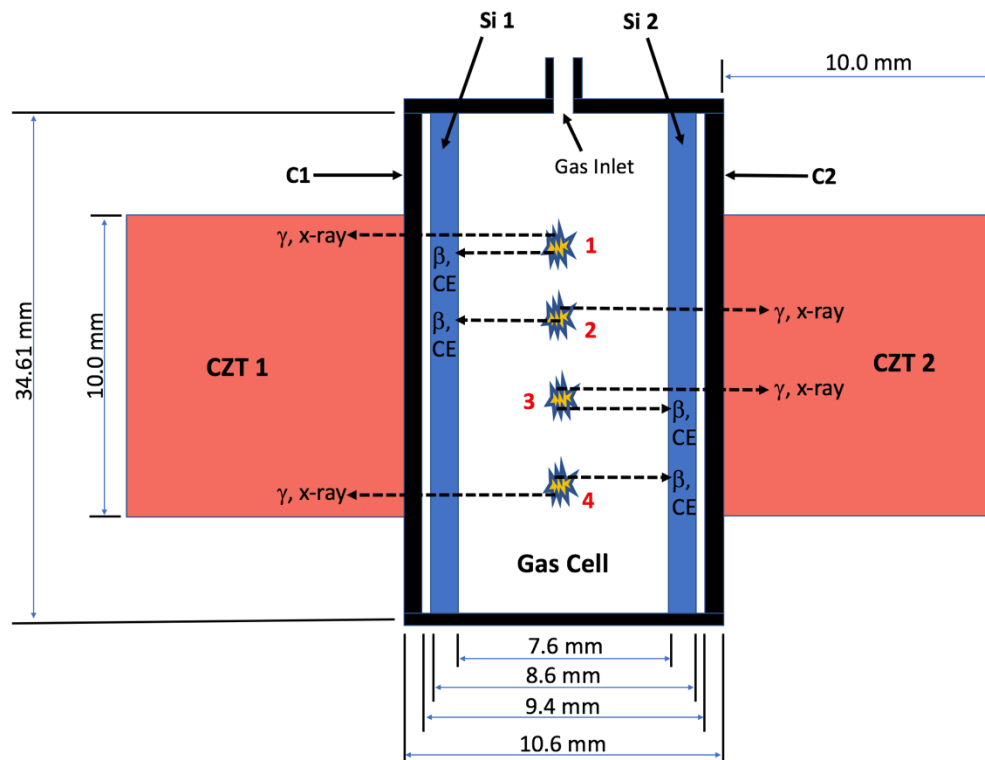


Figure 3-3: PIPSBox/CZT coincidence scenarios (with detector dimensions; not scaled)

3.3 Detector Simulation

To evaluate the expected performance of the detection system, it was simulated using MCNP to acquire various parameters necessary to calculate the Minimum Detectable Concentration (MDC) such as coincidence detection efficiency for all four radionuclides of interest.

3.3.1 MCNP Simulations, PTRAC, Expected Coincidence Events

Figure 3-4 shows a schematic of the PIPSBOX obtained by the manufacturer (Canberra) to be used in the MCNP modeling.

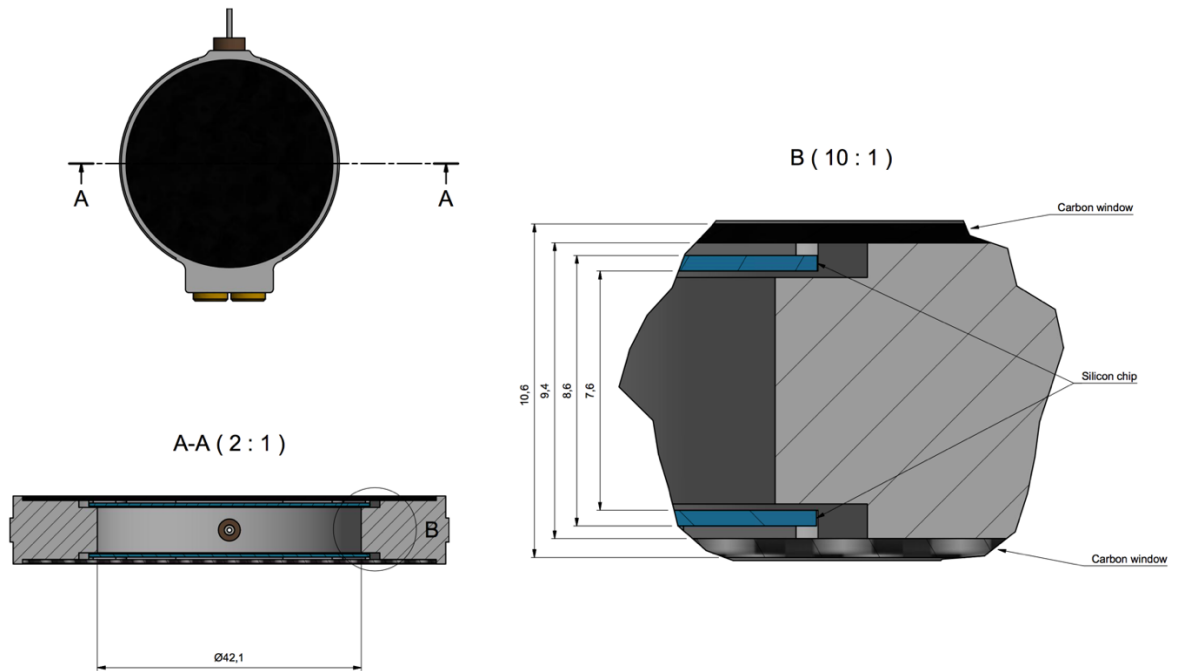


Figure 3-4: PIPSBox schematic obtained from the manufacturer with actual dimensions to be used in MCNP modeling

The PIPSBox/CZT detector was simulated using MCNP6. Cell dimensions were obtained from the manufacturer to ensure that the results will mimic the actual detection system. To obtain simulation results, several steps were followed:

1. Create MCNP input files for all four radioxenons;
2. Generate PTRAC files that record particle interactions and energy deposition from generation to termination;
3. Parse the data with Python codes;
4. Produce coincidence files for expected scenarios using Python codes;
5. Generate 2D spectrum for radioxenon using MATLAB.

In the first step, ten MCNP input files were created. Table 3-1 shows the files made for each radioxenon emission of interest.

Table 3-1: Description of MCNP files used to simulate the CZT-PIPSBox Detector

Radioxenon	No. of files	Radiation Simulated	No. of particles
^{131m}Xe	2	30 keV X-ray	1e7
		129 keV conversion electron	1e7
^{133m}Xe	2	30 keV X-ray	1e7
		199 keV conversion electron	1e7
^{133}Xe	4	30 keV X-ray	1e7
		45 keV conversion electron	1e7
		81 keV γ	1e7
		346 keV β	1e7
^{135}Xe	2	250 keV γ	1e7
		910 keV β	1e7

Each input file contained a command to generate particle tracking files (PTRAC) that are essential to identify where each particle has deposited its energy. A Python code was written to clean up and reduce the PTRAC files to a history number followed by the cell, in which the particle was terminated, and the amount of energy deposited at the time of termination. Another Python code was then used to parse the output of the first script and reduce it to only the coincidence events of interest. For example, when examining ^{131m}Xe , if particle #10 from the 129 keV conversion electron file was terminated in one of the silicon detectors, and particle #10 from the 30 keV X-ray file was terminated in one of the CZT detectors, this is considered one coincidence event. The same logic was applied to all four radioxenons, depending on the types of particles emitted in coincidence. Coincidence scenarios for each radioxenon are listed in Table 3-2. Based on the events listed in Table 3-2, MATLAB was used to generate 2D coincidence spectra that will be compared to expected signatures from all four

radioxenons. A complete description of how to work with MCNP and PTRAC files can be found in the PhD Dissertation of Lily Ranjbar [40]

. Two-dimensional scatter plots were generated by the simulation results obtained with broadening values applied to the peaks of interest. Broadening percentages were based on values found in literature [66] [69].

Table 3-2: Coincidence Scenarios for all radioxenons of interest

Expected Scenarios	Xenon	Event 1	Event 2	Event 3
1	^{131m}Xe	129 keV CE in Si-1	30 keV X-ray in CZT-1	n/a
2		129 keV CE in Si-1	30 keV X-ray in CZT-2	n/a
3		129 keV CE in Si-2	30 keV X-ray in CZT-1	n/a
4		129 keV CE in Si-2	30 keV X-ray in CZT-2	n/a
5	^{133m}Xe	199 keV CE in Si-1	30 keV X-ray in CZT-1	n/a
6		199 keV CE in Si-1	30 keV X-ray in CZT-2	n/a
7		199 keV CE in Si-2	30 keV X-ray in CZT-1	n/a
8		199 keV CE in Si-2	30 keV X-ray in CZT-2	n/a
9	^{133}Xe	346 keV β in Si-1	81 keV γ in CZT-1	n/a
10		346 keV β in Si-1	81 keV γ in CZT-1	n/a
11		346 keV β in Si-2	81 keV γ in CZT-2	n/a
12		346 keV β in Si-2	81 keV γ in CZT-2	n/a
13		346 keV β in Si-1	30 keV X-ray in CZT-1	n/a
14		346 keV β in Si-1	30 keV X-ray in CZT-2	n/a
15		346 keV β in Si-2	30 keV X-ray in CZT-1	n/a
16		346 keV β in Si-2	30 keV X-ray in CZT-2	n/a
17		45 keV CE in Si-2	30 keV X-ray in CZT-1	n/a
18		45 keV CE in Si-2	30 keV X-ray in CZT-2	n/a
19		45 keV CE in Si-1	30 keV X-ray in CZT-1	n/a
20		45 keV CE in Si-1	30 keV X-ray in CZT-2	n/a
21		346 keV β in Si-1	45 keV CE in Si-2	30 keV X-ray in CZT-1
22		346 keV β in Si-1	45 keV CE in Si-2	30 keV X-ray in CZT-2
23		346 keV β in Si-2	45 keV CE in Si-1	30 keV X-ray in CZT-1
24		346 keV β in Si-2	45 keV CE in Si-1	30 keV X-ray in CZT-2
25	^{135}Xe	910 keV β in Si-1	250 keV γ in CZT-1	n/a
26		910 keV β in Si-1	250 keV γ in CZT-2	n/a
27		910 keV β in Si-2	250 keV γ in CZT-1	n/a
28		346 keV β in Si-2	250 keV γ in CZT-2	n/a

3.3.1 Simulation Results

The CZT-PIPSBox detection system has four detectors. The x-axis in the 2D plot was dedicated to energies released by beta particles and conversion electrons in either silicon 1 or silicon 2. The y-axis was dedicated to energies released by gamma and X-rays in either CZT 1 or CZT 2.

3.3.1.1 ^{131m}Xe

^{131m}Xe emits a 30 keV X-ray in coincidence with 129 keV conversion electron. Figure 3-5 shows ^{131m}Xe 2D coincidence scatter plot generated in MATLAB. Events are populated along the 30 keV line for the CZT detectors because conversion electrons can backscatter between the two silicon detectors and thus do not deposit their full energy all the time. However, along that same line, there is a cluster of events around the 129 keV energy for silicon detectors. This is a result of absorbing 30 keV X-rays and 129 keV conversion electrons that almost deposit their full energies in the CZT and silicon detectors respectively. Another populated line below the 10 keV energy for the CZTs can be observed with a second cluster around the 129 keV energy on the silicon axis. This line is a result of the Cd and Te escape peaks as they leave the CZT and do not release their energies. Table 3-3 lists the characteristic X-rays from Cd, Zn and Te.

Simulated Beta-Gamma Coincidence Events for ^{131m}Xe

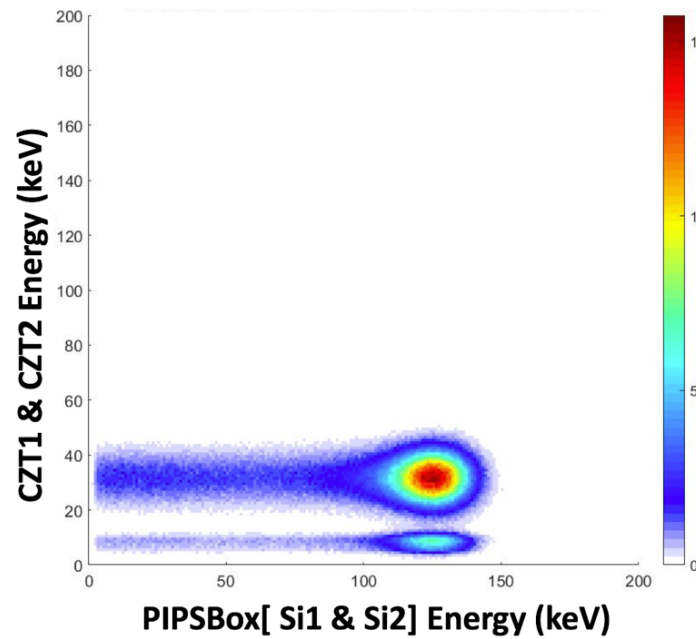


Figure 3-5: Simulated beta-gamma coincidence events for ^{131m}Xe

Table 3-3: Energies of the characteristic X-rays and K edges of Cd, Zn, and Te

Element	K edge (eV)	$K_{\alpha 1}$ (eV)	$K_{\alpha 2}$ (eV)	$K_{\beta 1}$ (eV)	$L_{\alpha 1}$ (eV)
Cd	26.72	23.173	22.984	26.095	3.134
Zn	9.66	8.638	8.615	9.572	1.0117
Te	31.80	27.472	27.201	30.995	3.769

3.3.1.1 ^{133m}Xe

^{133m}Xe emits 30 keV X-ray in coincidence with 199 keV conversion electron.

Figure 3-6 shows ^{133m}Xe 2D coincidence scatter plot. Events are populated along the 30 keV line for the CZT detectors. At the end of the line, there is a cluster of events surrounding the 199 keV energy. These are events from full X-ray energy absorption

and complete conversion electron deposition. Similar to the ^{131m}Xe case, there is a populated line below the 10 keV energy for the CZTs with another cluster on the same line around the 199 keV energy of the silicon detectors caused by the Cd and Te escape peaks.

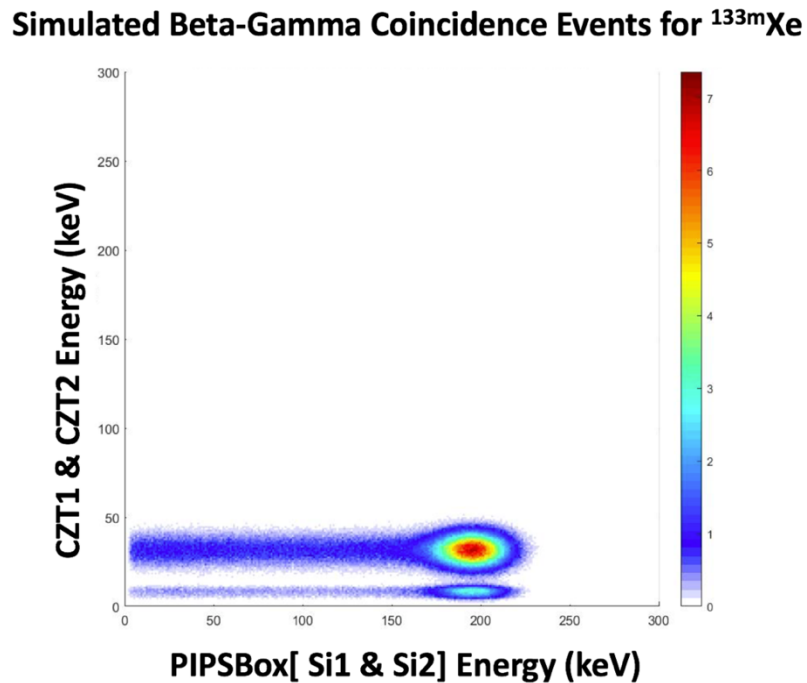


Figure 3-6: Simulated beta-gamma coincidence events for ^{133m}Xe

3.3.1.1 ^{133}Xe

^{133}Xe decays in two different ways: 346 keV beta in coincidence with 81 keV gamma ray, and 346 keV beta in coincidence with 30 keV X-ray and 45 keV conversion electron. These two decays have different intensities, but the second coincidence branch is more likely to take place in the decay process. The simulated 2D coincidence scatter plot in Figure 3-7 confirms the difference in coincidence intensities. Events on the 81 keV gamma line are less populated than the events on the 30 keV X-ray line as stated

earlier. On the 81 keV line, beta particles extend up to the maximum energy, 346 keV. However, on the 30 keV line, events extend up to 391 keV because both beta particle and the 45 keV conversion electron can be absorbed in the same silicon detector. The Cd and Te escape peak line is observed again on this plot and is clustered around the 30 keV energy.

Simulated Beta-Gamma Coincidence Events (Double & Triple) for ^{133}Xe

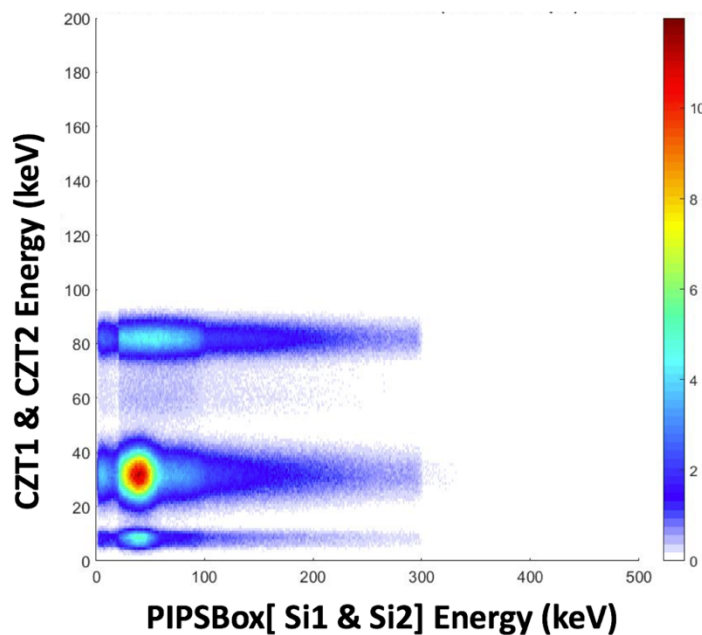


Figure 3-7: Simulated beta-gamma coincidence events for ^{133}Xe

Figure 3-8 shows the simultaneous situation when the CZT-PIPSBox detector is injected with activated ^{132}Xe . Both ^{133}Xe and $^{133\text{m}}\text{Xe}$ will decay inside the gas cell and the result will be the 2D scatter plot of $^{133\text{m}}\text{Xe}$ super-imposed on the 2D scatter plot of ^{133}Xe .

Simulated Beta-Gamma Coincidence Events (Double & Triple) for ^{133}Xe & $^{133\text{m}}\text{Xe}$

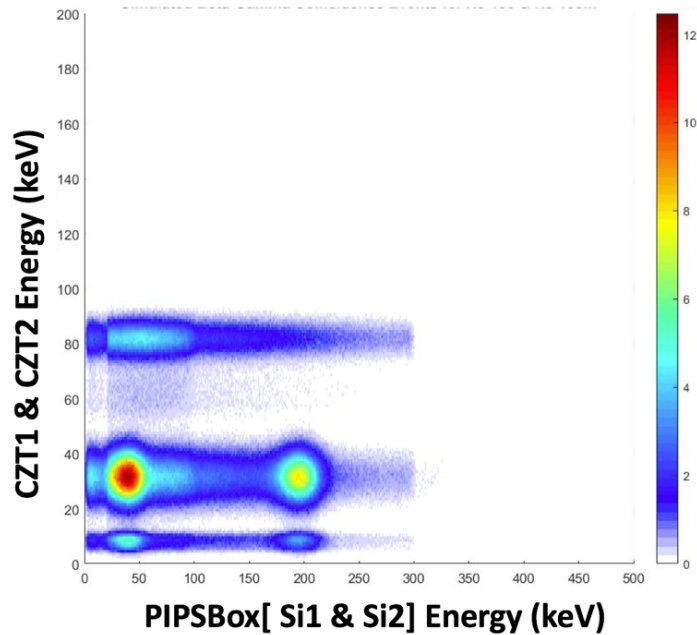


Figure 3-8: Simulated beta-gamma coincidence events for ^{133}Xe and $^{133\text{m}}\text{Xe}$

3.3.1.1 ^{135}Xe

Figure 3-9 shows the 2D scatter plot for ^{135}Xe . Events are populated around the 250 keV gamma line and are distributed along the beta energy distribution. It should be noted here that the beta distribution line tapers off significantly in intensity between 600 and 700 keV. This is because the emission probability of high energy betas is lower than the emission probability of lower energy betas, as well as because the silicon detectors are 500 μm thick and thus do not consistently absorb the full energy of a 910 keV beta particle.

Simulated Beta-Gamma Coincidence Events for ^{135}Xe

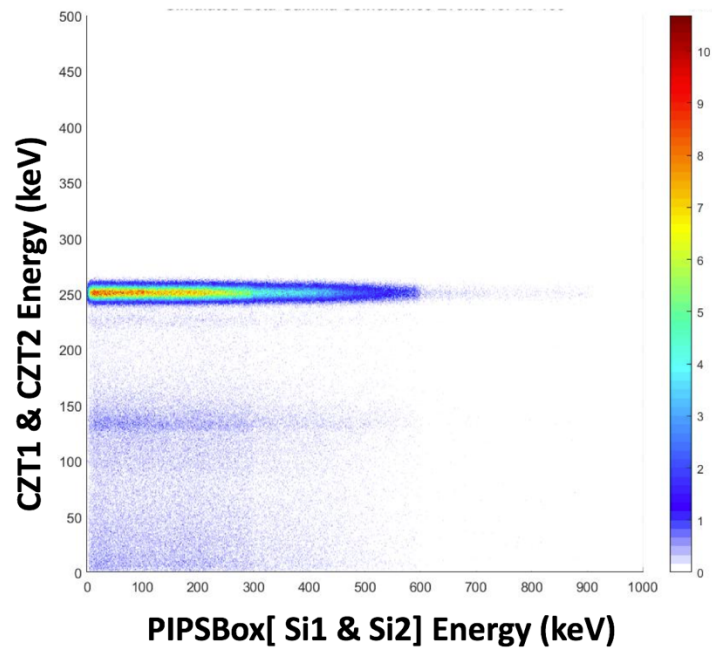


Figure 3-9: Simulated beta-gamma coincidence events for ^{135}Xe

3.3.1.1 Coincidence Detection Efficiency Calculations

Coincidence events generated in MCNP were used to calculate the coincidence detection efficiency of the system. The total number of coincidence events simulated by MCNP was multiplied by the coincident branching ration of each radioxenon decay to estimate the coincidence detection efficiency of the system. Table 3-4 lists the coincidence detection efficiency of the PIPSBox/CZT system for all four radioxenons:

Table 3-4: Simulated coincidence detection efficiency for the PIPSBOX/CZT system

Isotope	β - γ coincidence Scenarios	Coincident Branching Ratio	$\epsilon_{\beta \cdot \gamma}$ [MCNP]
^{131m}Xe	129 keV C.E. & 31 keV X-ray	0.561	0.0459
^{133m}Xe	199 keV C.E. & 31 keV X-ray	0.584	0.0324
^{133}Xe	346 keV β & 81 keV γ ray	0.372	0.0253
	346 keV β , 45 keV C.E. & 31 keV X-ray	0.489	0.0545
^{135}Xe	910 keV β & 250 keV γ ray	0.90	0.0411

3.4 The 2-Channel Digital Pulse Processor (DPP2.0)

DPP2 is a two-channel digital pulse processor based on an FPGA (Spartan 3) from Xilinx and two ADC's designed and built by Dr. Abi Farsoni at OSU. Users can implement their own custom firmware to adapt the DPP2 for a specific detection configuration. The processor has a sampling rate of 200 MHz with 12-bit ADC resolution. A complete description of how DPP2 works, FPGA modules MATLAB script, etc can be found in Lily Ranjbar PhD dissertation [66]. Figure 3-10 shows a photo of DPP2.

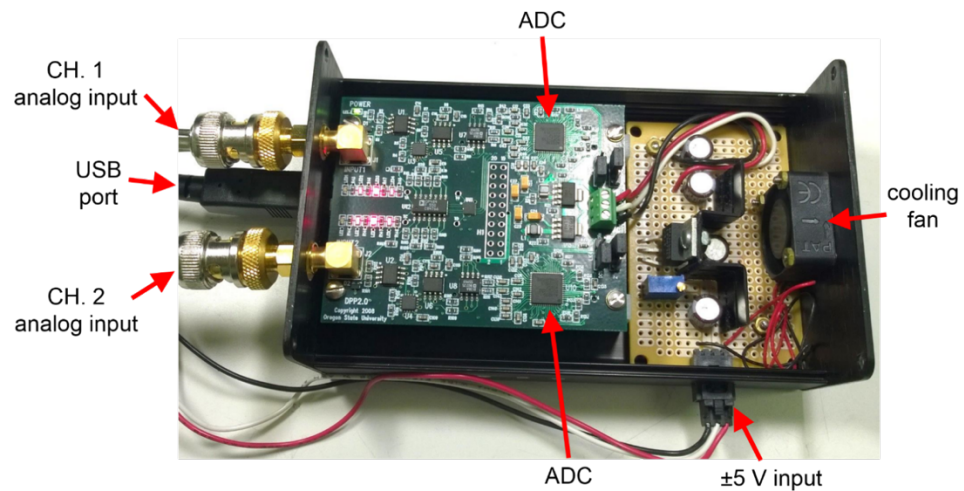


Figure 3-10: FPGA-based Digital Pulse Processor DPP2.0 with 200 MHz sampling frequency developed at OSU [66]

3.5 The 8-Channel Digital Pulse Processor (DPP8.0)

DPP8 is an eight-channel digital pulse processor based on an eight-channel ADC from Analog Devices and a high-performance FPGA from Xilinx that has been designed and built at the radiation detection group lab by two Ph.D. students under the supervision of Dr. Abi Farsoni. Users can implement their own custom firmware to adapt the DPP8 for a specific detection configuration. A custom-built analog-to-digital conversion (A/D) board was used in addition to the FPGA board acquired from Opal Kelly. The processor has a sampling rate of 125 MHz with 14-bit resolution. Because we can implement any custom firmware to work with a one channel/detector up to 8 channels/detectors, we can implement beta-gamma coincidence counting in real-time. The first step in this research will be to transfer coincidence pulses to the PC side and

process them offline. An explanation of the firmware and the MATLAB script to control the processor will be discussed later. Figure 3-11 shows a photo of DPP8.

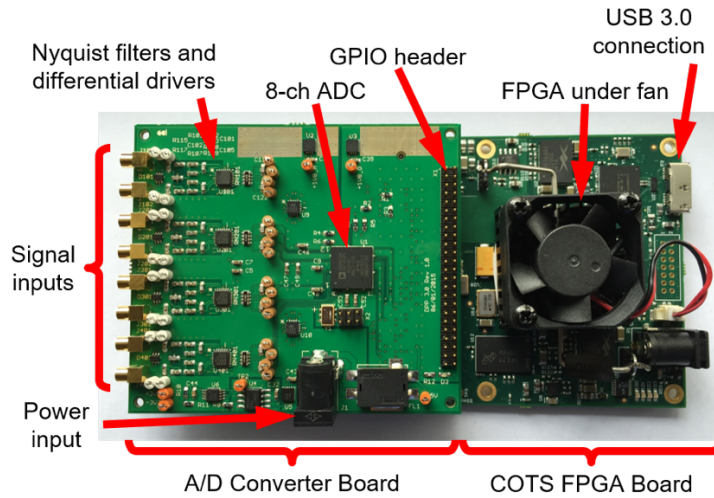


Figure 3-11: DPP8 with the analog to digital converting board (left) and the FPGA board (right)

A basic diagram of the firmware architecture is shown in Figure 3-12.

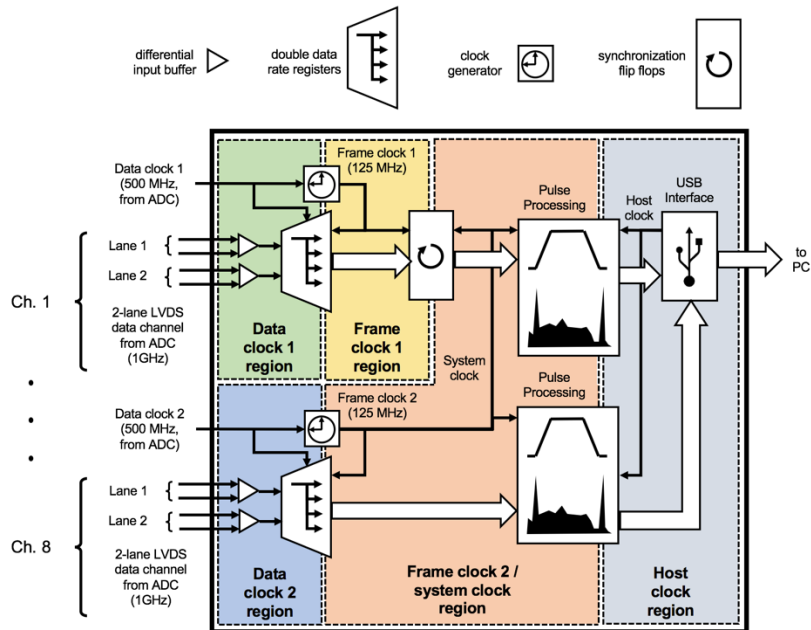


Figure 3-12: Diagram of the DPP8 basic firmware architecture

3.5.1 Readout Electronics

3.5.1.1 Analog Electronics

The detection system has a combination of analog and digital components. A diagram of the circuitry required to read out signals from a coplanar CZT detector is shown in Figure 3-13 [66]. Signals from the collecting and non-collecting grids will be fed into Amptek A250F charge-sensitive preamplifiers, which will feed into an analog subtraction circuit. This will result in an integrated pulse that will be digitized in the 8-channel ADC on the custom made board [70]. Each CZT requires two charge-sensitive preamplifiers and the circuit in Figure 3-13 is duplicated for the other CZT.

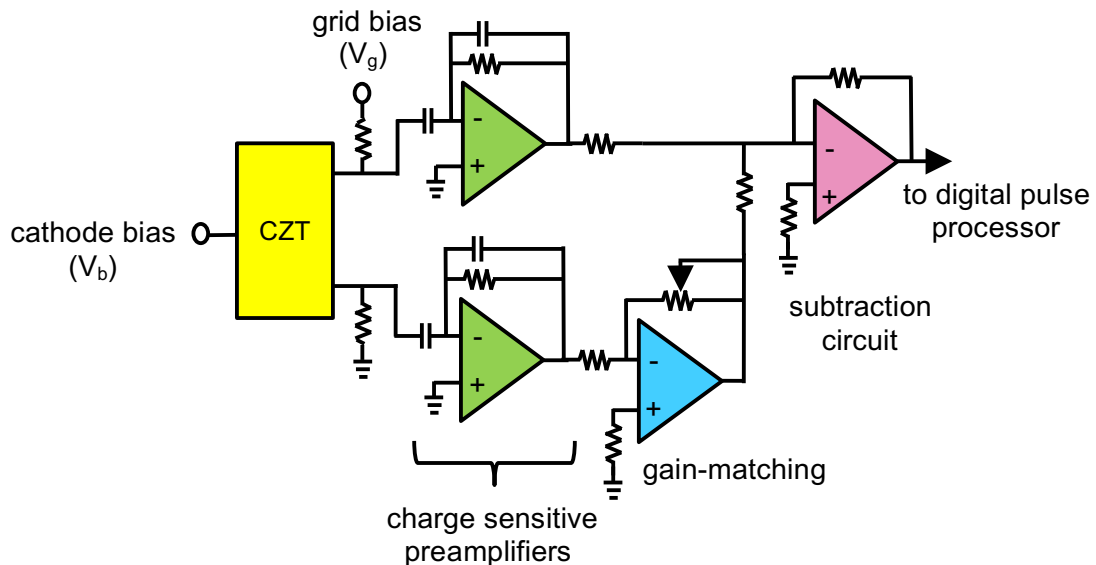


Figure 3-13. Block diagram of the required electronics to read one coplanar CZT detector used in this research, same in Ranjbar et al. work[66]

High voltage is applied to the cathode to move charge carriers throughout the detector, where another small voltage is applied between the collecting and non-

collecting grids to direct the electrons towards the collecting grid. The small voltage will have negative polarity to repel the electrons towards the collecting grid. As the electrons move towards the anode, they induce charge on both collecting and non-collecting grids. The signal is then subtracted using the subtraction circuit shown to the far right in Figure 3-13. Coplanar designs transform CZT crystals to be sensitive to only single charge carriers (electrons), overcoming hole trapping problems inside the bulk of the CZT crystal. A potentiometer is used to adjust the gain between the anode grids. Gain adjustment helps to compensate for electron trapping. Eventually, the generated signal is independent of the depth of interaction inside the CZT detectors. The subtracted signal will be digitized and sent to the FPGA for further processing.

In the case of the silicon detectors in the PIPSBox, no subtraction circuit is required to readout the signals coming of the silicons. The PIPSBox has LEMO connectors, one for each silicon, that are fed directly to the charge-sensitive preamplifier input. It should be noted that silicon detectors rely on collecting both electrons and holes since they don't have electron and hole trapping problems as in the case of CZT detectors. Additionally, silicon detectors are reverse biased to create the depletion region inside the silicon detector so that charge carriers are created and collected to the proper side when radiation interacts with silicon.

3.5.1.2 FPGA Firmware and MATLAB Script

To control DPP8, the user must implement an 8-channel coincidence firmware and write a MATLAB script to communicate with the FPGA. The **ADC interface**

module controls and digitizes all eight analog waveforms coming into the FPGA device. For pulse processing, the FPGA firmware used in this research is made of **four separate** modules connected under a top module. The first module is the **Trigger**, which passes the ADC data through a triangular filter and compares the incoming data with a threshold set by the user in MATLAB. The data then goes to the second module, **Oscilloscope**. This module transfers the data of the triggered channels to the PC side depending on the user input. The user might ask to transfer one channel or transfer more than one channel. Under the same module, there is a coincidence part. This part monitors coincidence between all 8-channels depending on a coincidence window and a specific pattern set by the user in the MATLAB script. Coincidence window determination will be discussed later. The third module is **Histogram** module. In this module, the user can generate a histogram of one channel from the 8-channel. The free running histogram is generated in real-time inside the FPGA. A high-level flow chart of the MATLAB script used to program the FPGA and transfer pulses is shown in Figure 3-14. The figure shows two main steps the user must do to acquire data from the detection system. The first step is setup. The user here programs the FPGA with a bit file that contains a description of the firmware written in VHSIC Hardware Description Language (VHDL). Then, DAC level is set for all eight channels. Finally, trigger threshold values, conversion gain, trapezoidal shaping parameters for the free running histogram are set. The system is now ready to operate in any of the three modes shown in Figure 3-14. For this work, the functionality of oscilloscope coincidence mode is the most important part of the firmware design so it will be thoroughly discussed.

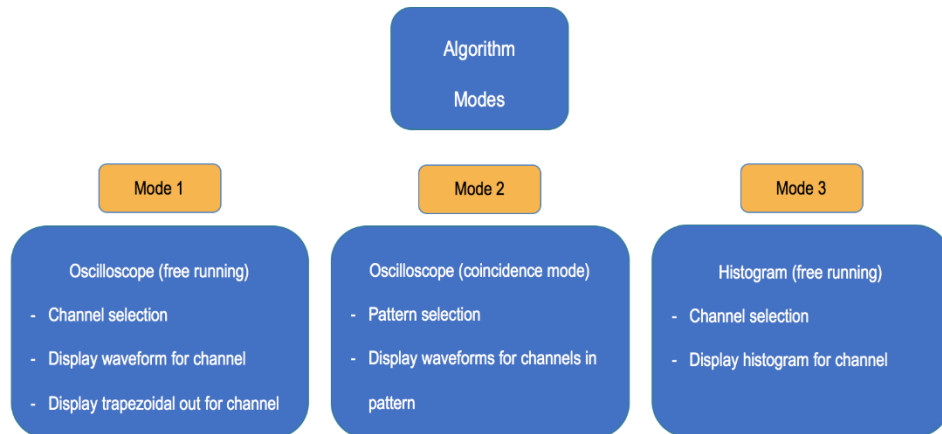


Figure 3-14: High-level flow chart of the MATLAB script used to transfer pulses from the FPGA

A state machine for the oscilloscope coincidence part is shown in Figure 3-15. When the user has set run mode to 3 (coincidence mode), the state machine moves from “idle” state to “reset.” In “reset” state, the coincidence window counter is reset and the 8-bit signal that contains coincidence channels is also reset. Then comes “start” state where the state machine is waiting to be triggered by any of the 8 channels/detectors. There is a *pattern enable* signal that is set to 01 to ensure that the channel initiating the coincidence event is registered. Once a trigger arrives, the state moves to “count” state where the coincidence window counter is enabled. In this state, the firmware waits for other channels to get triggered to create the *coincidence channels* signal. The user is able to set multiple patterns from the MATLAB script. If *coincidence channels* signal matches any of the patterns set by the user, the state machine moves to “coincidence assignment” state, where it indicates that a pattern has been found and the *pattern enable* signal is set to 10, which will keep the coincidence pattern until all coincidence pulses are read and transferred to the PC side. When the pulses are read, MATLAB sends a

read done signal to move the state machine to “coincidence reset” state, in which coincidence channels are reset and the coincidence counter is reset before the state machine moves to “start” state and look for another coincidence event. MATLAB also sends a signal to inform all 8 oscilloscope channel state machines to go back and wait for a new coincidence/trigger event.

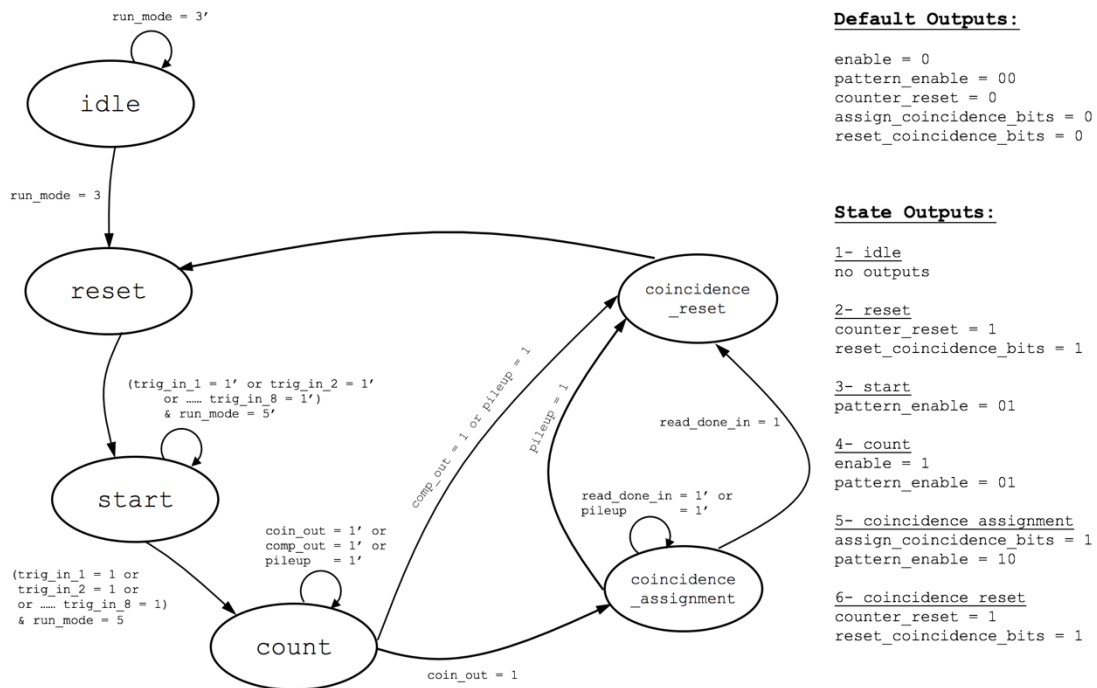


Figure 3-15: Coincidence state machine inside the firmware

Assuming that only one channel is triggered, the state machine will go from “start” state to “count” state, where the counter will count up to the duration of the coincidence window that is set by the user in MATLAB. After the coincidence window is over, the state machine moves to “coincidence reset” state and resets the counter and the *coincidence channels* signal to look for a new coincidence event. The state machine

is also sensitive to pileup events. Pileup occurs if a channel is triggered twice during the time the FPGA is writing the channel's waveform. In the case of a pileup event, the state machine will throw away the *coincidence channels* and pulse waveforms associated with those channels and look for a new trigger to form a new coincidence event. The fourth and final module is the **USB interface**, which handles the FPGA-PC communications and data transfer.

Additional MATLAB scripts were written to generate 2-D coincidence plots similar to the ones generated from the MCNP simulations. Inspecting the scatter plot allows us to observe the radiation signature of the radioxenon isotopes of interest and identify the associated ROIs. In addition to coincidence plots, the script also generates 1D gated spectra for coincidence beta and gamma events.

3.6 Expected Pulse Amplitudes from All Four Detectors

To ensure that pulses generated by the CZT and silicon detectors can be displayed fully within the 14-bit dynamic range of the ADC inside DPP8, the first step before using the preamplifiers was to calculate the expected charge generated from both detectors per keV of radiation deposited energy. Equations 3-4 and 3-5 were used to calculate the expected amplitudes per keV of deposited energy in the detectors:

$$Q = \frac{E}{\varepsilon} \times q \quad (3-4)$$

$$V = \frac{Q}{C} \quad (3-5)$$

Where Q is the charge generated per energy deposition E , q is the charge of an electron, ε is the energy required to create an ion pair for that particular material, C is the capacitance of the preamplifier used in the circuit, and V is the voltage amplitude of the resultant pulse. Using these equations with $\varepsilon_{Si} = 3.61 \times 10^{-3}$, $\varepsilon_{CZT} = 4.64 \times 10^{-3}$, and a capacitance of 0.25 pF, silicon detectors will generate pulses with amplitude of 0.1772 mV/keV of deposited energy, and CZT detectors will generate pulses with amplitude of 0.138 mV/keV of deposited energy.

Table 3-5 lists the expected amplitudes from radiation emitted by all four radioxenons of interest (^{131m}Xe , ^{133m}Xe , ^{133}Xe , and ^{135}Xe), in addition to radiation emitted by a lab check source (^{137}Cs) that is used in the calibration process. Note that we assume the voltage produced is independent of type of radiation, i.e.: the electron produces the same voltage as a photon.

Table 3-5. Expected amplitudes from incident radiation on the silicon and CZT detectors

Energy (keV)	V_{Si} (mV)	V_{CZT} (mV)
22	3.2494	2.53
30	4.431	3.45
45	6.6465	5.175
81	11.9637	9.315
129	19.0533	14.835
199	29.3923	22.885
250	36.925	28.75
346	51.1042	39.79
662	97.7774	76.13
910	134.407	104.65

The 910 keV beta emitted by ^{135}Xe generates the largest pulses, with a maximum amplitude of ~ 135 mV. The baseline of the silicon pulse waveforms should thus be set to allow for full capture and display of these pulses. Baseline is adjusted by changing the pulse digital-to-analog (DAC) offset value.

3.7 Detector Assembly

The detection system is now assembled and placed inside an aluminum box to shield from electromagnetic radiation and light. The box includes six preamplifiers, four for the CZT detectors and two for the silicon detectors. Two subtraction circuits and two potentiometers are placed inside the box to adjust the CZT gain. The gas inlet was brought out of the box so experimental conditions won't change as the radionuclide experiments are performed. Figure 3-16 shows a top view of the PIPSBBox/CZT detectors in the plastic holder secured in the aluminum. Figure 3-17 shows CZT1 and silicon1 side inside the box and Figure 3-18 shows CZT2 silicon2 side.

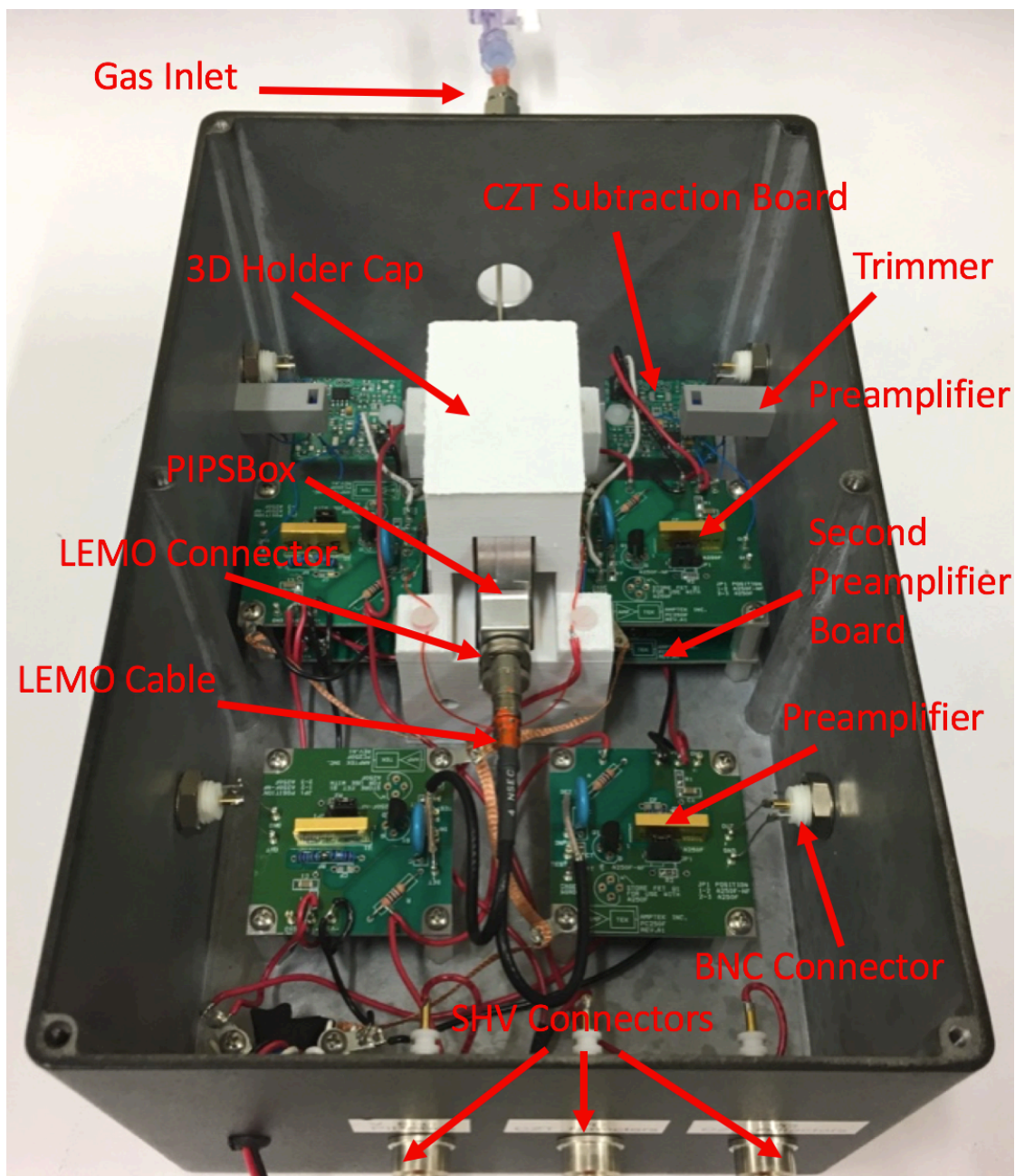


Figure 3-16: PIPSBox/CZT detection system and readout electronics inside the aluminum box

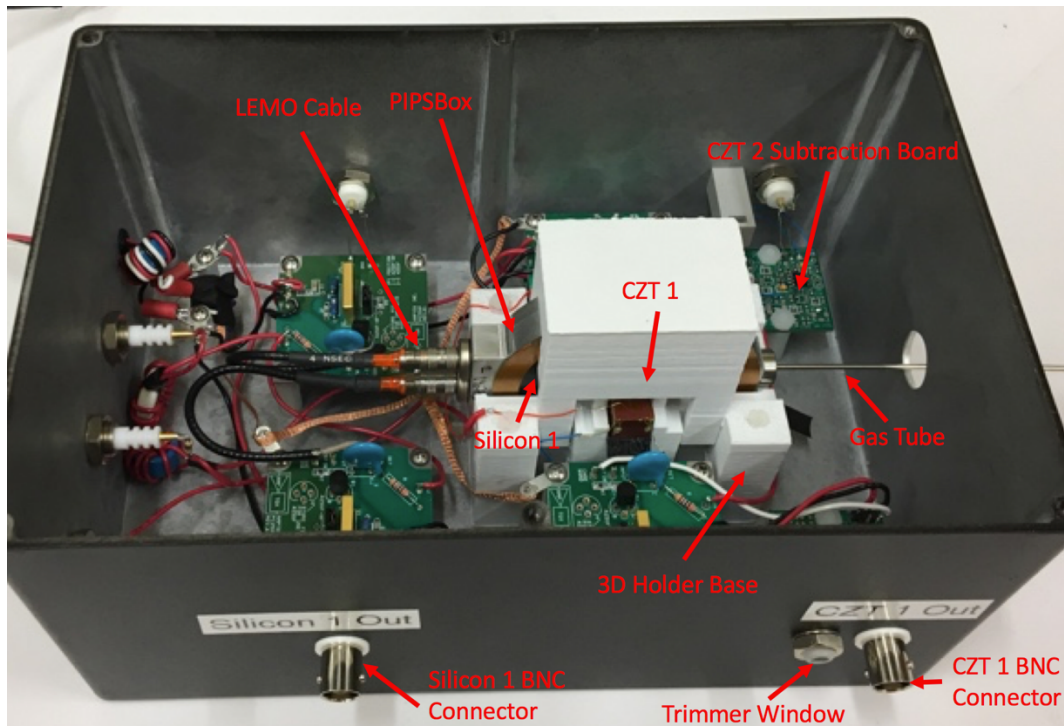


Figure 3-17: PIPSBox/CZT inside the aluminum box (CZT1 side)

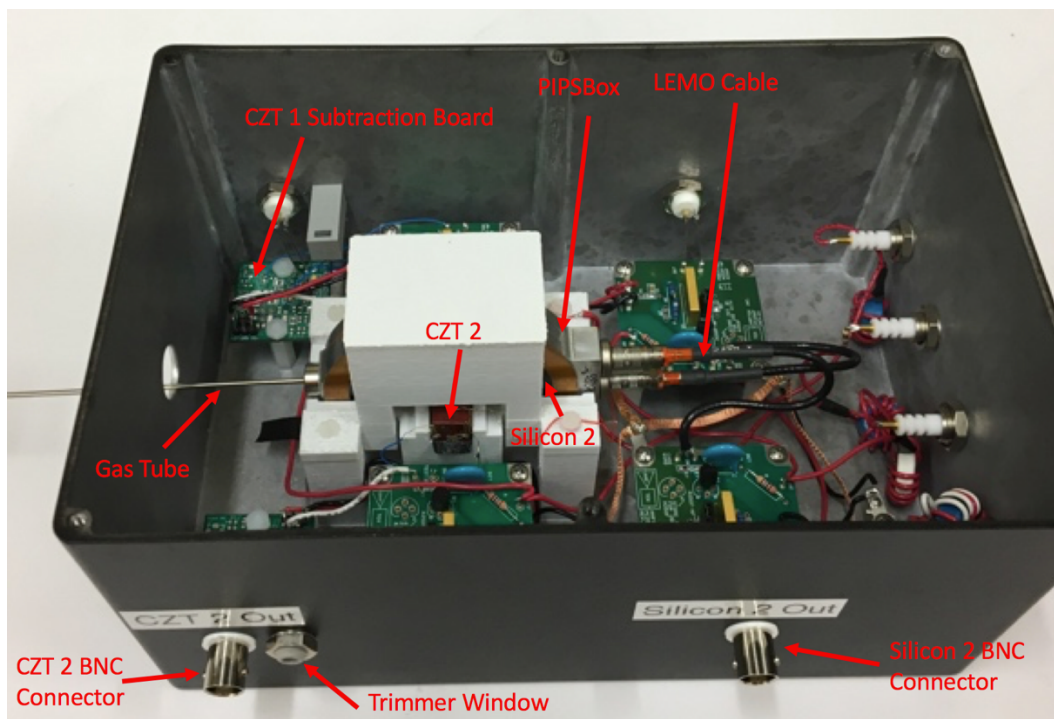


Figure 3-18: PIPSBox/CZT inside the aluminum box (CZT2 side)

4. Results and Discussion

4.1 Detector Characterization

The characterization process was accomplished using DPP8 and was comprised of three main tasks:

1. setting the best operating voltages for both the coplanar CZT detectors and the silicon detectors
2. finding the best trigger module coefficients to trigger the system with low energy radiation (30 keV X-ray for CZT and 45 keV conversion electron for silicon)
3. setting the best shaping parameters (peaking time and flat-top time) for the trapezoidal filter to achieve the best resolution for CZT and silicon detectors in off-line processing

4.1.1 CZT Calibration and Detection Parameters

A ^{137}Cs source was used to characterize the $1 \times 1 \times 1 \text{ cm}^3$ coplanar CZT detectors. ^{137}Cs decays by emitting a 662 keV gamma ray and a 30 keV X-ray. Both energies are important for radioxenon measurements because the 662 keV gamma illustrates the detector response for high energy gammas (250 keV gamma in the case of ^{135}Xe), and the 30 keV X-ray demonstrates the detection system capability to detect low energy X-rays (30 keV X-rays in the case of $^{131\text{m}}\text{Xe}$ and $^{133\text{m}}\text{Xe}$).

Energy resolution is important because it plays a vital role in MDC calculations. The smaller the energy resolution, the smaller regions of interests (ROIs) on the 2D coincidence spectrum, which will reduce the MDC value by reducing unwanted

background coincidences as well as reducing the interference between ROIs at similar energies. Several parameters had to be determined and tested to achieve the lowest resolution possible for the 662 keV energy peak. These parameters were:

1. CZT detector bias (anode grid and cathode)
2. Triangular filter parameters for trigger module inside the FPGA (number of coefficients)
3. Trigger threshold value
4. DAC value (offset setting)
5. Trapezoidal filter parameters known as shaping parameters (peaking time and flat time for energy measurements)
6. Gain value for each CZT (potentiometer resistance)

The coplanar CZT detectors are the same ones used with the CASP system [67], so the same cathode and grid voltages were used, -35 V and -1000 V respectively. The preamplifiers are also similar to those used with the CASP system, so they were biased at ± 6 V. The initial trigger threshold module utilized 32 coefficients in a trapezoidal shape, 12 ones, 8 zeros, 12 negative ones. Each coefficient represents one time step (a sample) with a frequency equal to the processor sampling frequency. The way trigger filter works is that it produces a response to pulse waveforms generated by radiation interaction inside the detector. The more coefficients added to the peaking time of the trigger filter, the greater the filter response is to the incoming pulse as shown in Figure 4-1. Therefore, it is necessary to have the right number of coefficients so that the system is sensitive to small pulse amplitudes generated by low energy radiation like 30

keV X-ray from ^{137}Cs . Having a trigger filter with zeros padded between the positive and negative coefficients in a trapezoidal shape will allow the system to keep the same threshold response for extended time equal to the number of zeros, samples, in the filter flat-top time. Setting the right threshold value is very important for measurements. If the threshold value is set too high, small pulse amplitudes won't surpass it and the system will not be sensitive to low energy radiation.

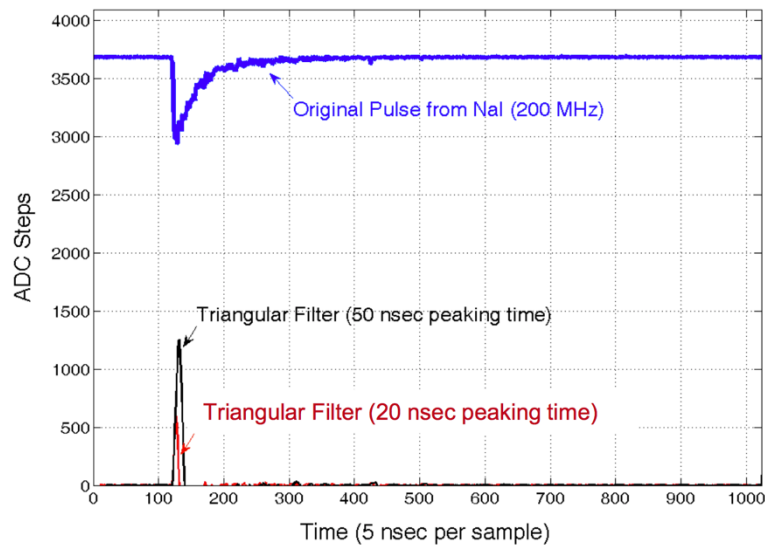


*Figure 4-1: Triangular filter response to a NaI(Tl) pulse with 20 nsec peaking time in **red** 50 nsec peaking time in **black**. The filter response is greater to the same pulse amplitude with a longer peaking time [RHP 537, Digital Radiation Measurement and Spectroscopy, Oregon State University, Dr. Abi Farsoni]*

The generated ^{137}Cs spectrum showed all the expected features: a 662 keV peak, a Compton edge at approximately 480 keV, a back-scatter peak at 190 keV, and a 30 keV peak. The 30 keV peak was not symmetrical (Figure 4-2). Experiments showed that that 96 nsec peaking time for the trigger filter is not enough to capture all pulses responsible for generating the 30 keV peak, since those pulses had very small filter

response, which did not surpass the threshold value. A trigger filter with longer peaking time would allow the system to capture more low energy pulses and distinguish them from electronic noise.

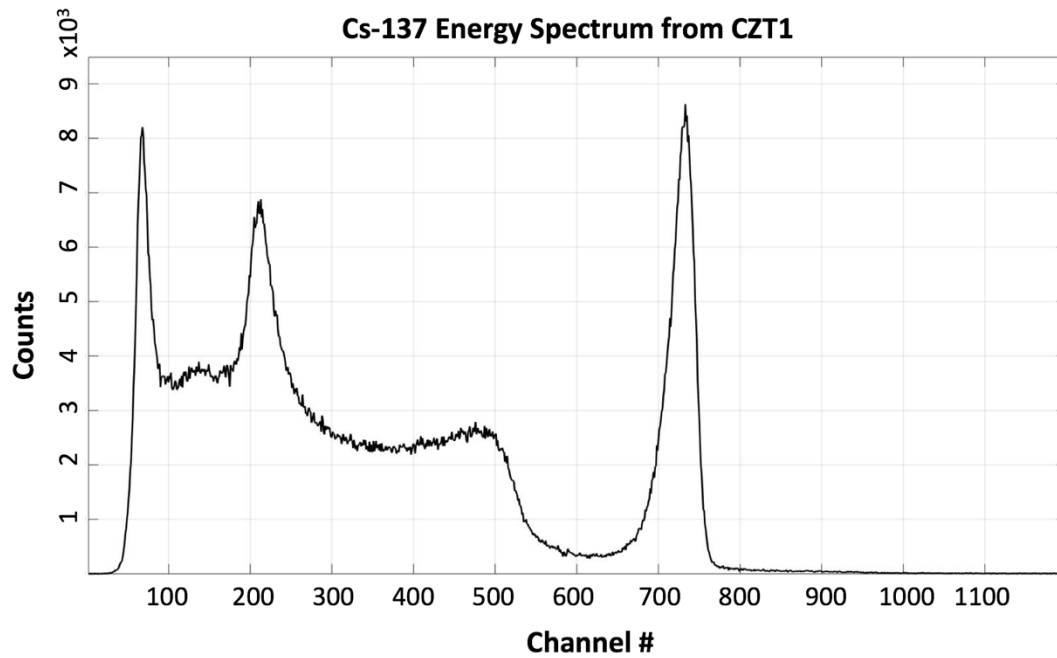


Figure 4-2: ^{137}Cs spectrum with an asymmetric 30 keV peak

To resolve this problem, a new trigger filter module was created with 320 nsec peaking time (40 ones, 10 zeros, 40 -ones). The generated 30 keV peak was symmetric, as shown in Figure 4-3. Multiple trigger threshold values were tested and the number of valid pulse waveforms was observed to assess at what point noise stops triggering the system. Once the appropriate threshold value was found, it was used throughout the characterization process.

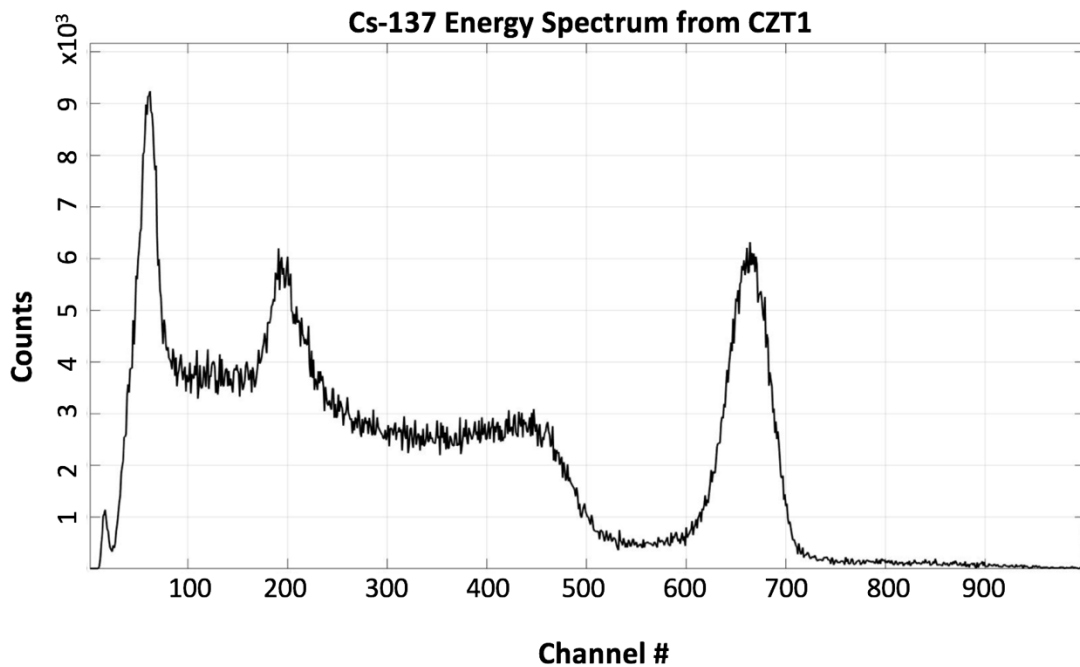


Figure 4-3: ^{137}Cs spectrum with a symmetric 30 keV peak

The shaping parameters for the trapezoidal filter used in energy histogram generation were determined next. The peaking time of the trapezoidal filter must be long enough so that it flattens out noise components in the pulse waveform, but not so long as to affect the system count rate limit. The flat-top time should be greater than the pulse rise time to allow for accurate determination of pulse amplitudes. The acceptable flat-top time will improve the energy resolution [71]. The CZT pulses had a rise time of about 400-480 ns. The optimum flat-time was found to be 720 ns and the optimum peaking time was 1600 ns for both CZTs (Figure 4-4, Figure 4-5, Figure 4-6, and Figure 4-7). The best resolution for CZT1 was measured at **3.97% FWHM**, where CZT2 had a **4.31% FWHM** resolution. Shaping parameters were determined by taking several spectra. First, peaking time was held constant at 1.6 μs and flat-top time was

varied from 0 μsec to 1.6 μs (80 ns steps). Then, flat-top time was held constant at 720 ns and peaking time was varied from 1 μs to 8 μs (800 ns steps). Energy resolution and peak centroid channel were taken for each measurement. Energy resolution is the full width at half maximum (FWHM) of the counts peak at that energy unit. Peak centroid is the channel in the middle of the energy peak. The centroid channel should increase as the flat-top time increases, and should cease to significantly vary with increasing flat-top time once the flat-top time is enough to integrate the whole pulse as shown in Figure 4-6. Each spectrum had gross counts of 50,000 pulses to ensure good statistics in determining both the resolution and the energy channel centroid.

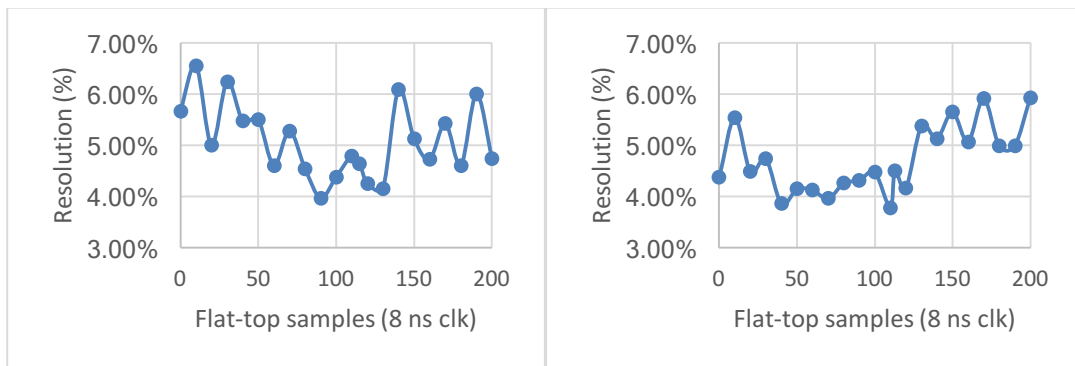


Figure 4-4: Energy resolution at different trapezoidal filter flat top times for CZT1 (left) and CZT2 (right); peaking time = 200 samples (sampling frequency = 125 MHz, = 8 ns period)

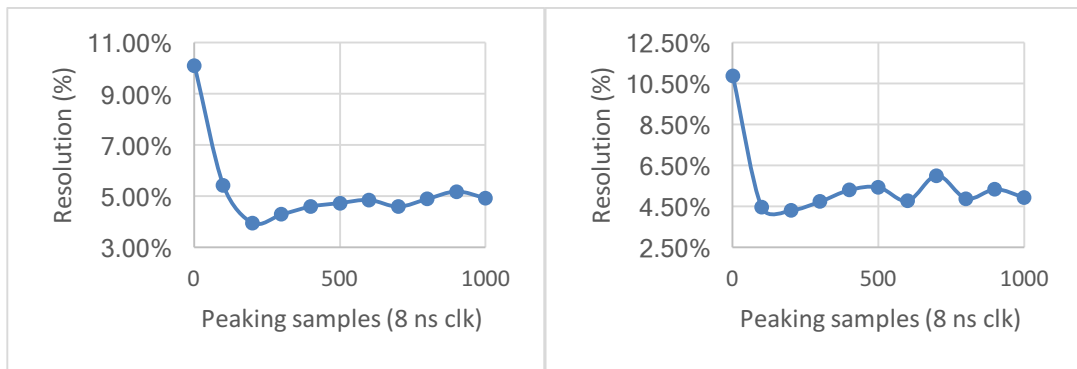


Figure 4-5: Energy resolution at different trapezoidal filter peaking times for CZT1 (left) and CZT2 (right); flat top time = 90 samples (sampling frequency = 125 MHz, = 8 ns period)

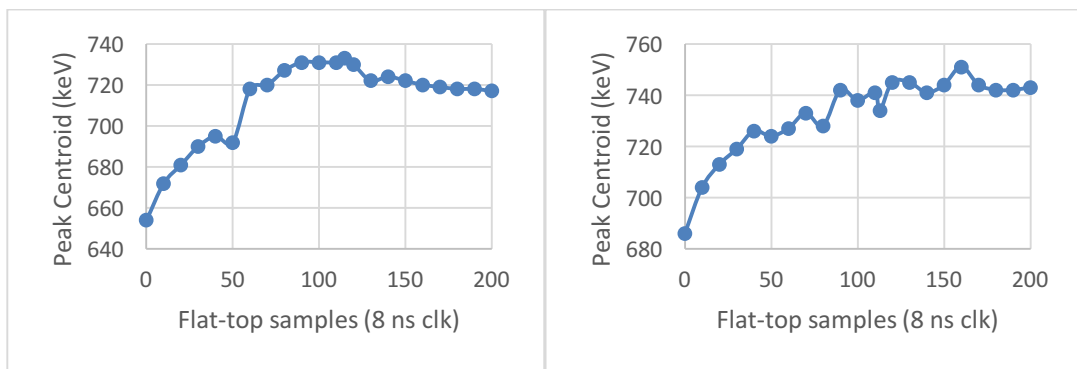


Figure 4-6: Peak centroid at different trapezoidal filter flat top times for CZT1 (left) and CZT2 (right); peaking time = 200 samples (sampling frequency = 125 MHz, = 8 ns period)

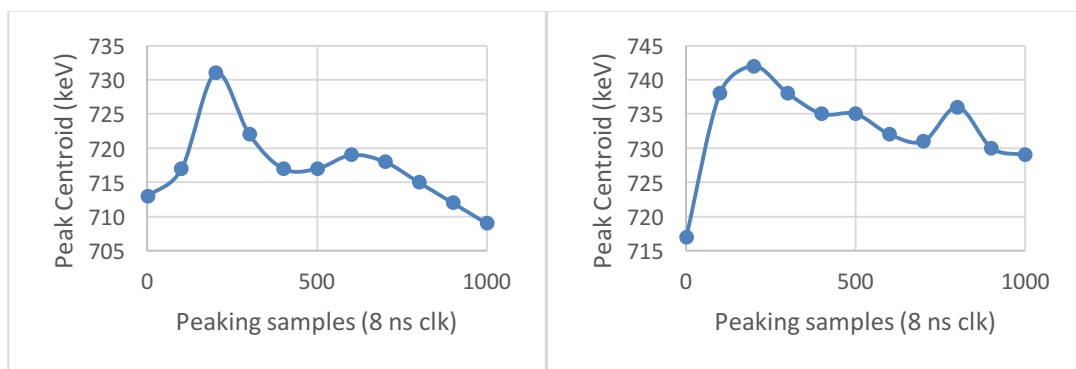


Figure 4-7: Peak centroid at different trapezoidal filter peaking times for CZT1 (left) and CZT2 (right); flat top time = 90 samples (sampling frequency = 125 MHz, = 8 ns period)

Finally, the trimmer resistance for the gain of non-collecting signal was changed in an effort to improve the resolution of the 662 keV peak. Gain adjustment helps overcome electron trapping inside the CZT crystals, which degrades the energy resolution of the detectors [72], [73]. The trimmer for each CZT was varied by taking the trimmer all the way to the maximum number of counter clockwise turns, and then turning it 1 full turn at a time ($\sim 90 \Omega/\text{turn}$ for a $1\text{k}\Omega$ potentiometer). Figure 4-8 shows the energy resolution vs. trimmer revolutions. The final trimmer values that produced the best resolution were 2.5 revolutions, which is equal to 220Ω for CZT1 and 2 revolutions for CZT2, which is equal to 180Ω .

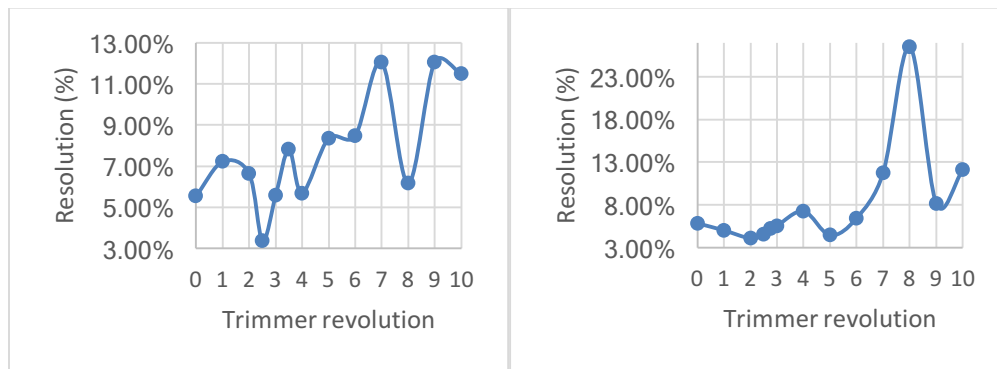


Figure 4-8: Energy resolution for CZT1 (left) and CZT2 (right) at different gain values

4.1.2 Silicon Calibration and Detection Parameters

Xenon $^{131\text{m}}\text{Xe}$ was used to characterize the silicon detectors. The reason to use $^{131\text{m}}\text{Xe}$ gas instead of lab check sources is that the silicon detectors are surrounded by two carbon layers ($600 \mu\text{m}$ thick) followed by a $400 \mu\text{m}$ air gap, which will prevent beta and alpha particles from interacting with the silicon detectors when lab check sources are externally used. X-rays can interact with the silicon detectors but the probability of

a 30 keV X-ray to interact with the silicon detectors is ~9% according to MCNP simulations. As stated earlier in this work, ^{131m}Xe decays by emitting a 24 keV Auger electron, 30 keV X-ray, 129 keV conversion electron and a 159-163 keV conversion electrons. The monogenetic electrons are perfect to characterize the silicon detectors. Enriched xenon 130 was activated in the OSU TRIGA reactor to make ^{131m}Xe . The gas was injected into the PIPSBox gas cell to start the characterization process. Several parameters had to be determined similar to the CZT detectors. These parameters were:

1. Silicon detector bias (revers bias voltage)
2. Triangular filter parameters for trigger module inside the FPGA (number of coefficients)
3. Trigger threshold value
4. DAC value (offset setting)
5. Trapezoidal filter parameters known as shaping parameters (peaking time and flat time for energy measurements)

The silicon detector data sheet suggests bias range of 100-150 V with negative polarity. The engineers at Canberra recommended the use of -130 V bias voltage. Multiple measurements have been performed to identify the best operating voltage. A bias of -145 V exhibited the best signal to noise ratio, so it was used for the rest of the experiments. The same triangular filter used with the coplanar CZT crystals is used with the silicon detectors. The filter was able to trigger the system with 30 keV X-rays in the case of CZT's, so it will be able to trigger the system with the lowest conversion electron energy from radioxenons, which is 24 keV. The threshold value was chosen so that it

would block the noise generated by the detectors and electronics but at the same time allow for the detection of the 24 keV electrons. The silicon detectors exhibited a large offset close to -1 V when examined using DPP8. Silicon pulses couldn't be displayed without adding a positive offset using the on-board DAC that had a -1 V, +1 V dynamic range. Adding the full +1 V offset from the DAC moved the silicon baseline back inside the dynamic range of the ADC at around 1000 ADC values. Because both the silicon and CZT detectors produce negative polarity pulses, this was not enough to display the full 2160 ADC values needed to display the 910 keV amplitudes from beta particles emitted by ^{135}Xe . To add additional positive offset, the DAC dynamic range was increased from -1V/+1V to -2V/+2V by changing the IC that controlled the DAC reference voltage. Adding another +1V allowed for the silicon base line to be moved well inside the ADC dynamic range. It is recommended to set the baseline at 80-85% of the maximum dynamic range values for proper display when dealing with pulses with negative polarity, so the baseline was set around 14,000 ADC values. Both CZT and silicon detectors have been coupled to the AMPTEK A250F charge sensitive preamplifiers. Both CZT and silicon detectors use BNC cables with 50 Ω resistance. In order to eliminate signal oscillating, the input resistance of DPP8 channels should match the resistance of the cables. The CZT detector signals had no oscillation, but the silicon detectors had oscillating issues in addition to the large offset. AMPTEK technical support recommended that we remove the 50 Ω resistors at the silicon channel inputs on DPP8. We followed the recommendation but that did not solve the oscillation problem. A small circuitry was designed to accomplish three goals: (1) isolate DPP8 silicon

channel inputs from the A250F silicon preamplifier outputs, (2) remove the offset generated by the silicon detectors, and (3) amplify the generated signal to improve the signal to noise ratio. Figure 4-9 shows the schematic of the circuit used, which consisted of an op-amp, resistors and capacitors. Notice that the amplification circuit uses an inverting input, which reversed the polarity of silicon pulses from negative to positive.

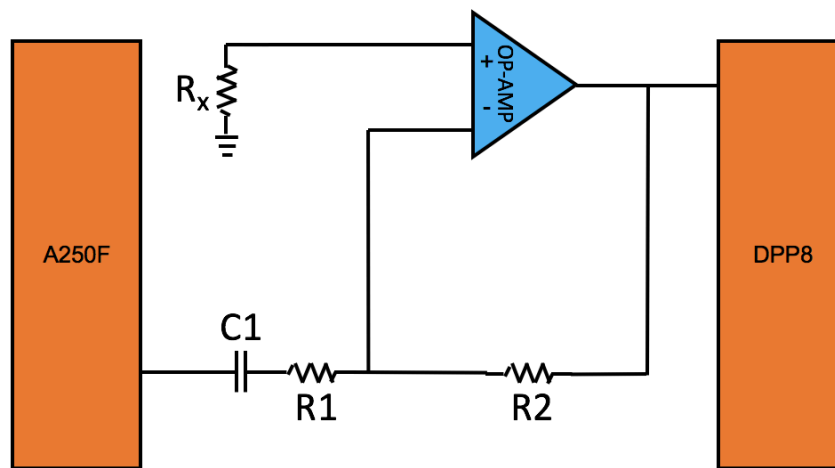


Figure 4-9: Amplification circuit connected to the silicon detectors output

The amplifier gain is determined by R1 & R2 values. Using equation 4-1:

$$Gain = \frac{R_2}{R_1} \quad (4-1)$$

The gain for the amplifier is 2.127, where R2 = 10 kΩ and R1= 4.7 kΩ. This means that each pulse amplitude will be doubled, which improved the signal to noise ratio. The value of Rx can be calculated using equation 4-2:

$$R_x = \frac{R_1 \times R_2}{R_1 + R_2} \quad (4-2)$$

Rx will be $3.19\text{k}\Omega$. The capacitor C1 had a value of 10 nF . This capacitor removed the -1V offset produced by the silicon detectors.

The shaping parameters for the silicon detectors were $2\text{ }\mu\text{s}$ for peaking time and $1.2\text{ }\mu\text{s}$ for flat-top time. The same process used in the determination of the CZT shaping parameters was used here. Several spectra were taken. First, flat-top time was kept constant at 720 ns and the peaking time was varied starting at 800 ns up to $8\text{ }\mu\text{s}$ (800 ns steps). For flat-top time determination, peaking time was kept constant at $2\text{ }\mu\text{s}$ and flat-top time was varied starting from 80 ns to $1.2\text{ }\mu\text{s}$ (80 ns steps).

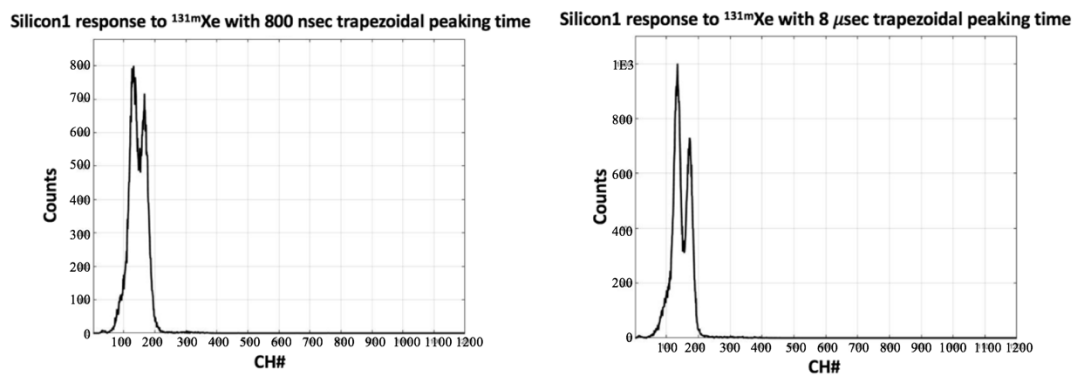


Figure 4-10 and

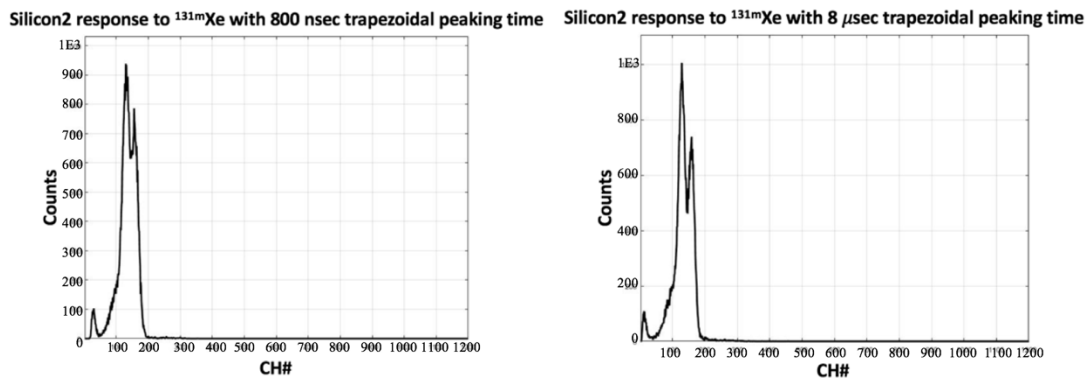


Figure 4-11 shows the difference in peak separation between the 129 keV and the 160 keV conversion electrons when the trapezoidal peaking time is changed from 800 ns to 8 μ s keeping the flat top time constant.

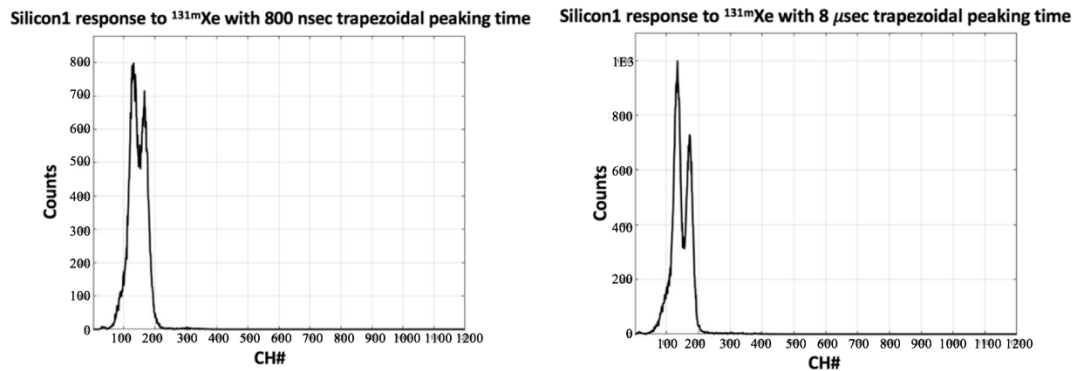


Figure 4-10: Silicon1 response to ^{131m}Xe with an 800 ns trapezoidal peaking time (left) and 8 μ s trapezoidal peaking time (right) and a 1.2 μ s flat top time in both spectra

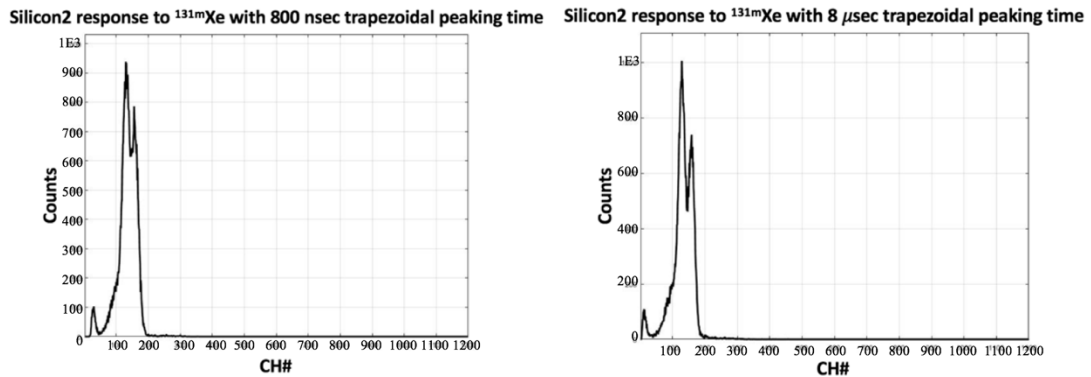


Figure 4-11 Silicon2 response to ^{131m}Xe with an 800 ns trapezoidal peaking time (left) and 8 μ s trapezoidal peaking time (right) and a 1.2 μ s flat top time in both spectra

Unlike CZT detectors, there is no gain adjustment for the silicon detectors because they don't have the electron trapping problems associated with compound semiconductors. The system is now ready for radioxenon measurements. The first step was to take free running spectra for all four detectors to check the response when the system is fully operating with all four detectors biased and running. Coincidence spectra will be taken next to compare them to the simulation results produced by MCNP.

4.1.3 CZT and Silicon Spectra in Oscilloscope Free Running Mode using $^{131\text{m}}\text{Xe}$

This section presents the first spectra generated in free running mode from $^{131\text{m}}\text{Xe}$.

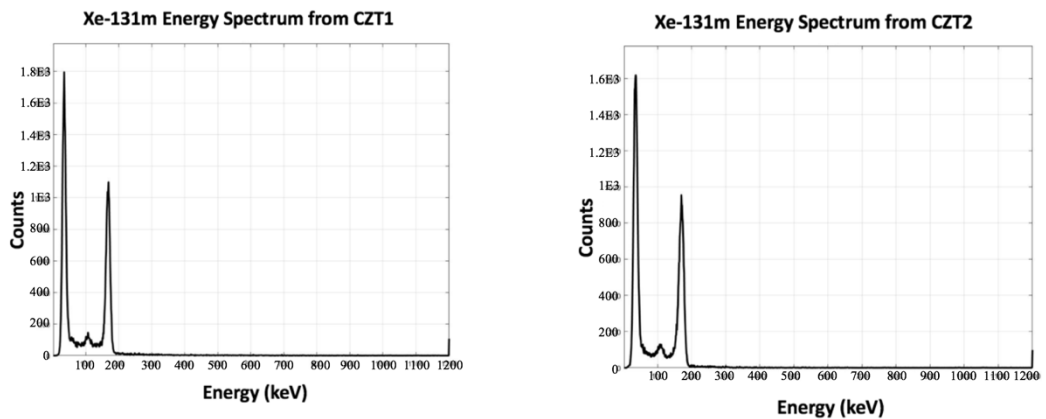


Figure 4-12 shows the spectra generated from CZT 1 and CZT 2. The two peaks are from the 30 keV X-ray and the 164 keV gamma ray. The small peak between the 30 keV and 164 keV is from the Compton edge of the 164 keV gamma. The resolution of keV and 164 keV is from the Compton edge of the 164 keV gamma. The resolution of

the 30 keV peak is 34.28% for CZT1 and 37.83% for CZT2, where the resolution of the 164 keV peak is 8.28% for CZT1 and 10.00% for CZT2. Each spectrum was generated by collecting 100,000 gross counts from ^{131m}Xe .

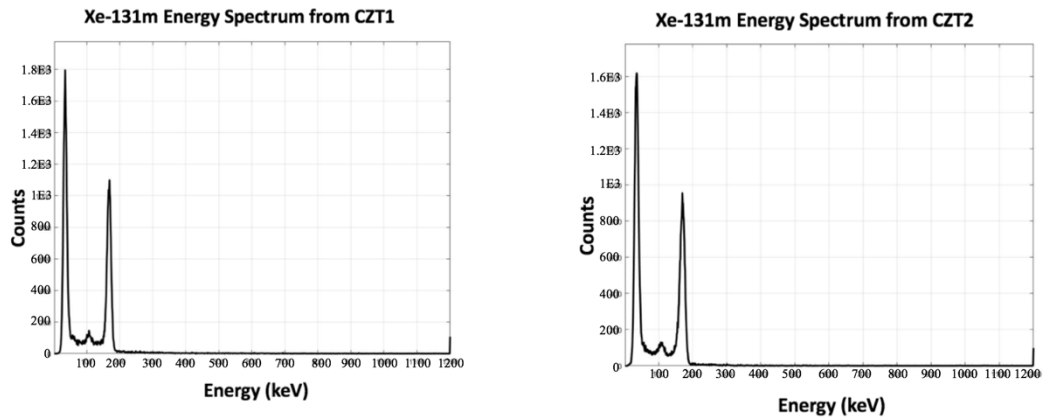


Figure 4-12: ^{131m}Xe gamma/X-ray spectra generated by the CZT detectors in free running mode

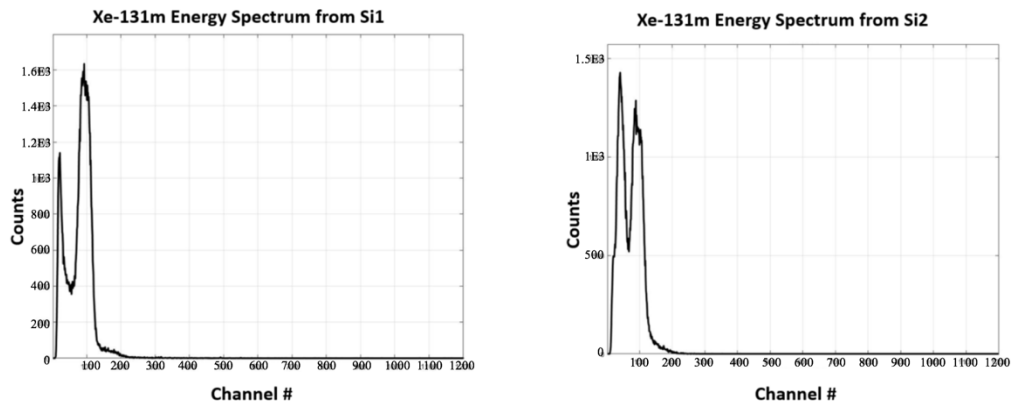


Figure 4-13 shows the first attempt to generate beta/conversion electron spectra from ^{131m}Xe . The figure shows two peaks, the first is due to electrical noise and the

second one is generated from both the 129 keV and the 159-163 keV conversion electrons. The biasing voltage applied to the silicon detectors when collecting these spectra was -130 V, which proved not enough to get healthy spectra.

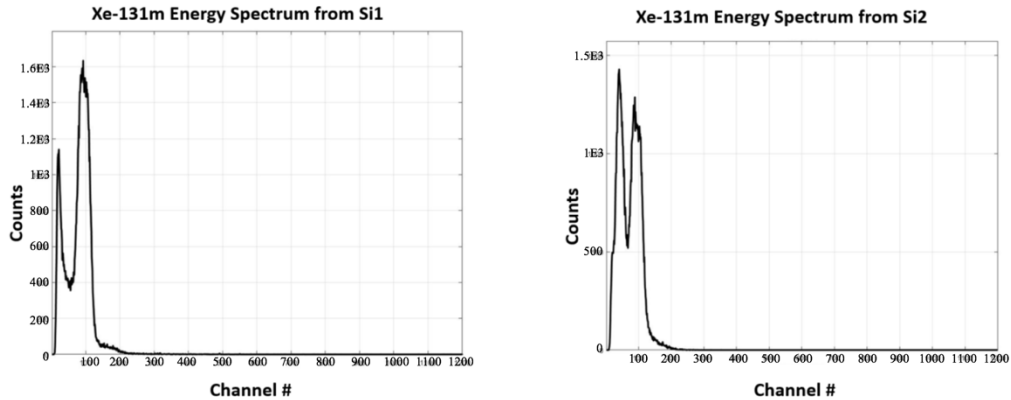


Figure 4-13: ^{131m}Xe Beta/conversion electron spectra generated by the silicon detectors in free running mode

The biasing voltage was increased to -145 and the amplification circuit described above was added to the output of the silicon preamplifiers to eliminate oscillation and increase the signal to noise ration of the detectors. Figure 4-14 shows the enhanced spectra from both silicon detectors. The noise level was decreased so much that we can see a small peak at the lower end of the spectrum as result of the 24 keV auger electrons and the 30 keV X-rays. The second peak is for the 129 keV conversion electron and the one right next to it is from the 159-163 keV conversion electrons. The resolution of the 129 keV is 16.66% for silicon1 and 16.87% for silicon2.

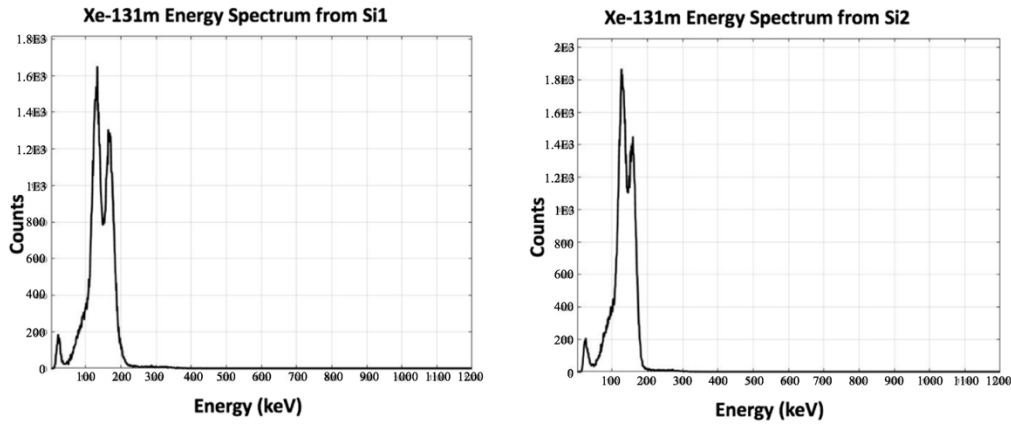


Figure 4-14: Enhanced ^{131m}Xe Beta/conversion electron spectra generated by the silicon detectors in free running mode

4.1.4 Coincidence Detection Window

The coincidence detection window is a timing window that indicates if two radiation quanta were emitted from radioxenon in coincidence. A timer is enabled in the coincidence module any time one of the four detectors is triggered. The timer counts for a particular amount of time set by the user in MATLAB and waits for another trigger to arrive during that time window. For this detection system, if a CZT trigger enables the counter, the system will wait for one of the two silicon detectors to be triggered during the time window. If a silicon detector enables the counter, the system will wait for one of the two CZT detectors to be triggered during the time window. The amount of time to count for depends on the electrical and physical properties of the detectors used in the system. The electron drift time should be calculated for both silicon and CZT. Drift time is a function of the electron mobility, voltage, and the size of the detector as described in equation 4-3:

$$\tau_e = \frac{d}{v_e} = \frac{d}{\mu_e \cdot E} = \frac{d}{\mu_e \cdot (\frac{V}{d})} = \frac{d^2}{\mu_e \cdot V} \quad (4-3)$$

Where τ_e is the electron's drift time, d is the detector thickness, v_e is the electron's drift velocity, μ_e is the electron's mobility, E is the electric field inside the detectors, which is proportional to the detector bias voltage, V is the bias voltage. The thickness of the CZT is 10 mm and 0.5 mm for the silicon. Mobility is 1350 cm²/V.s for CZT and 1450 cm²/V.s for silicon. Finally, the cathode voltage for the CZT is -1000 V, and -145 V for silicon. Using equation 4-3, the electron drift time is **740 ns** in CZT in the CZT detectors and for electrons inside the CZT detectors and **1189 ns** in silicon. As a result, electrons will drift through silicon is one order of magnitude faster than in CZT. Thus, coincidence detection time will follow the electron drift time in CZT. Coincidence time window was also determined experimentally as shown in Figure 4-15 and Figure 4-16 using DPP8 and DPP2 respectively. The measurement for DPP8 has bad statistics because it was 5 min coincidence measurements, where DPP2 coincidence measurements were taken for 10 min so the curve is smoother compared to the DPP8 curve as it doesn't flatten out at higher coincidence windows. The appropriate coincidence window is 1 μ s, a value very close to the theoretical 0.74 μ s calculated from equation 4-3. The count rate in Figure 4-16 clearly flattens out at 1 μ s so coincidence experiments conducted in this work will have a 1 μ sec coincidence timing window. Ranjbar et al. used the same size CZT crystals with an equal cathode voltage and got a coincidence time window of 1 μ s as well [66].

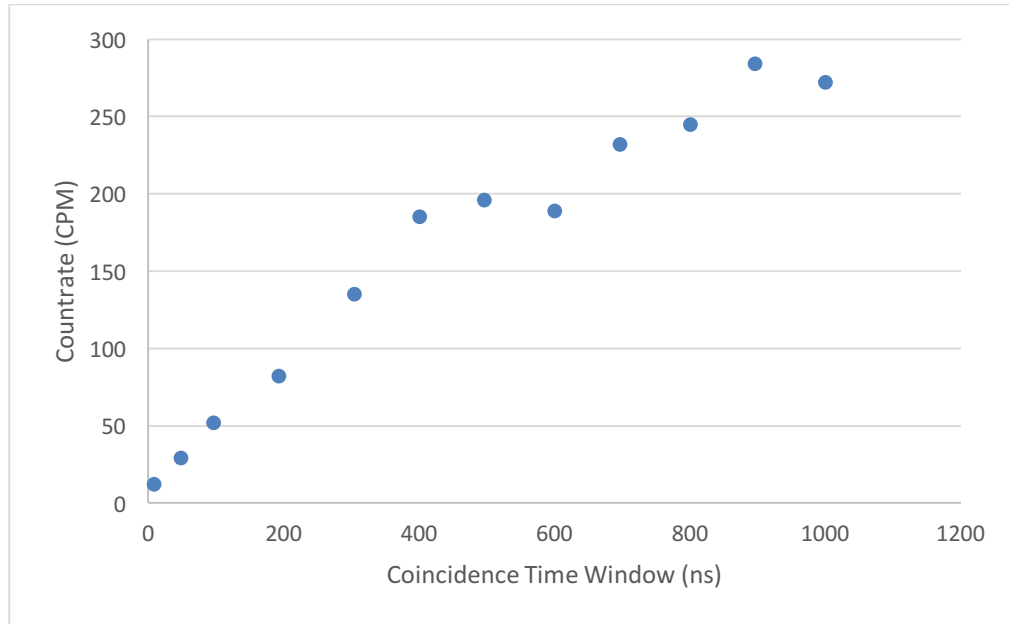


Figure 4-15: Coincidence window determination for a 1cm^3 cube coplanar CZT detector using a ^{60}Co source using DPP8

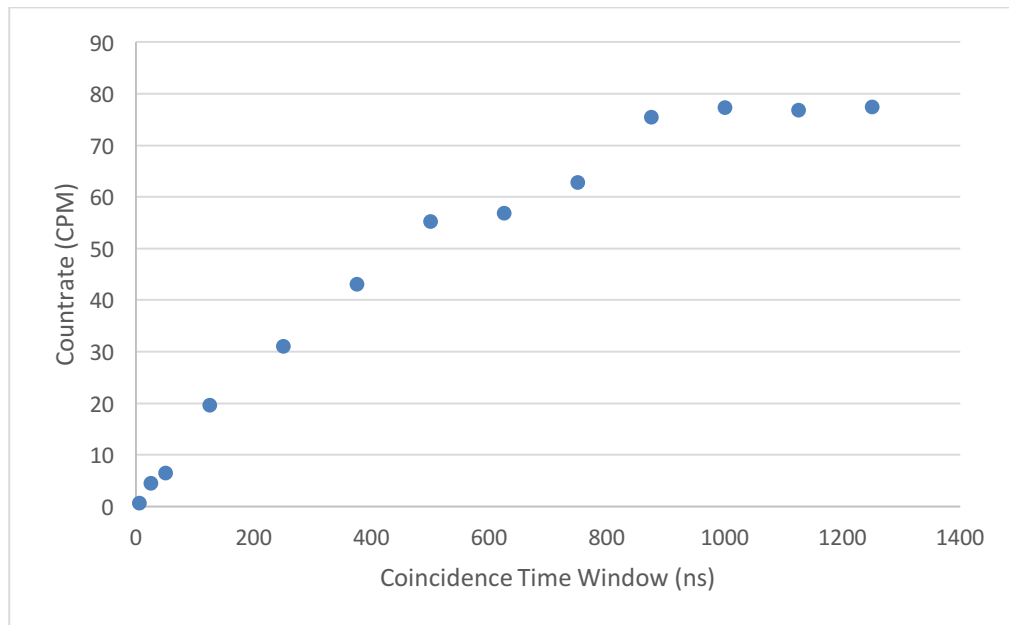


Figure 4-16: Coincidence window determination for a 1cm^3 cube coplanar CZT detector using a ^{60}Co source using DPP2

To test the coincidence module in the FPGA, two input channels of the DPP8 were connected to the same output of a signal generator with a 2-way BNC T-splitter. One of the channels was connected to a long coaxial cable to introduce a delay between both channels. The cable was about 420 feet in length. Each foot of a coaxial cable delays the signal by ~ 1.5 ns, so a total of 52.5 ns was introduced to one of the signals. When the coincidence window was set to a value below 52.5 ns, the system was not triggered, and when the window was set to values greater than 52.5 ns the system was triggered. This validated the proper functioning of the coincidence module.

4.2 Radioxenon Measurements using DPP8

These first radioxenon measurements were carried out to evaluate the response of DPP8 to all four radioxenons of interest. The measurements will also evaluate the performance of the coincidence module in detecting coincidence events. ^{131m}Xe , ^{133m}Xe , ^{133}Xe and ^{135}Xe were produced using enriched ^{130}Xe , ^{132}Xe and ^{134}Xe . The gases were activated in the OSU's TRIGA reactor. Equation 4-4 was used to calculate the estimated activity of all 3 ml gas samples:

$$A = \lambda N = N_T(\sigma_{th}\varphi_{th})(1 - e^{-\lambda t}) \quad (4-4)$$

Where N is the number of radioactive atoms, σ is the activation cross section (cm^2), N_T is the number of target atoms, φ is the thermal flux ($\text{n cm}^2 \text{ s}^{-1}$), t is the irradiation time (s), and λ is the decay constant of induced activity (s^{-1}). The irradiation time varied between samples (4 to 12 hours), and the thermal flux of the OSU TRIGA reactor is $2.51 \times 10^{11} \pm 3.26 \times 10^{10}$ neutrons/ $\text{cm}^2\text{-s}$. The resulting activity of the ^{131m}Xe sample was 6.0 μCi , 8.8E-2 μCi for ^{133}Xe , 2.0 μCi for ^{133m}Xe , and 5.9E-2 μCi for ^{135}Xe .

4.2.1 ^{135}Xe Experimental Results

An enriched sample of ^{134}Xe was activated in the OSU TRIGA reactor to generate ^{135}Xe .

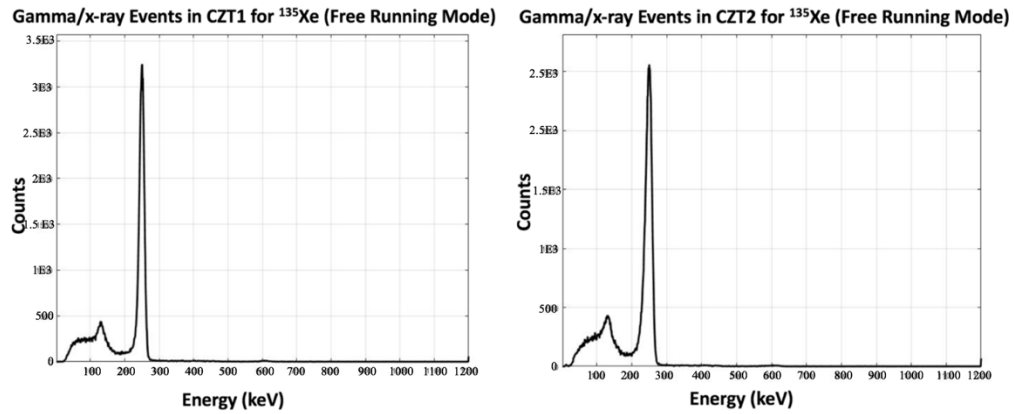


Figure 4-17 shows free running spectra generated from CZT1 and CZT2. The energy resolution of the 250 keV peak from CZT1 was 6.40% and the energy resolution from CZT2 was measured at 8.40%.

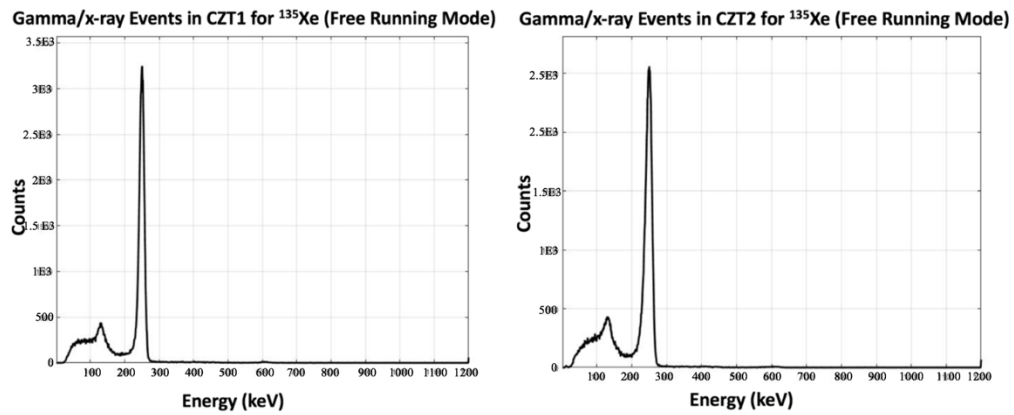


Figure 4-17: Gamma spectra from CZT1 (left) and CZT2 (right) generated by ^{135}Xe in free running mode

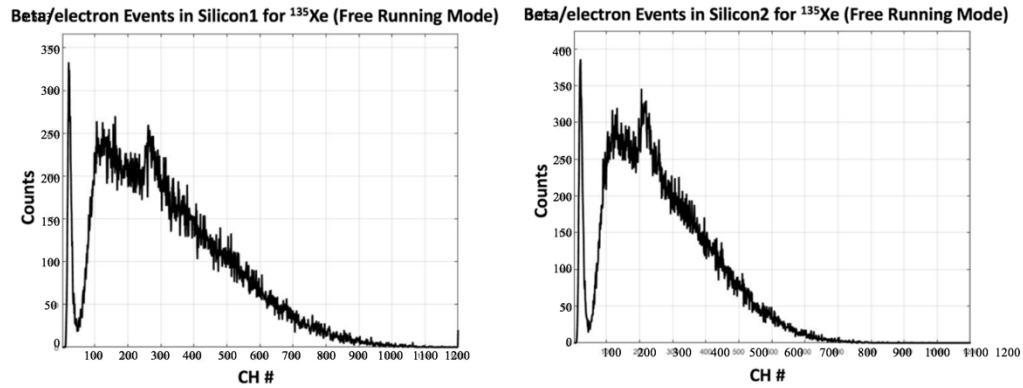


Figure 4-18 shows the spectra from silicon1 and silicon2 in free running mode. The spectra show the beta continuum extending up to the maximum energy of 910 keV emitted by ^{135}Xe . There is a peak riding on the beta spectrum from the 214 keV conversion electron. The low energy peak is due to electrical noise.

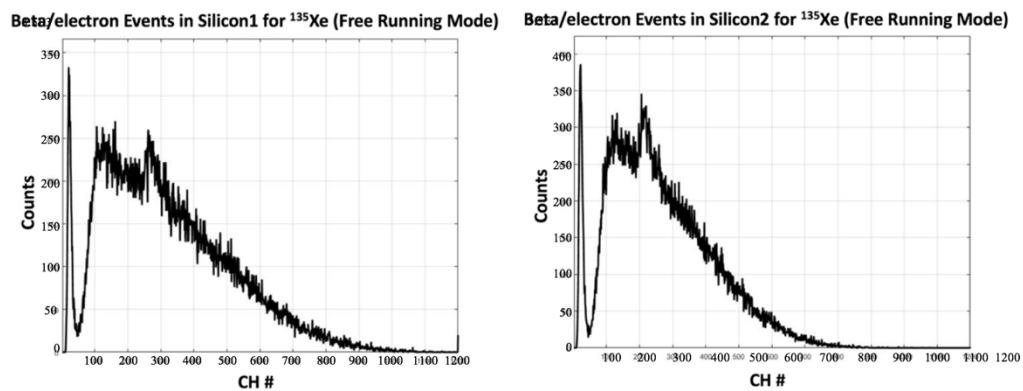


Figure 4-18: Beta spectra from silicon1 (left) and silicon2 (right) generated by ^{135}Xe in free running mode

A 2-D coincidence spectrum of ^{135}Xe is shown in Figure 4-19. On the 2-D spectrum, the horizontal axis represents the energy absorbed in the PIPSBox silicon detectors, and the vertical axis represents the energy absorbed in the coplanar CZT detectors.

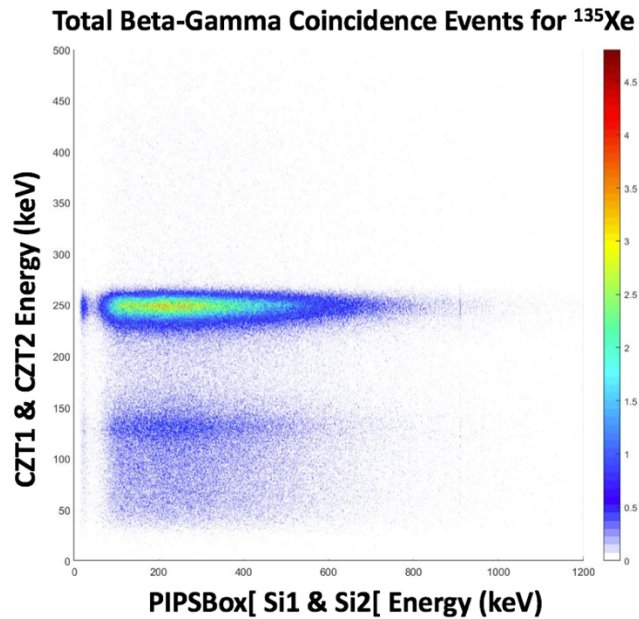


Figure 4-19: 2-D coincidence events from ^{135}Xe generated by the PIPSBox/CZT detection system

Events are populated around the 250 keV horizontal energy line representing photons absorbed energy in the CZT detectors. These events extend up to the 910 keV maximum energy of the beta particle emitted by ^{135}Xe . Another populated region can be seen around the 120-130 keV CZT energy line. These events are due to the

Compton edge of the 250 keV gamma in coincidence with the 910 keV beta particle.

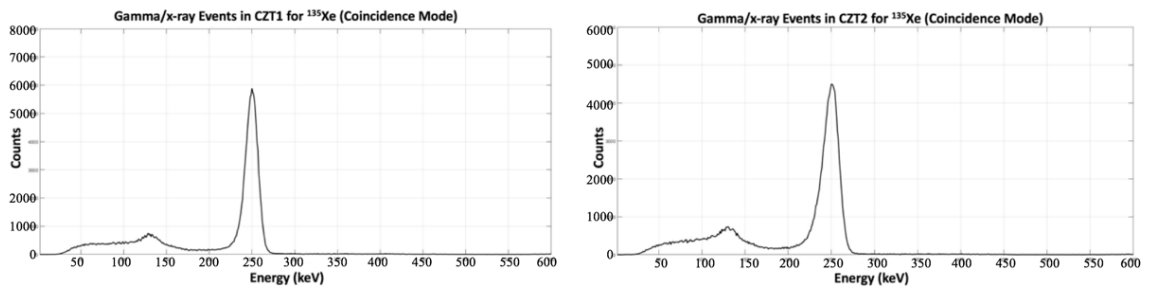


Figure 4-20 shows the gated gamma events absorbed in CZT1 and CZT2 with a prominent peak from the 250 keV gamma ray. Gated gamma events are those in coincidence with events in the silicon detectors.

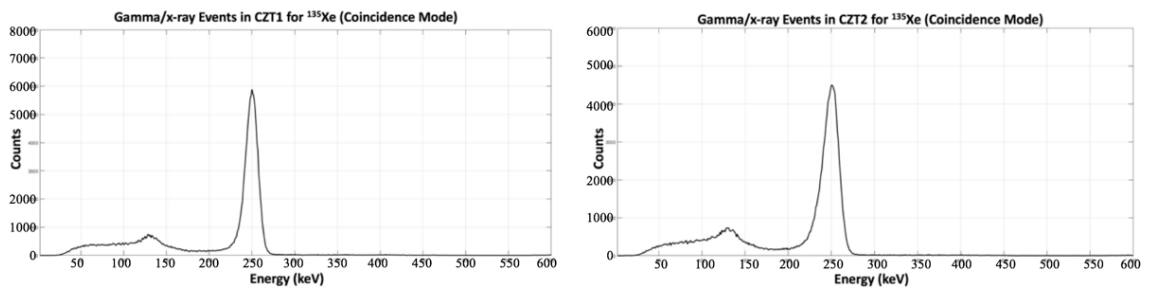


Figure 4-20: Gamma events from CZT1 (left) and CZT2 (right) generated by ^{135}Xe in coincidence mode

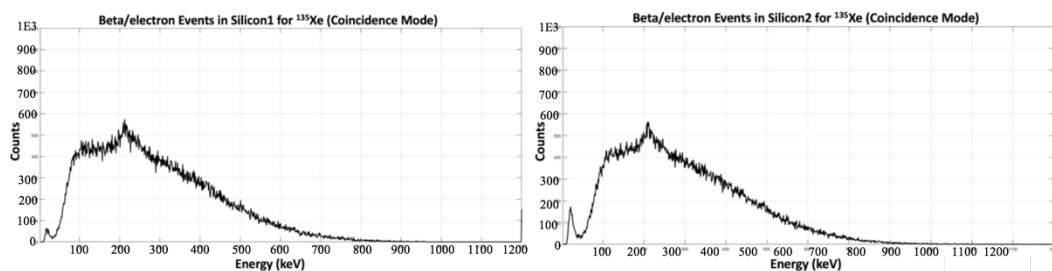


Figure 4-21 shows the gated beta events absorbed in silicon1 and silicon2. The beta spectra show the 214 keV conversion electron, which is emitted in coincidence with a 31 keV X-ray. This conversion electron should not be seen in the coincidence spectrum. The coincidence module mischaracterized them as true coincidences. This issue will be investigated more using DPP2.

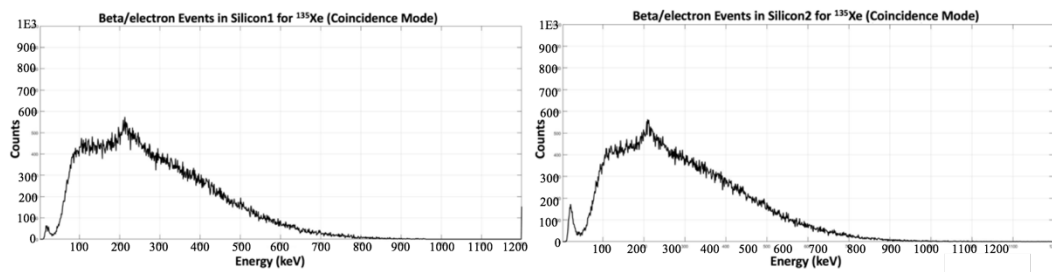


Figure 4-21: Beta events from silicon1 (left) and silicon2 (right) generated by ¹³⁵Xe in coincidence mode

Figure 4-22 shows total gated gamma events in both CZT1 and CZT2. The spectrum shows what we expect from a coincidence spectrum generated by ¹³⁵Xe.

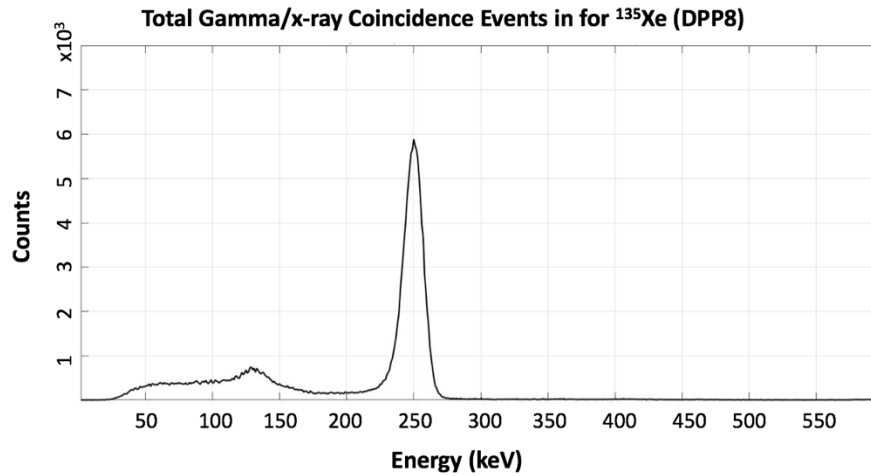


Figure 4-22: Total gamma events from CZT1 and CZT2 generated by ^{135}Xe in coincidence mode

Figure 4-23 shows total gated beta events in both silicon1 and silicon2 with the 214 keV conversion electron peak riding on the beta spectrum. This peak should not develop in a coincidence beta spectrum from ^{135}Xe .

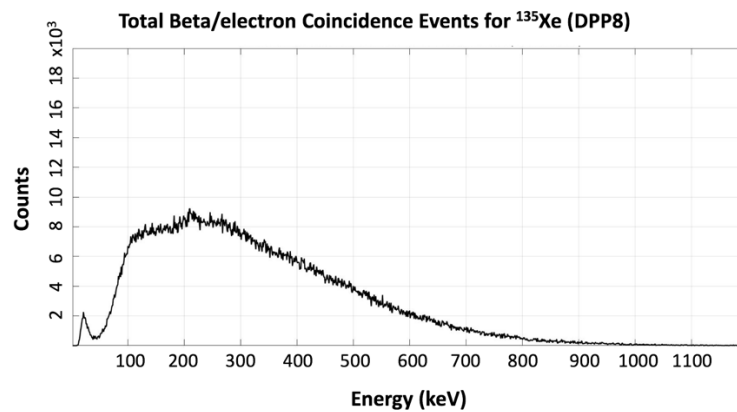


Figure 4-23: Total gamma events from silicon1 and silicon2 generated by ^{135}Xe in coincidence mode

4.2.2 ^{133}Xe & $^{133\text{m}}\text{Xe}$ Experimental Results

A sample of ^{132}Xe was activated in the OSU TRIGA reactor to generate ^{133}Xe and $^{133\text{m}}\text{Xe}$.

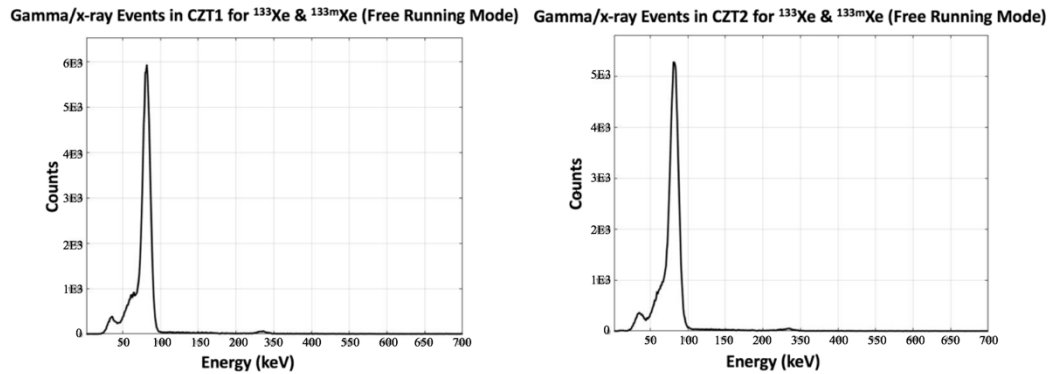


Figure 4-24 shows free running spectra generated from CZT1 and CZT2. The energy resolution of the 81 keV peak from CZT1 was 15.85% and the energy resolution from CZT2 was measured at 17.28%. The 30 keV peak is not as prominent as it should be because the threshold value was set high enough that most of the 30 keV X-rays can't pass the threshold value. The yield of the 30 keV X-ray is higher than the yield of the 81 keV gamma ray.

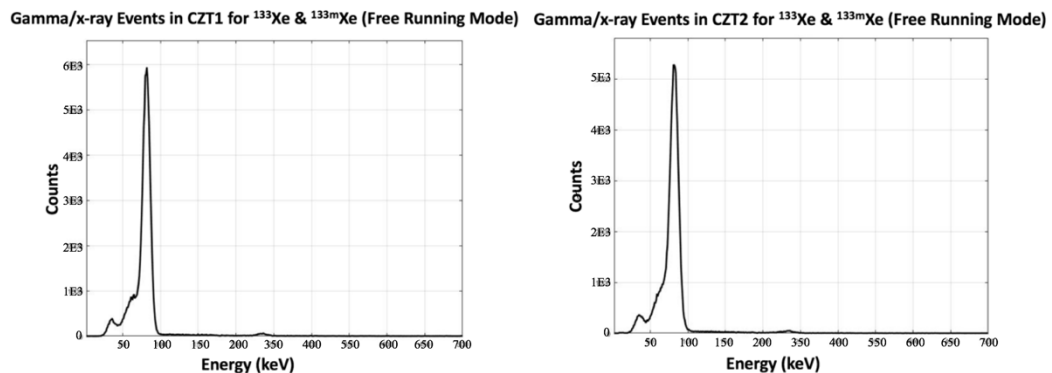


Figure 4-24: Gamma spectra from CZT1 (left) and CZT2 (right) generated by ^{133}Xe and $^{133\text{m}}\text{Xe}$ in free running mode

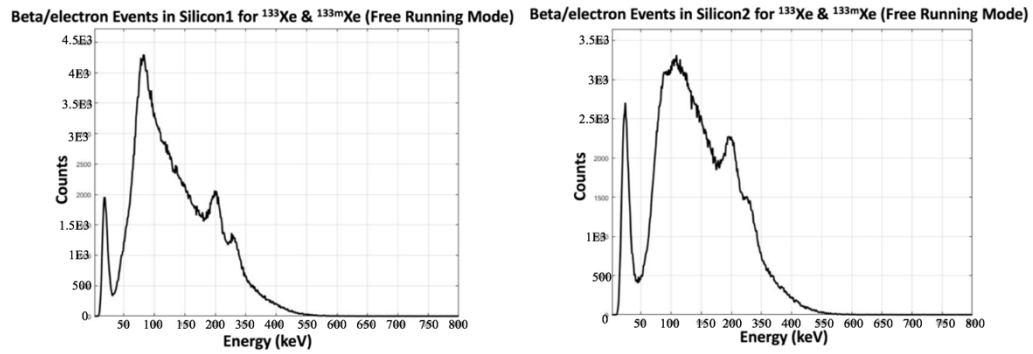


Figure 4-25 shows the spectra from silicon1 and silicon2 in free running mode. The spectra show the beta continuum extending up to the maximum energy plus the 45 keV conversion electron, which adds up to ~ 400 keV. The spectra show the 45 keV conversion electron at the low end of the spectrum, the 199 keV from $^{133\text{m}}\text{Xe}$ on top of the beta continuum and the 227 keV from $^{133\text{m}}\text{Xe}$ conversion electron riding the beta continuum.

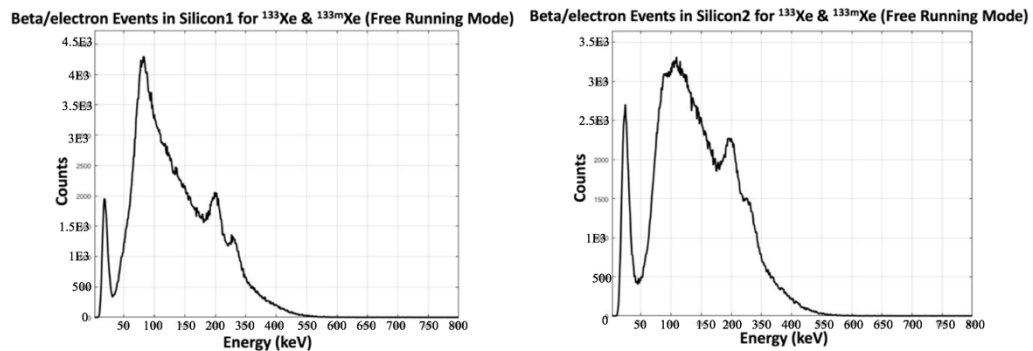


Figure 4-25: Beta spectra from silicon1 (left) and silicon2 (right) generated by ^{133}Xe and $^{133\text{m}}\text{Xe}$ in free running mode

The 2-D coincidence spectrum of ^{133}Xe and $^{133\text{m}}\text{Xe}$ is shown in Figure 4-26. On the 2-D spectrum, the horizontal axis represents the energy absorbed in the PIPSBox silicon detectors, and the vertical axis represents the energy absorbed in the coplanar CZT detectors. Events are populated around the 81 keV energy line representing the photons absorbed energy in the CZT detectors. These events extend up to the 400 keV maximum energy of the beta particle summed with the 45 keV conversion electron emitted by ^{133}Xe .

Total Beta-Gamma Coincidence Events for ^{133}Xe & $^{133\text{m}}\text{Xe}$ (Double Coincidence)

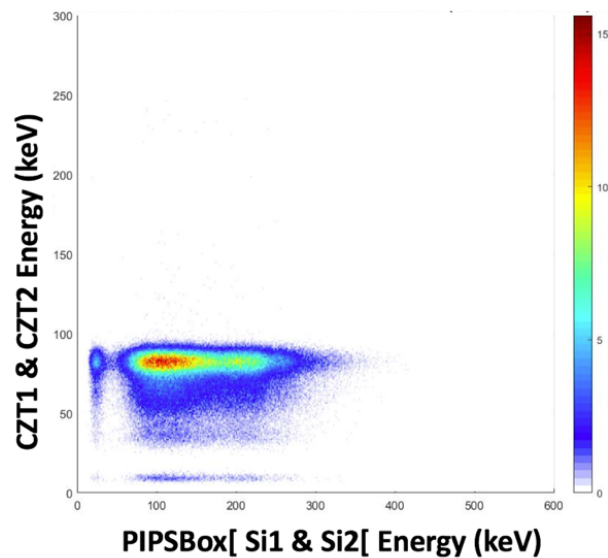


Figure 4-26: 2-D coincidence events from ^{133}Xe and $^{133\text{m}}\text{Xe}$ generated by the PIPSBox/CZT detection system

It was expected to have another populated region around the 30 keV energy for $^{133\text{m}}\text{Xe}$ coincidence events between the 30 keV X-ray and the 199 keV conversion electron. It is believed that these events cannot be seen because of the coincidence module is missing them. Since the 199 keV conversion electron is in coincidence with

30 keV X-rays, there is no populated region also around the 199 keV silicon energy since most of the X-rays are rejected. The low energy peak on

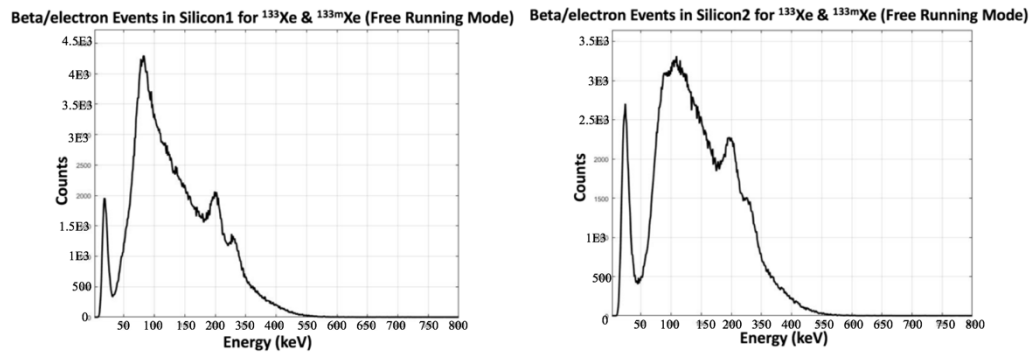


Figure 4-25 is combination of the 45 keV conversion electron and some of the 30 keV X-rays.

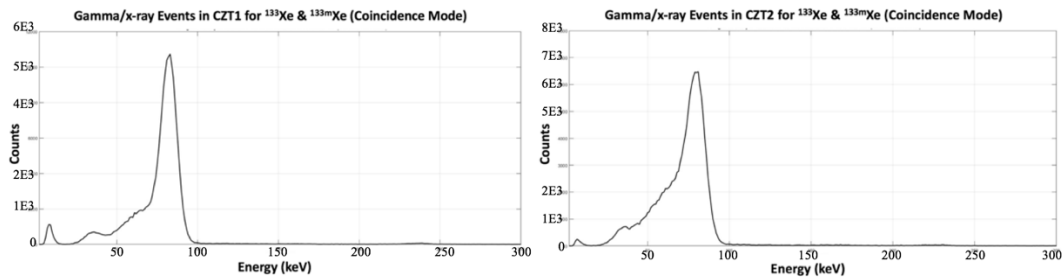


Figure 4-27 shows the gated gamma events absorbed in CZT1 and CZT2. The 30 keV peak is not on the spectrum which indicates that the coincidence module is missing events between the 30 keV X-ray and the 199 keV conversion electron. The low energy peak is due to electrical noise.

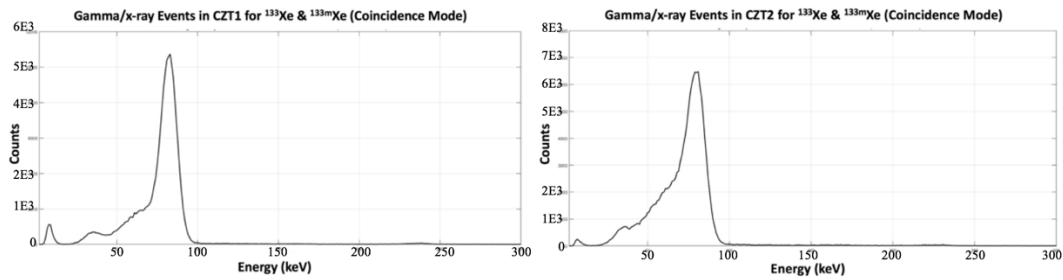


Figure 4-27: Gamma events from CZT1 (left) and CZT2 (right) generated by ^{133}Xe and $^{133\text{m}}\text{Xe}$ in coincidence mode

Figure 4-28 shows the gated beta events absorbed in silicon1 and silicon2. On the spectra, the 199 keV conversion electron can be seen on the beta continuum. This peak suggest that the coincidence module might not be working as expected since most of the 30 keV X-rays are rejected and the 199 keV is not in coincidence with the 81 keV gamma. Therefore, DPP2 will be used to investigate this problem in the coincidence module and generate the expected spectra from this radioxenon.

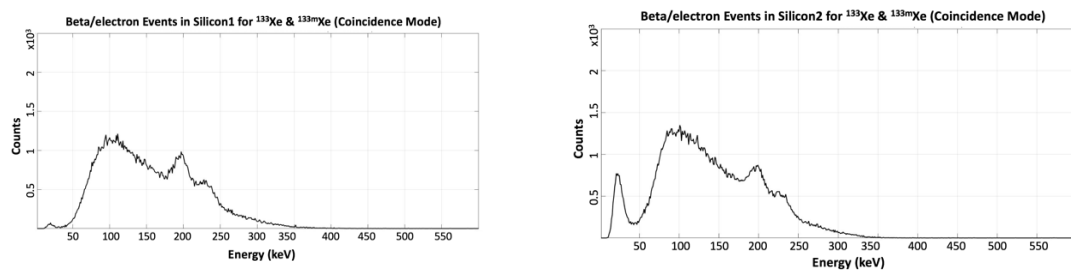


Figure 4-28: Beta events from silicon1 (left) and silicon2 (right) generated by ^{133}Xe and $^{133\text{m}}\text{Xe}$ in coincidence mode

Figure 4-29 shows total gated gamma events in CZT1 and CZT2. The 30 keV peak is not on the spectrum which suggests that the coincidence module did not identify events between the 30 keV X-ray and the 199 keV conversion electron.

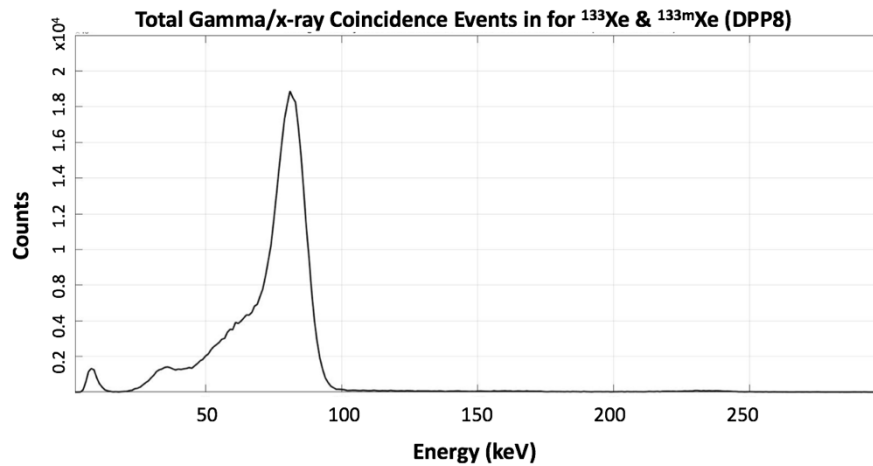


Figure 4-29: Total gamma events from CZT1 and CZT2 generated by ^{133}Xe and $^{133\text{m}}\text{Xe}$ in coincidence mode

Figure 4-30 shows total gated beta events in silicon1 and silicon2. Again, the spectrum does not show a well-defined 199 keV peak from the conversion electron which suggest that the coincidence module is not working well. This issue will be investigated using DPP2.

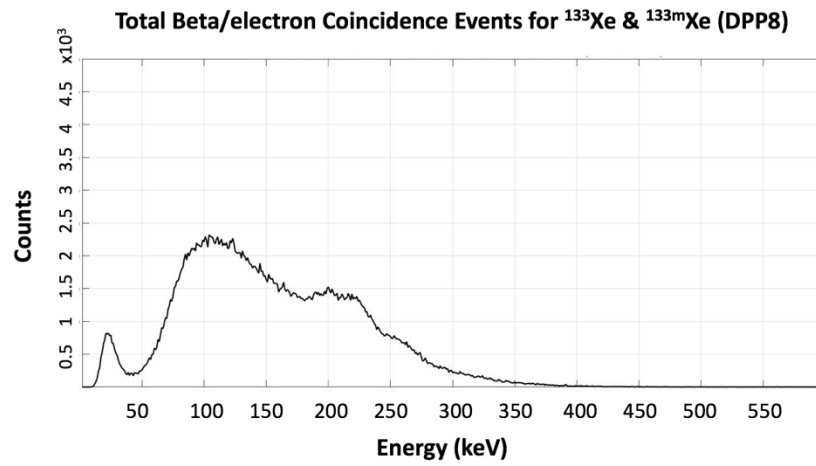


Figure 4-30: Total beta events from silicon1 and silicon2 generated by ^{133}Xe and $^{133\text{m}}\text{Xe}$ in coincidence mode

Another measurement was performed to generate a 2-D coincidence plot but with triple coincidence, that is between two silicon detectors and one of the CZTs. Figure 4-31 shows the triple coincidence 2-D spectrum.

Total Beta-Gamma Coincidence Events for ^{133}Xe & $^{133\text{m}}\text{Xe}$ (Triple Coincidence)

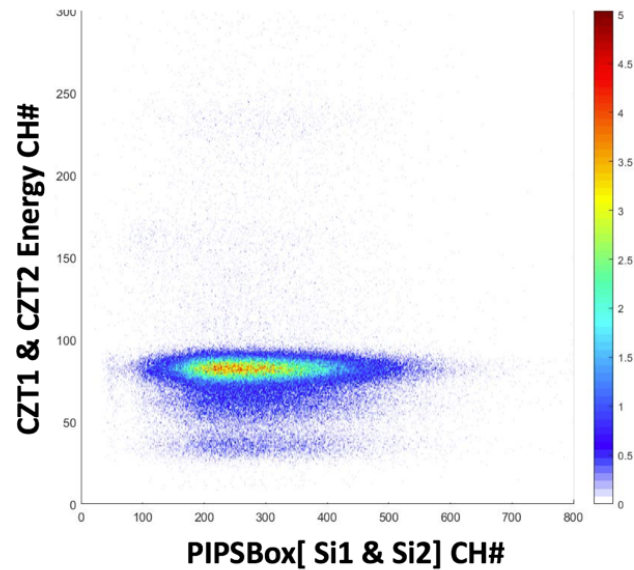


Figure 4-31: 2-D triple coincidence events from ^{133}Xe and $^{133\text{m}}\text{Xe}$ generated by the PIPSBBox/CZT detection system

The figure shows events populated around the 81 keV energy line and the 30 keV energy line but extend to the maximum beta energy summed with the 45 keV conversion electron. Again, the 199 keV conversion electron cannot be seen here due to the high threshold set during the measurement setup, and that there is a problem with the coincidence module in detecting coincidence events between the 30 keV X-ray and the 199 keV conversion electrons.

4.2.3 ^{131m}Xe Experimental Results

A sample of ^{130}Xe was activated in the OSU TRIGA reactor to generate ^{131m}Xe . Figure 4-32 shows the spectra generated from CZT1 and CZT2 in free running mode. The energy resolution of the 30 keV X-ray is 34.28% in CZT1 and 37.83% in CZT2. The resolution of the 164 keV gamma was 8.28% from CZT1 and 10.00% from CZT2.

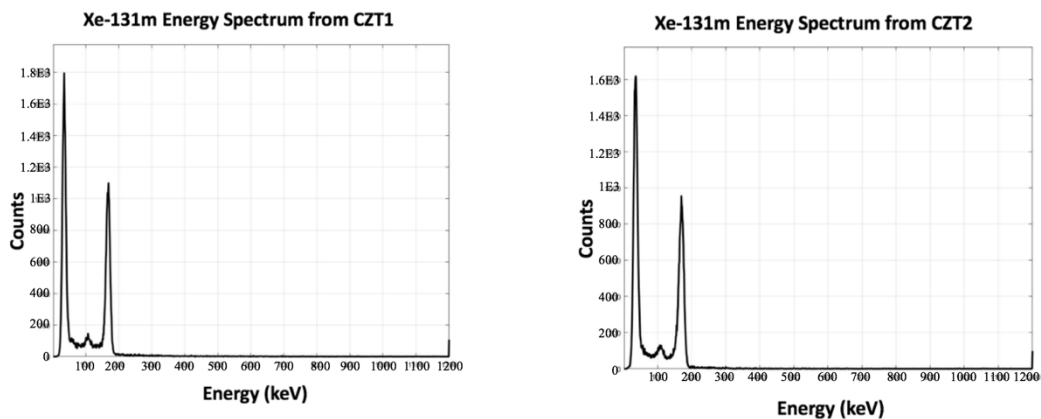


Figure 4-32: Gamma spectra from CZT1 (left) and CZT2 (right) generated by ^{131m}Xe in free running mode

Figure 4-33 shows the ^{131m}Xe spectra from silicon1 and silicon2 in free running mode. The 129 keV peak has a 16.66% resolution in silicon1 and 16.87% resolution in silicon2. The 160 keV peak has 14.21% resolution in silicon1 and 15.15% resolution in silicon2. It should be noted that the resolution of the 160 keV is approximated because the leading edge of the peak is merged with the falling edge of the 129 keV peak.

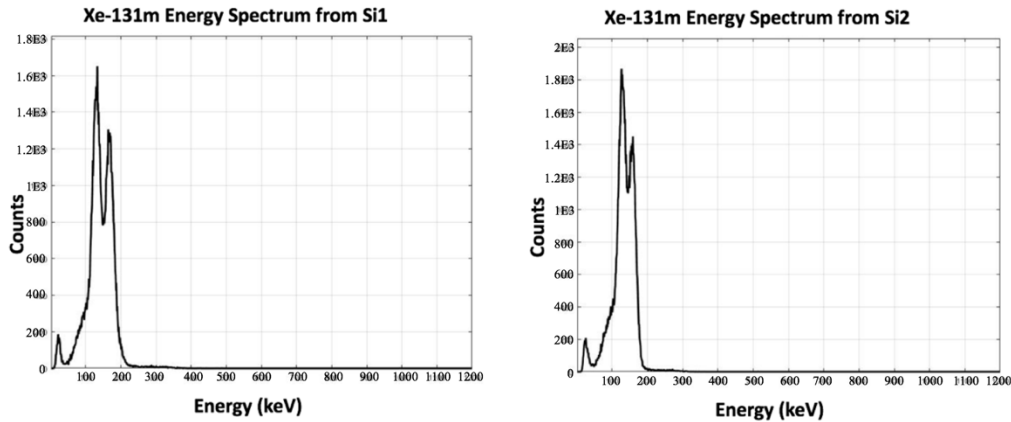


Figure 4-33: Beta spectra from silicon1 (left) and silicon2 (right) generated by ^{131m}Xe in free running mode

Figure 4-34 shows the 2-D coincidence spectrum of ^{131m}Xe . The spectrum shows two populated regions around the 30 keV X-ray energy line as discussed earlier, one from the 129 keV conversion electron and the other one is believed to be from mischaracterized coincidences between the 30 keV X-ray and:

1. the 160 keV conversion electrons,
2. a summation of the 30 keV X-ray with the 129 keV conversion electron
3. a summation of the 29 keV auger electron with the 129 keV conversion electron

The same populated regions are also found along the 164 keV gamma energy line. These events are also accidental since the ^{131m}Xe atom either decays by emitting the 164 keV gamma ray or the 129 keV X-ray in coincidence with the 30 keV X-ray.

Another possibility for the additional peak is that the coincidence module is not working properly and the system is being triggered by the 160 keV conversion electrons. These electrons are not in coincidence with the 30 keV X-rays.

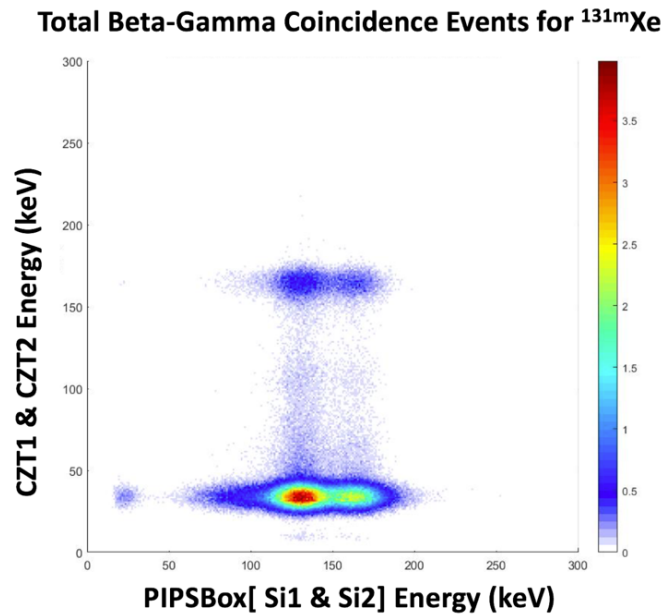


Figure 4-34: 2-D coincidence events from ^{131m}Xe generated by the PIPSBox/CZT detection system

Figure 4-35 shows the gated gamma events in CZT1 and CZT2 from ^{131m}Xe . The spectra show a 163 keV gamma ray that should not be among coincidence events.

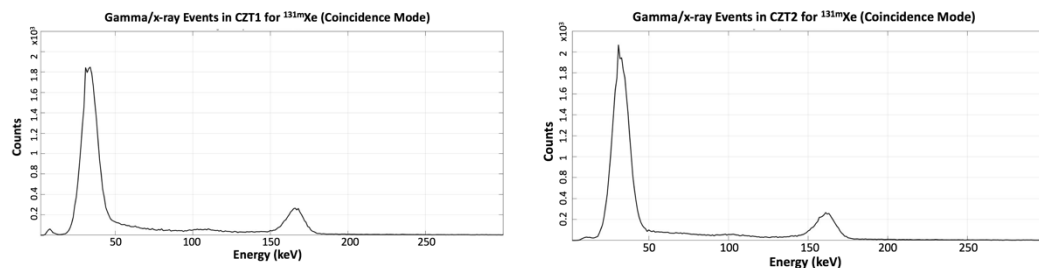


Figure 4-35: Gamma events from CZT1 (left) and CZT2 (right) generated by ^{131m}Xe in coincidence mode

Figure 4-36 shows gated beta events collected in silicon1 and silicon2. The additional peak can be seen after the 129 keV peak and it is from mischaracterized coincidence events.

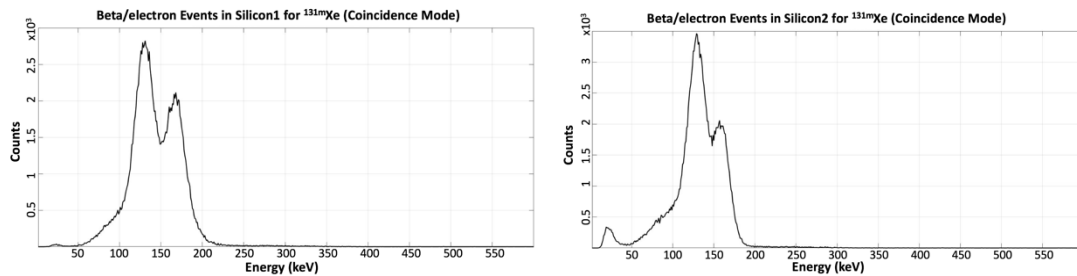


Figure 4-36: Beta events from Silicon1 (left) and Silicon2 (right) generated by ^{131m}Xe in coincidence mode

Figure 4-37 shows total gated gamma events in CZT1 and CZT2. The spectrum show the 163 keV which should not be detected in coincidence mode. The gamma ray is not in coincidence with any other radiation so there must be a problem with the coincidence module in DPP8.

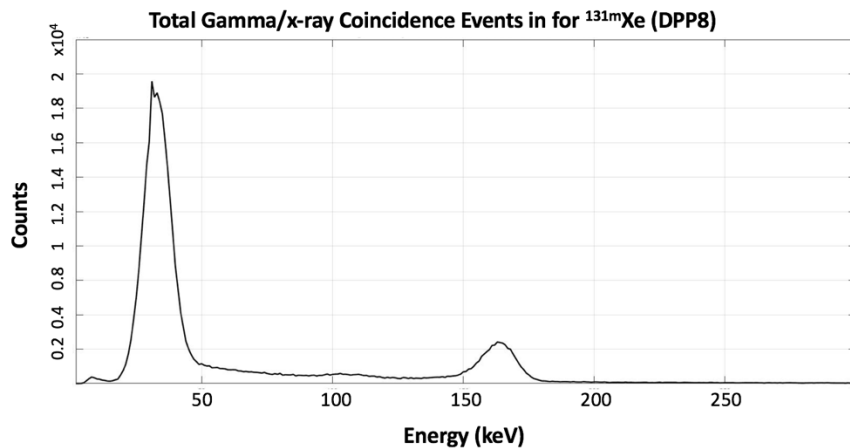


Figure 4-37: Total gamma events from CZT1 and CZT2 generated ^{131m}Xe in coincidence mode

Figure 4-38 shows total gated beta events in silicon1 and silicon2. The spectrum show two peaks. Xenon 131m beta spectrum should only have the 129 keV conversion electron peak. The 160 peak are events misscharacterized by the coincidence module that will be investigated using DPP2.

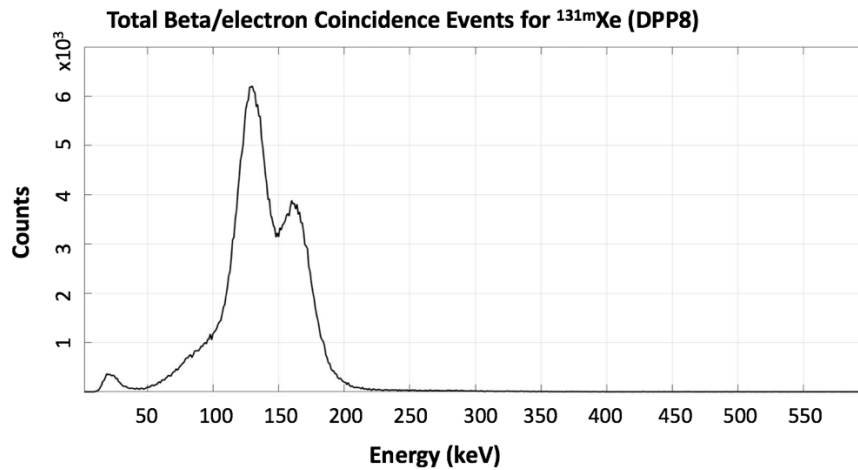


Figure 4-38: Total beta events from CZT1 and CZT2 generated ^{131m}Xe in coincidence mode

4.3 Energy Resolution Using DPP8

Table 4-1 lists the energy resolution of the X-ray and gamma radiation emitted by all four radioxenons from the PIPSBox/CZT detection system compared to other radioxenon systems developed at OSU and other systems deployed in IMS stations.

Table 4-1: Energy resolution of photons in the PIPSBox/CZT detection system using DPP8

	Gamma Energy (keV)	This Work (CZT1)	This Work (CZT2)	CASP	TECZT	WASPD	ARSA	SAUNA
Energy Resolution	30 (^{131m}Xe , ^{133m}Xe)	34.28%	37.83%	33.40%	48.20%	47.70%	32.00%	23.00%
	81 (^{133}Xe)	15.85%	17.28%	12.40%	12.50%	27.60%	25.00%	13.00%
	164 (^{131m}Xe)	8.28%	10.00%	NA	NA	NA	NA	NA
	250 (^{135}Xe)	6.40%	8.40%	5.70%	4.40%	19.30%	9.60%	NA

The PIPSBox/CZT system has comparable and sometimes better energy resolution for most of the X-ray and gamma energies emitted by radioxenons using the coplanar CZT detectors. Table 4-2 shows the resolution of the conversion electrons emitted by the metastable radioxenons compared to current radioxenon detection systems.

Table 4-2: Energy resolution of conversion electrons in the PIPSBox/CZT detection system using DPP8

	Gamma Energy (keV)	This Work (Silicon1)	This Work (Silicon2)	CASP	TECZT	WASPD	ARSA	SAUNA
Energy Resolution	129 (^{131m}Xe)	16.66%	16.87%	23.0%	10.1%	38.5%	25-30%	23.25%
	199 (^{133m}Xe)	14.21%	15.15%	19.0%	NA	NA	NA	NA

4.4 Radioxenon Measurements Using DPP2.0

Since results obtained by DPP8 did not match the MCNP simulations, a decision was made to run the same experiments using DPP2.0. This processor has been tested multiple times and the coincidence module produced results for the TECZT and CASP system, and both detection have more than one publication in respected journals. The processor has a 200 MHz sampling frequency with a 12-bit ADC resolution. DPP2 can only handle two channels so two detectors, CZT1 and silicon1 will be connected to it during the new measurements. All four radioxenons ^{131m}Xe , ^{133m}Xe , ^{133}Xe and ^{135}Xe were produced again using enriched ^{130}Xe , ^{132}Xe and ^{134}Xe . The gases were activated in the OSU's TRIGA reactor. The irradiation time was 7 hours for all samples, and the thermal flux of the OSU TRIGA reactor is $2.51 \cdot 10^{11} \pm 3.26 \cdot 10^{10}$ neutrons/cm²-s. The resulting activity of the ^{131m}Xe sample was 3.0 μCi , 4.4E-2 μCi for ^{133}Xe , 1.0 μCi for ^{133m}Xe , and 2.9E-2 μCi for ^{135}Xe . The activity of these samples is half of the activity used in the case of DPP8 to reduce the probability of accidental coincidences that were observed with DPP8.

4.4.1 ^{135}Xe Experimental Results Using DPP2.0

An enriched sample of ^{134}Xe was activated in the OSU TRIGA reactor to generate ^{135}Xe . Figure 4-39 shows the free running gamma spectrum generated by CZT1. On the spectrum, there is the 250 keV peak, the Compton edge around 140 keV and a 30 keV peak from 30 keV X-rays. Xenon 135 emits a 30 keV X-ray but with a

very low intensity around 4% as it was shown in Table 2-2. The peak is a combination of the 30 keV emitted by ^{135}Xe and $^{131\text{m}}\text{Xe}$ sample that wasn't completely removed from an earlier measurement. The resolution of the 250 keV is 5.09% which is better than the result achieved by DPP8.

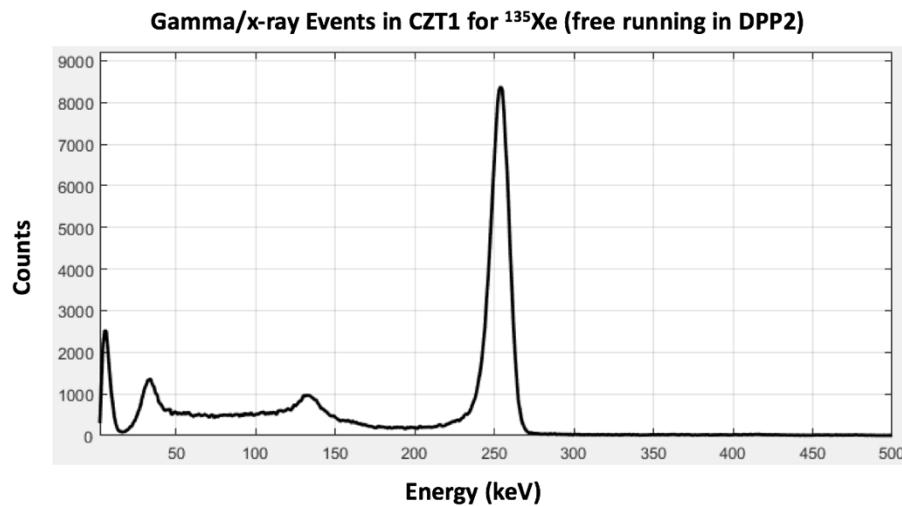


Figure 4-39: Gamma spectrum from CZT1 generated by ^{135}Xe in free running mode

Figure 4-40 shows the free running spectrum generated by silicon1. On this spectrum, the beta continuum extends to almost 900 keV and there is a 214 keV peak riding on the beta spectrum from a conversion electron that should be minimized or eliminated in the coincidence measurement since it is not in coincidence with the 250 keV gamma ray. The low energy peak is due to electrical noise.

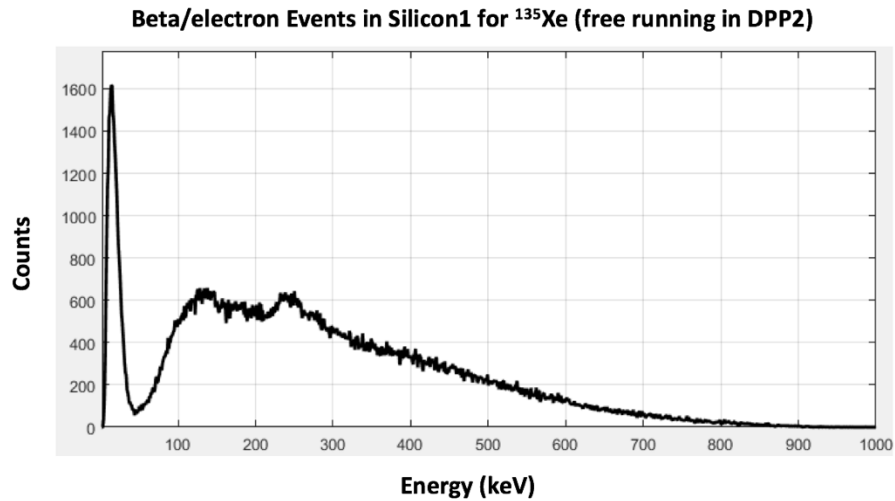


Figure 4-40: Beta spectra from silicon1 generated by ^{135}Xe in free running mode

Figure 4-41 shows the 2-D coincidence spectrum generated by silicon 1 and CZT1. The spectrum shows counts populated around the 250 keV X-ray energy from CZT1 that extends up to about 900 keV energy from silicon1. We can see events around the 140 keV energy due to the Compton edge of the 250 keV peak and events around the 30 keV line from the previous $^{131\text{m}}\text{Xe}$ sample that was not completely removed from the gas cell.

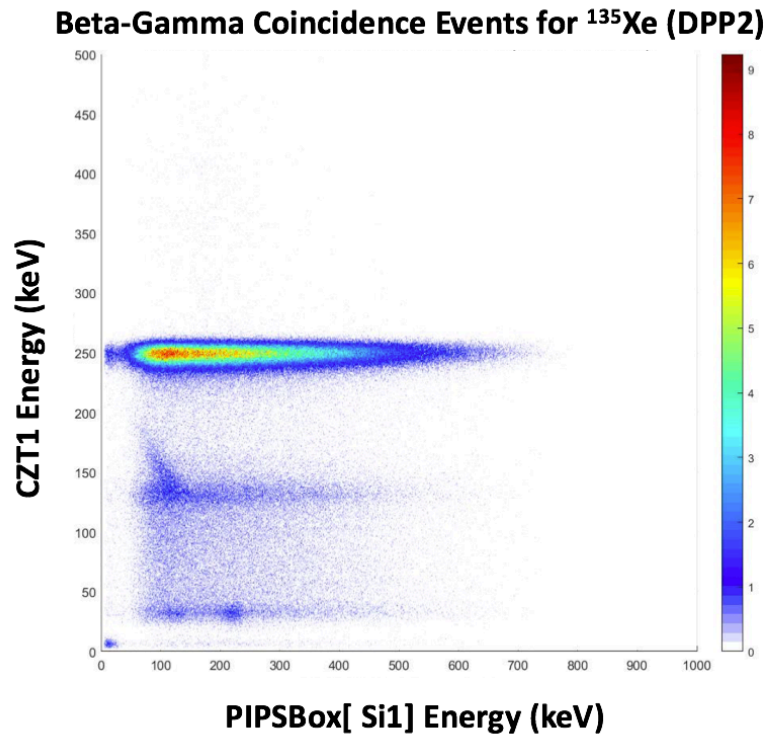


Figure 4-41: 2-D coincidence events from ^{135}Xe generated by the PIPSBox/CZT detection system using DPP2.0

Figure 4-42 shows gated gamma events from CZT1. The figure shows the 250 keV peak, its Compton edge around 140 keV and the 30 keV X-ray peak from the earlier sample. The 30 keV X-ray peak is due to the minimal memory effect observed in the PIPSBox. It is not as intense as it is for plastic scintillators.

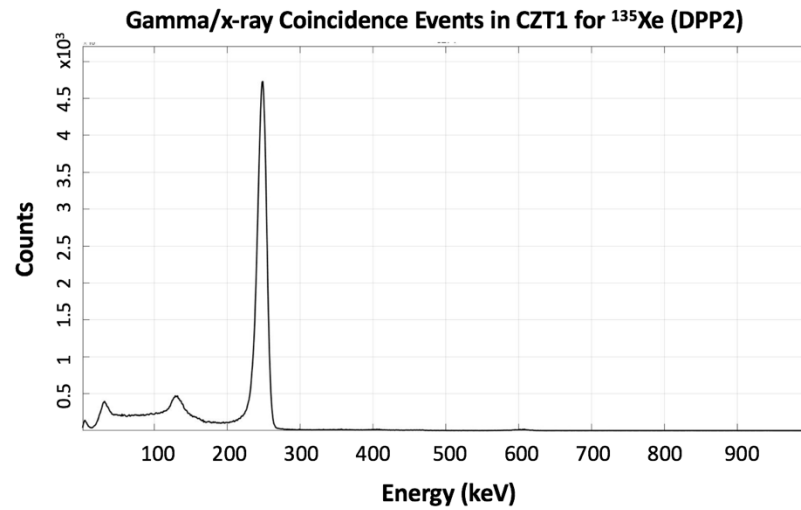


Figure 4-42 : Coincidence gamma spectrum from CZT1 generated by ^{135}Xe using DPP2

Figure 4-43 shows gated beta events in silicon1. The spectrum shows a beta continuum up to 900 keV. The 214 keV conversion electron peak is greatly minimized in this spectrum compared to the free running spectrum in Figure 4-40. The low energy peak is due to electrical noise.

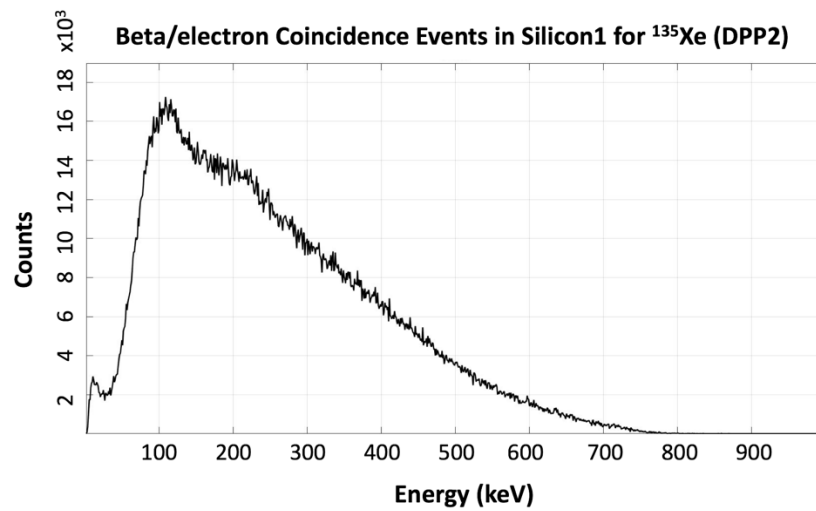


Figure 4-43: Coincidence beta spectrum from silicon1 generated by ^{135}Xe using DPP2

4.4.2 ^{133}Xe and $^{133\text{m}}\text{Xe}$ Experimental Results Using DPP2.0

An enriched sample of ^{132}Xe was activated in the OSU TRIGA reactor to generate ^{135}Xe . Figure 4-44 shows the free running gamma spectrum generated by CZT1. On the spectrum, there is the 30 keV X-ray peak and the 81 keV gamma ray peak. The counts under the 30 keV peak are less than the counts under the 81 keV peak even though 30 keV has higher intensity. This due to the threshold value. When the threshold was lowered to allow for more 30 keV counts, the spectrum was overwhelmed by electrical noise and the noise peak at the very low end of the spectrum had more counts than both the 30 and 81 keV peaks. This threshold value was a compromise between reducing the electrical noise peak and maximizing the 30 keV peak. The resolution of the 30 keV peak is 30.00%, and the resolution of the 81 keV peak is 12.19%. both resolutions are better than the ones obtained by DPP8.

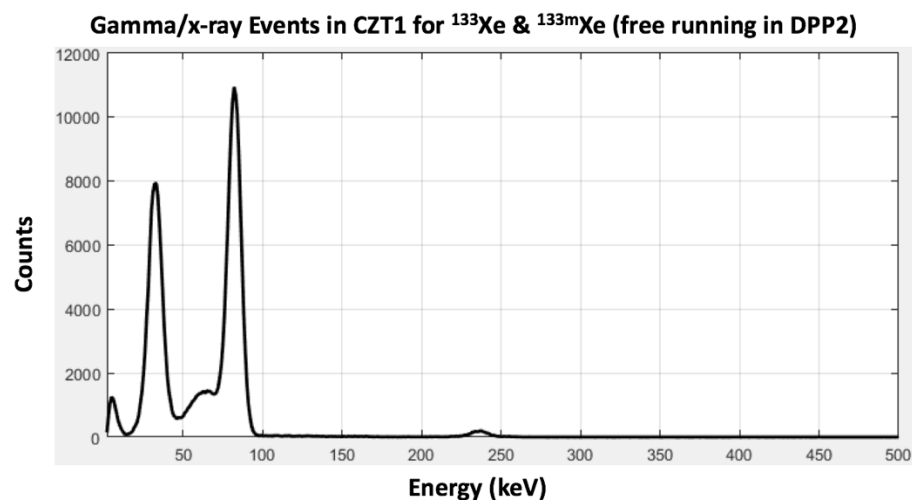


Figure 4-44: Gamma spectrum from CZT1 generated by ^{133}Xe and $^{133\text{m}}\text{Xe}$ in free running mode

Figure 4-45 shows the free running spectrum generated by silicon1. On this spectrum, the beta continuum extends to almost 400 keV which is the maximum beta energy in addition to the 45 keV conversion electron from ^{133}Xe . On the beta continuum, there are two peaks, the first one is from the 199 keV conversion electron and the second one is from the 227 keV conversion electron.

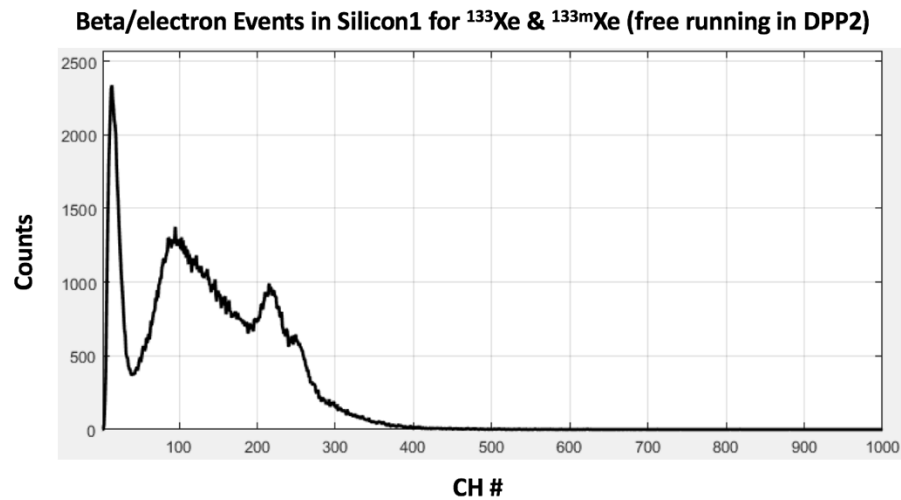


Figure 4-45: Beta spectrum from silicon1 generated by ^{133}Xe and $^{133\text{m}}\text{Xe}$ in free running mode

Figure 4-46 shows the 2-D coincidence spectrum generated by silicon 1 and CZT1. The spectrum shows counts populated around the 81 keV gamma ray line from ^{133}Xe and the 30 keV energy line from $^{133\text{m}}\text{Xe}$. On the 30 keV X-ray line, there is a cluster of events around the 199 keV silicon energy due to coincidence events between the 30 keV X-rays and the 199 keV conversion electrons. Intense events around the 81 keV line are due to the absorption of the average beta energy in silicon in coincidence with 81 keV gamma ray in the case of ^{133}Xe .

Beta-Gamma Coincidence Events for ^{133}Xe & $^{133\text{m}}\text{Xe}$ (DPP2)

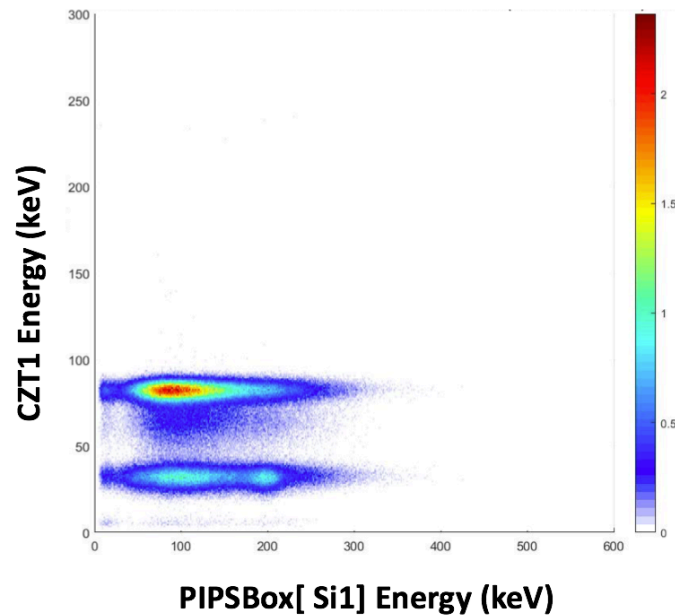


Figure 4-46: 2-D coincidence events from ^{133}Xe and $^{133\text{m}}\text{Xe}$ generated by the PIPSBox/CZT detection system using DPP2.0

Figure 4-49 shows gated gamma events from CZT1. The figure shows the 81 keV gamma ray peak and the 30 keV X-ray peak. There a little hump just before the 81 keV peak around 60 keV that is believed to be the result of the X-ray escape peak from Cd and Te. The peak at the very low end is due to electrical noise.

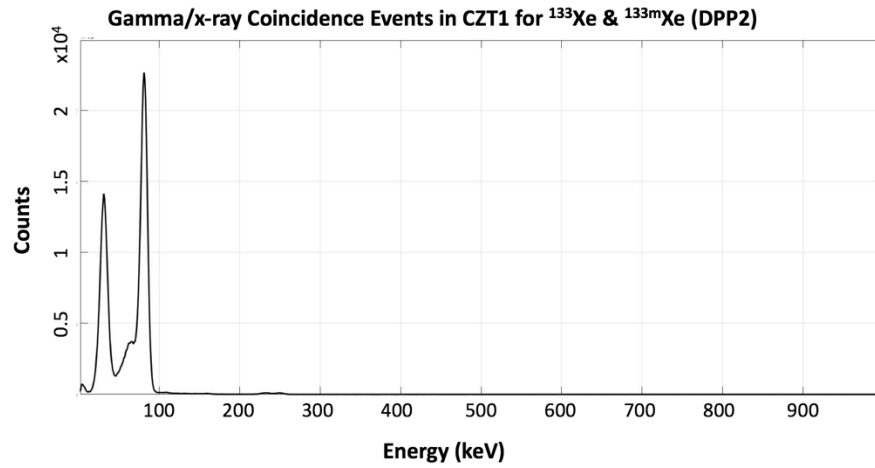


Figure 4-47: Coincidence gamma spectrum from CZT1 generated by ^{133}Xe and $^{133\text{m}}\text{Xe}$ using DPP2

Figure 4-48 shows gated beta events in silicon1. The spectrum shows a beta continuum up to 400 keV with a peak at 199 keV from the conversion electron emitted by $^{133\text{m}}\text{Xe}$. The peak at the very low end of the spectrum is due to electrical noise.

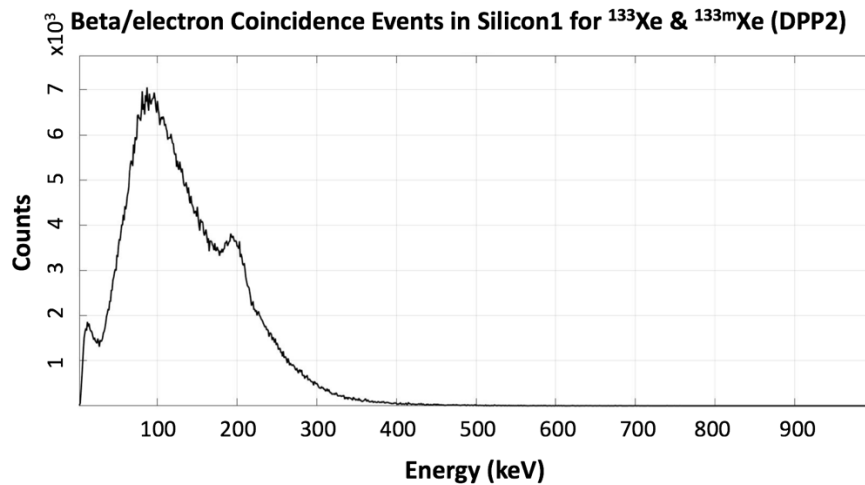


Figure 4-48: Coincidence beta spectrum from silicon1 generated by ^{133}Xe and $^{133\text{m}}\text{Xe}$ using DPP2

4.4.1 ^{131m}Xe Experimental Results Using DPP2.0

An enriched sample of ^{130}Xe was activated in the OSU TRIGA reactor to generate ^{131m}Xe . Figure 4-49 shows the free running gamma spectrum generated by CZT1. On the spectrum, there is the 30 keV X-ray peak, the 81 keV gamma ray peak, and the 164 keV gamma ray peak. The 81 keV peak is from an earlier ^{133}Xe and ^{133m}Xe sample that and it is due to the memory effect in the silicon detectors. This peak would have been more pronounced if a plastic scintillator was used as the gas cell and beta detectors. The time between gas evacuation and injection of the next sample was less than 6 hours. The resolution of the 30 keV peak is 30.00%. The peak at the very low end of the spectrum is due to electrical noise. Again, this resolution is better than the one obtained by DPP8.

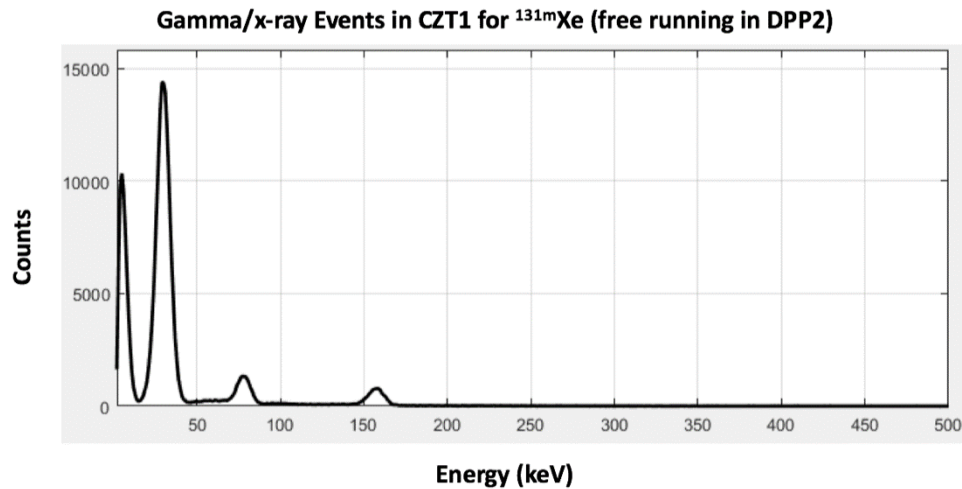


Figure 4-49: Gamma spectrum from CZT1 generated by ^{131m}Xe in free running mode

Figure 4-50 shows the free running spectrum generated by silicon1. On this spectrum, there are two peaks from the 129 keV and 159-160 keV conversion electrons. The peak at the low end of the spectrum is a mixture of electrical noise, 29 keV auger electrons and 30 keV X-rays absorbed in the silicon detector.

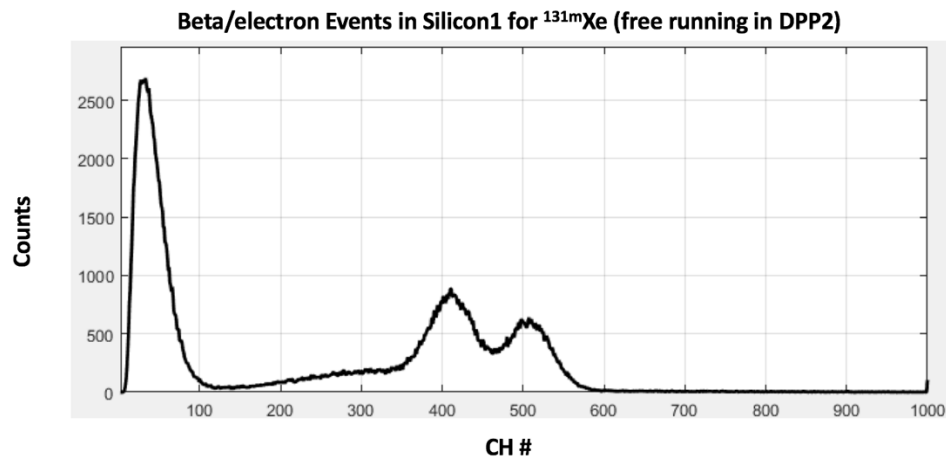


Figure 4-50: Beta spectrum from silicon1 generated by ^{131m}Xe in free running mode

Figure 4-51 shows the 2-D coincidence spectrum generated by silicon 1 and CZT1. The spectrum shows counts populated around the 30 keV X-ray energy from CZT1 that are concentrated around the 129 keV energy from silicon1. This is the expected signature of ^{131m}Xe . There is a tail to the events around the 129 keV energy due to back scattering events of electrons between silicon1 and silicon2. The faded events around the 81 keV line are due to previous sample of ^{133}Xe and ^{133m}Xe that was not completely removed from the PIPSBox gas cell. The events around the 10 keV energy

line are believed to be from escape peak of 30 keV. More measurements are needed to confirm that these events are from the 30 keV escape peak.

Beta-Gamma Coincidence Events for ^{131m}Xe (DPP2)

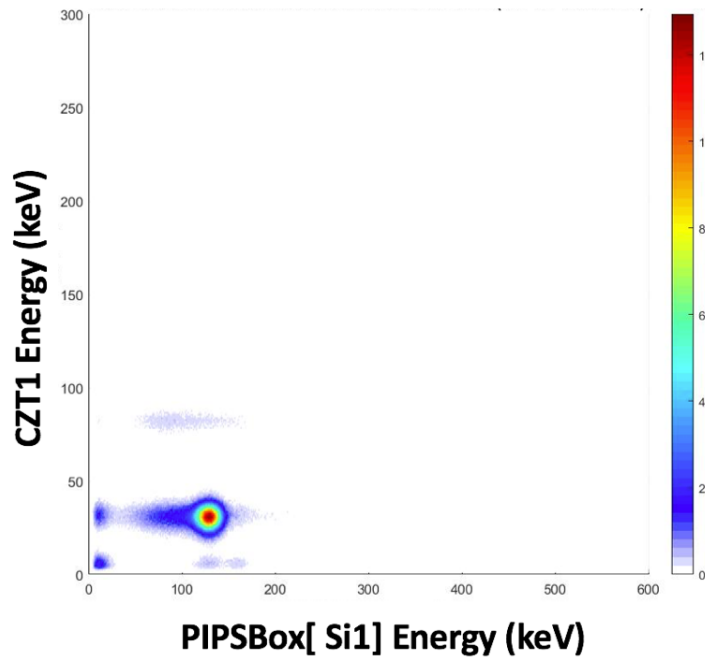


Figure 4-51: 2-D coincidence events from ^{131m}Xe generated by the PIPSBox/CZT detection system using DPP2.0

Figure 4-52 shows gamma coincidence events from CZT1. The figure shows the 30 keV X-ray peak in addition to the 164 keV gamma peak. There is also an 81 keV peak from the ^{133}Xe sample that was not fully evacuated from the gas cell.

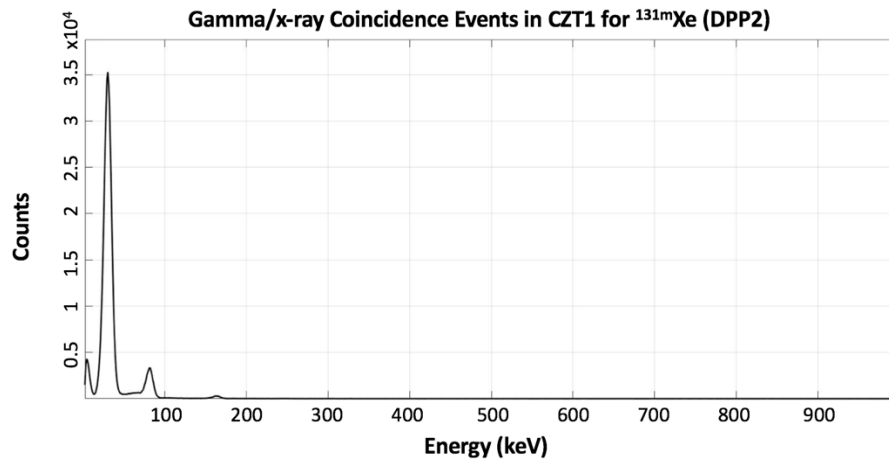


Figure 4-52: Coincidence gamma spectrum from CZT1 generated by ^{131m}Xe using DPP2

Figure 4-53 shows the beta coincidence events in silicon1. The spectrum shows a sharp peak for the 129 keV conversion electron in addition to a low energy peak from 30 keV X-rays and 29 keV Auger electrons and electrical noise. The resolution of the 129 keV peak is 17.05%, which is not better than the results obtained by DPP8 (16.66%)

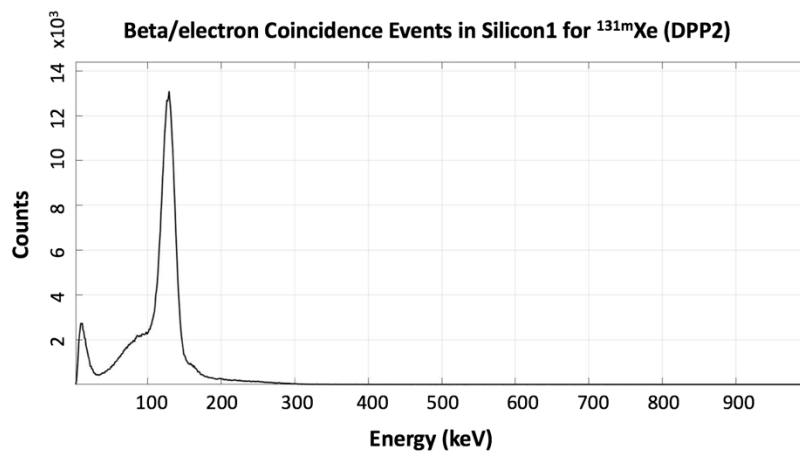


Figure 4-53: Coincidence beta spectrum from silicon1 generated by ^{131m}Xe using DPP2

4.5 Energy Resolution Using DPP2

Table 4-3 lists the energy resolution of the X-ray and gamma radiation emitted by all four radioxenons from the PIPSBox/CZT detection system compared to other radioxenon detection systems developed at OSU and other systems deployed in IMS stations.

Table 4-3: Energy resolution of CZT1 in the PIPSBox/CZT detection system using DPP2

	Gamma Energy (keV)	This Work (CZT1)	CASP	TECZT	WASPD	ARSA	SAUNA
Energy Resolution	30 (^{131m}Xe , ^{133m}Xe)	30.00%	33.40%	48.20%	47.70%	32.00%	23.00%
	81 (^{133}Xe)	12.19%	12.40%	12.50%	27.60%	25.00%	13.00%
	164 (^{131m}Xe)	NA	NA	NA	NA	NA	NA
	250 (^{135}Xe)	5.09%	5.70%	4.40%	19.30%	9.60%	NA

The previous table shows that the PIPSBox/CZT system has better energy resolution for most of the X-ray and gamma energies emitted by radioxenons. The silicon resolution is shown in Table 4-4 for DPP2. Again, the PIPSBox/CZT shows superior electron resolution when compared to current radioxenon detection systems.

Table 4-4: Energy resolution of Silicon1 in the PIPSBox/CZT detection system using DPP2

	Gamma Energy (keV)	This Work (Silicon1)	CASP	TECZT	WASPD	ARSA	SAUNA
Energy Resolution	129 (^{131m}Xe)	17.05%	23.0%	10.1%	38.5%	25-30%	23.25%
	199 (^{131m}Xe)	NA	19.0%	NA	NA	NA	NA

4.6 System Background

Figure 4-54 shows the background collected in 24 hours using DPP2.

Background Coincidence Events in 24 hours (DPP2)

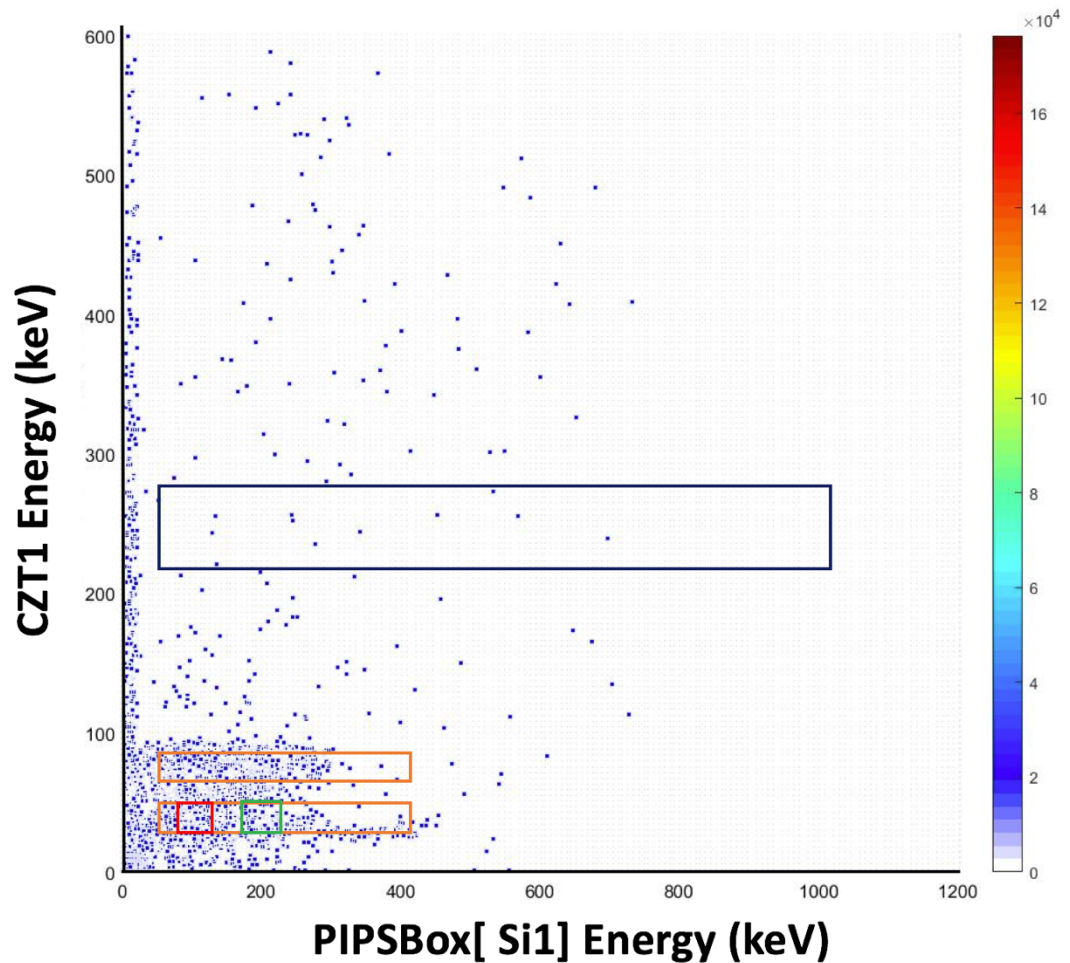


Figure 4-54: 2-D background spectrum generated from the PIPSBox/CZT detection system over 48 hours

The highlighted regions are the regions of interest, where background counts are integrated to calculate the MDC for each radionuclide. The small rectangular red region is for ^{131m}Xe , the small rectangular green region is for ^{133m}Xe , the two rectangular orange

regions are for ^{133}Xe , and finally the black rectangular region is for ^{135}Xe . These events are a result of the minimal memory effect inside the gas cell and electrical noise.

4.7 Minimum Detectable Concentration (MDC)

The MDC requirement for IMS detection systems is less than or equal to 1 mBq/m³ for ^{133}Xe [74]. In general, the MDC can be calculated using equation 4-5 described in PNNL work by McIntyre et al. [75]:

$$MDC \left(\frac{mBq}{m^3 air} \right) = \left[\frac{2.71 + 4.65\sigma_0}{\varepsilon_\beta \varepsilon_\gamma \beta_{BR} \gamma_{BR}} \right] \left[\frac{\lambda^2}{(1 - \exp(-\lambda T_c)) \exp(-\lambda T_p) (1 - \exp(-\lambda T_A))} \right] \left[\frac{T_C * 1000}{V_{air}} \right] \quad (4-5)$$

Where:

σ_0 : standard deviation of background counts in ROI

ε_β : β efficiency

ε_γ : γ efficiency

β_{BR} : β branching ratio

γ_{BR} : γ branching ratio

λ : radioxenon decay constant in inverse seconds (s⁻¹)

T_c : radioxenon collection time in seconds

T_p : Gas processing time in seconds

T_A : Count acquisition time in seconds

V_{air} : Sampled air volume which is equal to detector gas cell volume in (m³)

The background counts were obtained by running the CZT-PIPSBox detection system inside the aluminum box in a lead shielding for 24 hours. Then equation 4-6 was used to calculate the σ_0 in the MDC equation [75]:

$$\sigma_0 = \sqrt{BckCnt_{total} + \sigma_{BckCnt}^2 + InterferenceCnt + \sigma_{InterferenceCnt}^2 + MemoryCnt + \sigma_{MemoryCnt}^2} \quad (4-6)$$

The term for interference counts and memory counts can be eliminated because we assume no memory effect for the PIPSBox gas cell, and no interference counts from radon daughters since the measurement is performed in a controlled lab environment with pure xenon samples activated. These terms will have values once the detector is tested with real air samples at one of IMS stations. What we are left with is just the number of counts in the regions of interests for our radioxenons. The value of ϵ_β and ϵ_γ are obtained from Table 3-4, which was generated from the MCNP simulations. The next two variables β_{BR} and γ_{BR} are obtained from Table 2-2. For a direct comparison with previous detectors developed at OSU, the values of ($T_c = 8$ hours), ($T_p = 5.45$ hours), and ($T_A = 24$ hours) will be used. These values are the same values used in the ARSA MDC calculations [76]. Finally, V_{air} is typically 20 m^3 for IMS stations. The value will be adjusted according to the current detection system based on the ratios of gas cell values between PIPSBox and ARSA similar to what was done in Hennig et al. [77]. The ratio of gas cell volumes is ($10.6/6.14 = 1.726$), which will result in a scaled air volume of the ARSA system equal to ($V_{air} = 1.726 \times 3.26 = 5.626 \text{ m}^3$) for the CZT-

PIPSBox system. To calculate the background total count term in the σ_0 equation, we use equation 4-7 described in Hennig et al. work [77]:

$$BckCnt_{total} = [S_{Bck(ROI)}][CTW] \left[\frac{T_A}{T_B} \right] [N_{cp}] \quad (4-7)$$

Where:

$S_{Bck(ROI)}$ is Total background counts in the 2D spectrum ROI for each radioxenon, CTW is Coincidence time window (1 μ s), T_A is Acquisition time (24 hours), T_B is Background measurement time (48 hours), and N_{cp} is the Number of coincidence permutations (= 4) based on the method used by Hennig et al. [77].

All radioxenons will be calculated using the same MDC equation. Xenon-133 will have a special case because it has both an X-ray and a gamma ray that are on two different ROIs. Equation 4-8 shows the combined MDC calculation for ^{133}Xe which was described in PNNL work [75]:

$$^{133}\text{Xe}_{MDC} \left(\frac{mBq}{m^3 air} \right) = \sqrt{\frac{1}{(^{133}\text{Xe}_{MDC}^{31keV})^{-2} + (^{133}\text{Xe}_{MDC}^{81keV})^{-2}}} \quad (4-8)$$

Table 4-5 shows the calculated MDCs from the PIPSBox/CZT radioxenon detection system for a 1x1x1 cm³ coplanar CZT crystals. The system MDC values are excellent. All values are below the requirement of 1 mBq/m³.

Table 4-5: Calculated MDC values for the CZT-PIPSBox detection system (1x1x1 cm³ CZT)

Isotope	B- γ coincidence ROI	$\gamma_{BR} \cdot \beta_{BR}$	$\epsilon_{\beta} \cdot \epsilon_{\gamma}$ [MCNP]	MDC (mBq/m ³)
^{131m} Xe	31 keV X-rays and 129 keV CE	0.561	0.0459	0.25±0.016
^{133m} Xe	31 keV X-rays and 199 keV CE	0.584	0.0506	0.26±0.016
¹³³ Xe	81 keV gamma and 346 beta	0.372	0.0253	0.76±0.102
	31 keV gamma, 45 keV CE, and 346 beta	0.489	0.0318	0.46±0.094
¹³⁵ Xe	250 keV gamma and 910 keV beta	0.900	0.0411	0.72±0.045

Table 4-6 shows the calculated MDCs from the PIPSBox/CZT radionuclide detection system for a 3.46 x 3.46 x 1 cm³ coplanar CZT crystals (same area as the silicon detectors). The MDC values got one order of magnitude lower than the required IMS value. It should be mentioned that there is no commercially available coplanar CZT with the 3.46 x 3.46 x 1 cm³ size. Figure 4-55 shows the MDC of the CZT-PIPSBox compared to other OSU and IMS detection systems.

Table 4-6: Calculated MDC values for the CZT-PIPSBox detection system (3.46 x 3.46 x 1 cm³ CZT)

Isotope	B- γ coincidence ROI	$\gamma_{BR} \cdot \beta_{BR}$	$\epsilon_{\beta} \cdot \epsilon_{\gamma}$ [MCNP]	MDC (mBq/m ³)
^{131m} Xe	31 keV X-rays and 129 keV CE	0.561	0.2410	0.047±0.0020
^{133m} Xe	31 keV X-rays and 199 keV CE	0.584	0.2667	0.05±0.0020
¹³³ Xe	81 keV gamma and 346 beta	0.372	0.1322	0.14±0.0078
	31 keV gamma, 45 keV CE, and 346 beta	0.489	0.1684	0.08±0.0051
¹³⁵ Xe	250 keV gamma and 910 keV beta	0.900	0.2836	0.10±0.0027

We can see that the MDC gets better with bigger detection area for gamma and X-rays. The PIPSBox/CZT detection system meets the IMS MDC threshold for all four radioxenons, where all of them are below 1mBq/cm³ for both the 1x1x1cm³ and the 3.46x3.46x1 cm³ CZT detectors.

MDC Values for the PIPSBox/CZT System Compared to Current Radioxenons Detection Systems

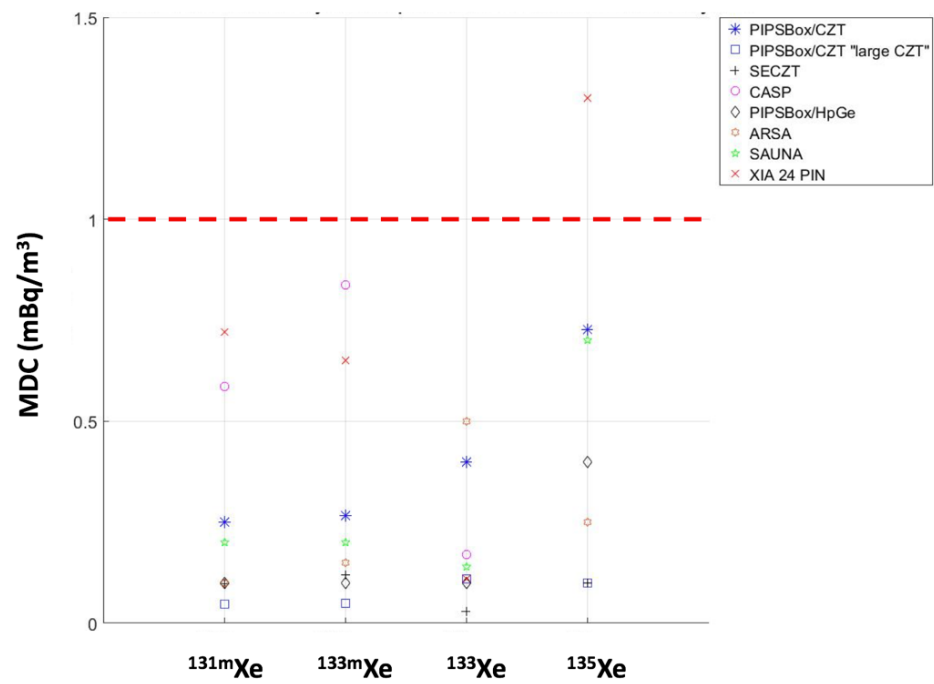


Figure 4-55: Comparison of MDC for the CZT-PIPSBox against current OSU and IMS detection systems

5. Conclusion

In conclusion, a new radioxenon detection system was built, assembled, and tested at OSU. The new detection system consisted of 4 semiconductor detectors. The gas cell of the detection system was made of two silicon detectors assembled in the new PIPSBox detection system made by Canberra. The PIPSBox was used as the beta and conversion electron detector. Two coplanar CZT detectors were coupled to the PIPSBox detector to measure X and gamma rays. The PIPSBox/CZT detection system had better resolution for all radiation emitted by all four radioxenons of interest compared to current detectors installed at IMS stations.

Two digital pulse processors, DPP2 and DPP8 were used to process the detection system coincidence events. DPP2 is a 200 MHz, 12-bit resolution digital processor that was used in previous radioxenon research at OSU. The new digital pulse processor DPP8 was developed to process coincidence events from all four semiconductor detectors. DPP8 had a 125 MHz sampling frequency with a 14-bit resolution ADC. A coincidence module firmware was implemented in a high-performance FPGA on DPP8 to identify and transfer coincidence events to the PC side via USB 3.0 technology. The detection system captured coincidence events in real-time and transferred them to a PC, where MATLAB performed the post processing.

The detection system should overcome current limitations in detectors installed at IMS stations such as memory effect since it is using semiconductor detectors, low air sampling frequency because memory effect is reduced, and low interference in

radioxenons ROI because of the excellent energy resolution observed from all four detectors.

The resolution of the silicon detectors was the best achieved so far amongst current radioxenon detection systems. The 129 keV conversion electron had a resolution of 16.66% in silicon1 and 16.87% in silicon2.

The MDC values of the new PIPSBox/CZT detection system were found to be 0.25 mBq/m³ for ^{131m}Xe, 0.26 mBq/m³ for ^{133m}Xe, 0.39 mBq/m³ for ¹³³Xe, and 0.72 mBq/m³ for ¹³⁵Xe. All values meet the 1 mBq/m³ requirement set by CTBTO. Simulation results showed that the MDC values can be improved by coupling the PIPSBox with bigger area CZT detector equal to the silicon areas. This increased the coincidence detection efficiency of the system, which reduced the MDC values for all four radioxenons.

The coincidence module used with DPP8 has some issues that need to be resolved before the system is ready to detect coincidence events from all four detectors. DPP8 also has some electrical noise issues that result in poorer resolution when compared to DPP2.

The PIPSBox/CZT radioxenon detection system is a great candidate to be installed at IMS stations because of its excellent energy resolution, low MDC values, minimal memory effect and potential higher air sampling frequency.

6. Future Work

This work is concluded with some of the work that needs to be done to improve upon this research. These suggestions will be completed in the next few months as the work continues on this new detection system.

6.1.1 Resolve Coincidence Module Issue with DPP8

The results obtained by DPP8 in radioxenon measurements did not show the expected signatures from all four radioxenons of interest. Gated beta and gamma spectra showed peaks of radiation quanta that are not emitted in coincidence. Even though the coincidence module passed all the tests to prove it is working properly, there must be some problem that is affecting coincidence measurements.

6.1.2 Electrical Noise Reduction for DPP8

Spectra generated from radioxenon measurements using DPP2 and DPP8 showed difference in resolution for energy peaks generated by the two processors. Since the detection system was the same, the difference in resolution should be due to the electrical noise in the baseline of DPP8 pulses. To resolve this problem, baseline root mean square (RMS) will be calculated for DPP8. Then, a series of steps will be taken to reduce the RMS value and increase the signal to noise ratio such as looking at the terraces on the ADC board and looking for ways to shield them from electromagnetic

noise and maybe replacing some components on the ADC board to reduce the noise associated with the signals.

6.1.3 Quantification of Memory Effect in the PIPSBox Gas Cell

Even though the memory effect is extremely minimized using a gas cell made of silicon detectors, it has to be quantified to figure the optimum time between measurements that would leave the least amount of memory in the gas.

6.1.4 Radioxenon Measurements in Real-Time Using DPP8

Once the last three steps are accomplished, the fourth and final step is to move the measurements and pulse processing to real-time inside the FPGA. This step will reduce the amount of dead-time and over all pulse processing time. There one disadvantage of using real-time measurements that is the FPGA will not be able to keep the pulse information as the case in off-line processing using MATLAB. The flip side to this disadvantage is that the FPGA is able to generate the 2-D spectra orders of magnitude faster than MATLAB processing, which allows for repeating experiments in the case of miss calibration or bad results in general.

7. Bibliography

- [1] “The Global Verification Regime and the International Monitoring System.” Preparatory Commission for the Comprehensive Nuclear-Test-Ban Treaty Organization (CTBTO), 2001.
- [2] C. T. B. Treaty, “Chairman’s Draft Text of the Comprehensive Test Ban Treaty,” *Arms Control Today*, 1996.
- [3] A. T. Farsoni, “Radioxenon Detection via Beta-Gamma Coincidence Technique,” presented at the Consortium for Verification Technology: Kick-Off Workshop, 16-17-2014.
- [4] CTBTO, “NOBLE GAS DETECTION SYSTEM REACHES MATURITY.”
- [5] A. Ringbom, T. Larson, A. Axelsson, K. Elmgren, and C. Johansson, “SAUNA—a system for automatic sampling, processing, and analysis of radioactive xenon,” *Nucl. Instrum. Methods Phys. Res. Sect. Accel. Spectrometers Detect. Assoc. Equip.*, vol. 508, no. 3, pp. 542–553, Aug. 2003.
- [6] V. V. Prelovskii, N. M. Kazarinov, A. Y. Donets, V. Y. Popov, I. Y. Popov, and N. V. Skirda, “The ARIX-03F mobile semiautomatic facility for measuring low concentrations of radioactive xenon isotopes in air and subsoil gas,” *Instrum. Exp. Tech.*, vol. 50, no. 3, pp. 393–397, May 2007.
- [7] J.-P. Fontaine, F. Pointurier, X. Blanchard, and T. Taffary, “Atmospheric xenon radioactive isotope monitoring,” *J. Environ. Radioact.*, vol. 72, no. 1–2, pp. 129–135, Jan. 2004.
- [8] G. Le Petit *et al.*, “Innovative concept for a major breakthrough in atmospheric radioactive xenon detection for nuclear explosion monitoring,” *J. Radioanal. Nucl. Chem.*, vol. 298, no. 2, pp. 1159–1169, Nov. 2013.
- [9] G. Le Petit *et al.*, “Spalax™ new generation: A sensitive and selective noble gas system for nuclear explosion monitoring,” *Appl. Radiat. Isot.*, vol. 103, pp. 102–114, Sep. 2015.
- [10] S. N. Kile, “Nuclear arms control and non-proliferation,” *SIPRI Yearb. 2004 Armaments Disarm. Int. Secur.*, pp. 617–619, 2011.
- [11] A. Becker, G. Wotawa, A. Ringbom, and P. R. J. Saey, “Backtracking of noble gas measurements taken in the aftermath of the announced October 2006 event in North Korea by means of the PTS methods in nuclear source estimation and reconstruction,” *Geophys. Res. Abstr.*, vol. 10, no. EGU200-A-11835, 2008.
- [12] G. Wotawa, “Meteorological analysis of the detection of xenon and barium/lanthanum isotopes in May 2010 in Eastern Asia,” *J. Radioanal. Nucl. Chem.*, vol. 44, no. 20, 2013.
- [13] A. Ringbom *et al.*, “Radioxenon detections in the CTBT international monitoring system likely related to the announced nuclear test in North Korea on February 12, 2013,” *J. Environ. Radioact.*, vol. 128, pp. 47–63, Feb. 2014.

- [14] C. M. Wright, "Low-Yield Nuclear Testing by North Korea in May 2010: Assessing the Evidence with Atmospheric Transport Models and Xenon Activity Calculations," *Sci. Glob. Secur.*, vol. 21, no. 1, pp. 3–52, Jan. 2013.
- [15] K. Kutsher, "Atmospheric Transport Modeling of Radio-Xenon Detections Possibly Related to the Announced Nuclear Test in North Korea on February 12, 2013," 2014.
- [16] L. Bläckberg *et al.*, "Memory effect, resolution, and efficiency measurements of an Al₂O₃ coated plastic scintillator used for radioxenon detection," *Nucl. Instrum. Methods Phys. Res. Sect. Accel. Spectrometers Detect. Assoc. Equip.*, vol. 714, pp. 128–135, Jun. 2013.
- [17] P. R. J. Saey *et al.*, "A long distance measurement of radioxenon in Yellowknife, Canada, in late October 2006," *Geophys. Res. Lett.*, vol. 34, no. 20, Oct. 2007.
- [18] A. Ringbom *et al.*, "Measurements of radioxenon in ground level air in South Korea following the claimed nuclear test in North Korea on October 9, 2006," *J. Radioanal. Nucl. Chem.*, vol. 282, no. 3, pp. 773–779, Dec. 2009.
- [19] K. Koch, W.-Y. Kim, P. G. Richards, and D. P. Schaff, "The Seismic Event in North Korea on 12 May 2010: an assessment from available seismological data," *Geophys. Res. Abstr.*
- [20] B. Orr, M. Schöppner, R. Tinker, and W. Plastino, "Detection of radioxenon in Darwin, Australia following the Fukushima Dai-ichi nuclear power plant accident," *J. Environ. Radioact.*, vol. 126, pp. 40–44, Dec. 2013.
- [21] W. Shilian *et al.*, "Radioxenon monitoring in Beijing following the Fukushima Daiichi NPP accident," *Appl. Radiat. Isot.*, vol. 81, pp. 344–347, Nov. 2013.
- [22] B. Alemayehu, A. T. Farsoni, L. Ranjbar, and E. M. Becker, "A well-type phoswich detector for nuclear explosion monitoring," *J. Radioanal. Nucl. Chem.*, vol. 301, no. 2, pp. 323–332, Aug. 2014.
- [23] A. T. Farsoni, D. M. Hamby, K. D. Ropon, and S. E. Jones, "A two-channel phoswich detector for dual and triple coincidence measurements of radioxenon isotopes," DTIC Document, 2007.
- [24] A. Farsoni and D. M. Hamby, "Characterizing a two-channel phoswich detector using radioxenon isotopes produced in the Oregon State University TRIGA reactor," presented at the 2010 Monitoring Research Review: Ground-Based Nuclear Explosion Monitoring Technologies, 2010.
- [25] A. T. Farsoni, D. M. Hamby, C. S. Lee, and A. J. Elliot, "Preliminary experiments with a triple-layer phoswich detector for radioxenon detection," DTIC Document, 2008.
- [26] A. T. Farsoni and D. M. Hamby, "Design and modeling of a Compton-suppressed phoswich detector for radioxenon monitoring," DTIC Document, 2010.
- [27] A. T. Farsoni, B. Alemayehu, A. Alhawsawi, and E. M. Becker, "A Phoswich Detector With Compton Suppression Capability for Radioxenon Measurements," *IEEE Trans. Nucl. Sci.*, vol. 60, no. 1, pp. 456–464, Feb. 2013.

- [28] A Farsoni, B. Alemayehu, A. Alhawsawi, and E. M. Becker, "A Compton-suppressed phoswich detector for gamma spectroscopy," *J. Radioanal. Nucl. Chem.*, vol. 296, no. 1, pp. 63–68, 2013.
- [29] A. T. Farsoni, B. Alemayehu, and A. M. Alhawsawi, "PRELIMINARY MEASUREMENTS WITH A COMPTON-SUPPRESSED PHOSWICH DETECTOR," *2011 Monit. Res. Rev. Ground-Based Nucl. Explos. Monit. Technol.*
- [30] L. Ranjbar, A. T. Farsoni, and E. M. Becker, "A CZT-based radioxenon detection system in support of the Comprehensive Nuclear-Test-Ban Treaty," *J. Radioanal. Nucl. Chem.*, pp. 1–10, 2016.
- [31] L. Ranjbar, A. T. Farsoni, and E. M. Becker, "Preliminary Measurements with a Two-element CZT-based Radioxenon Detector," *Nucl. Instrum. Methods Phys. Res. Sect. A*, vol. (Submitted), 2016.
- [32] "Types of Nuclear Weapons Tests," *ctbto.org*. [Online]. Available: <https://www.ctbto.org/nuclear-testing/history-of-nuclear-testing/types-of-nuclear-weapons-tests/>.
- [33] R. S. Norris and H. M. Kristensen, "Global Nuclear Weapons inventories, 1945-2010," *Bull. At. Sci.*, vol. 66, no. 4, 2010.
- [34] "U.S.-Russian Nuclear Arms Control Agreements at a Glance," *Arms Control Association*, Apr-2014. [Online]. Available: <https://www.armscontrol.org/factsheets/USRussiaNuclearAgreementsMarch2010>.
- [35] "Nuclear Weapons: Who Has What at a Glance," *Arms Control Association*, Jan-2017. [Online]. Available: <https://www.armscontrol.org/factsheets/Nuclearweaponswhohaswhat>.
- [36] "<https://www.ctbto.org/specials/who-we-are/>," Jan-2016. .
- [37] "http://www.bgr.bund.de/EN/Themen/Seismologie/_Content_alt/Kernwaffenteststopp_en_alt/kernwaffenteststopp_node_en.html."
- [38] B. Wernsperger and C. Schlosser, "Noble gas monitoring within the international monitoring system of the comprehensive nuclear test-ban treaty," *Radiat. Phys. Chem.*, vol. 71, no. 3–4, pp. 775–779, Oct. 2004.
- [39] M. Auer, T. Kumberg, H. Sartorius, B. Wernsperger, and C. Schlosser, "Ten Years of Development of Equipment for Measurement of Atmospheric Radioactive Xenon for the Verification of the CTBT," *Pure Appl. Geophys.*, vol. 167, no. 4–5, pp. 471–486, May 2010.
- [40] L. Ranjbar, "A Two-element CZT-based Radioxenon Detection System for Nuclear Weapon Test Monitoring," Oregon State University, 2016.
- [41] B. Bjurman *et al.*, "The detection of radioactive material from a venting underground nuclear explosion," *J. Environ. Radioact.*, vol. 11 (1), pp. 1–14, 1990.
- [42] "Evaluation and compilation of fission product yields." Los Alamos National Laboratory, LA-UR- 94-3106, ENDF-349, 1995.

- [43] “Preparatory commission for the comprehensive nuclear-test-ban treaty organization,” 2016. .
- [44] “WOSMIP III - Workshop on Signatures of Medical and Industrial Isotope Production.” Pacific Northwest National Laboratory (PNNL), 2012.
- [45] A. Matthias, “The International Monitoring System noble gas network.” CTBTO Preparatory Commission, 2014.
- [46] M. Schöppner, “Analysis of the Global Radioxenon Background with Atmospheric Transport Modelling for Nuclear Explosion Monitoring.”
- [47] R. W. Perkins and L. A. Casey, “Radioxenons: Their role in monitoring a comprehensive test ban treaty.” Pacific Northwest National Laboratory, 1996.
- [48] J. H. Ely, M. W. Cooper, J. C. Hayes, T. R. Heimbigner, J. I. McIntyre, and B. T. Schrom, “Final Technical Report on Radioxenon Event Analysis,” Pacific Northwest National Laboratory (PNNL), Richland, WA (US), 2013.
- [49] T. W. Bowyer *et al.*, “Elevated radioxenon detected remotely following the Fukushima nuclear accident,” *J. Environ. Radioact.*, vol. 102, no. 7, pp. 681–687, Jul. 2011.
- [50] F. Xie *et al.*, “Development of a radioxenon measurement system and its application in monitoring Fukushima nuclear accident,” *Radiat. Phys. Chem.*, vol. 97, pp. 85–89, Apr. 2014.
- [51] K. Kutsher, “Atmospheric transport modeling of radio-xenon detections possibly related to the announced nuclear test in North Korea on February 12, 2013,” in *Nuclear Forensics and Security meeting*, 2014.
- [52] T. W. Bowyer *et al.*, “Detection and analysis of xenon isotopes for the comprehensive nuclear-test-ban treaty international monitoring system,” *J. Environ. Radioact.*, vol. 59, pp. 139–151, 2002.
- [53] A. Ringbom, T. Larson, A. Axelsson, K. Elmgren, and C. Johansson, “SAUNA—a system for automatic sampling, processing, and analysis of radioactive xenon,” *Nucl. Instrum. Methods Phys. Res. Sect. Accel. Spectrometers Detect. Assoc. Equip.*, vol. 508, no. 3, pp. 542–553, Aug. 2003.
- [54] Y. V. Dubasov *et al.*, “The АРНКК-01 Automatic Facility for Measuring Concentrations of Radioactive Xenon Isotopes in the Atmosphere,” *Instrum. Exp. Tech.*, vol. 48 (3), pp. 373–379, 2005.
- [55] P. R. J. Saey and L.-E. De Geer, “Notes on radioxenon measurements for CTBT verification purposes,” *Appl. Radiat. Isot.*, vol. 63, no. 5–6, pp. 765–773, Nov. 2005.
- [56] L. Bläckberg *et al.*, “Investigations of surface coatings to reduce memory effect in plastic scintillator detectors used for radioxenon detection,” *Nucl. Instrum. Methods Phys. Res. Sect. Accel. Spectrometers Detect. Assoc. Equip.*, vol. 656, no. 1, pp. 84–91, Nov. 2011.
- [57] Y. S. Popov, N. M. Kazarinov, V. Y. Popov, Y. M. Rykov, and N. V. Skirda, “Measuring Low Activities of Fission-Product Xenon Isotopes Using the β - γ Coincidence Method,” *Instrum. Exp. Tech.*, vol. 48, no. 3, pp. 380–386, 2005.

- [58] J. I. McIntyre *et al.*, “Measurements of ambient radionuclide levels using the automated radionuclide sampler/analyzer (ARSA),” *J. Radioanal. Nucl. Chem.*, vol. 248, no. 3, pp. 629–635, 2001.
- [59] J. H. Ely, C. E. Aalseth, and J. I. McIntyre, “Novel beta-gamma coincidence measurements using phoswich detectors,” *J. Radioanal. Nucl. Chem.*, vol. 263, no. 1, pp. 245–250, 2005.
- [60] G. Le Petit, C. Jutier, P. Gross, and V. Greiner, “Low-level activity measurement of ^{131}Xe , ^{133}Xe , ^{135}Xe and ^{133}Xe in atmospheric air samples using high-resolution dual X- γ spectrometry,” *Appl. Radiat. Isot.*, vol. 64, no. 10–11, pp. 1307–1312, Oct. 2006.
- [61] W. Hennig, H. Tan, W. K. Warburton, and J. I. McIntyre, “Digital pulse shape analysis with phoswich detectors to simplify coincidence measurements of radioactive xenon,” *Proc. 27th Seism. Res. Rev. Ground-Based Nucl. Explos. Monit. Technol.*, pp. 787–794, 2005.
- [62] W. Hennig, Hui Tan, W. K. Warburton, and J. I. McIntyre, “Single-channel beta-gamma coincidence detection of radioactive xenon using digital pulse shape analysis of phoswich detector signals,” *IEEE Trans. Nucl. Sci.*, vol. 53, no. 2, pp. 620–624, Apr. 2006.
- [63] C. E. Cox *et al.*, “A 24-element Silicon PIN diode detector for high resolution radionuclide measurements using simultaneous X-ray and electron spectroscopy,” in *Nuclear Science Symposium and Medical Imaging Conference (NSS/MIC), 2013 IEEE*, 2013, pp. 1–7.
- [64] A. T. Farsoni and D. M. Hamby, “Study of a Tripple-Layer Phoswich Detector for Beta and Gamma Spectroscopy with Minimal Crosstalk,” *28th Seism. Res. Rev. Ground-Based Nucl. Explos. Monit. Technol.*
- [65] A. T. Farsoni and D. M. Hamby, “Characterization of a Tripple-Layer Phoswich Detector For Radionuclide Measurements,” *2009 Monit. Res. Rev. Ground-Based Nucl. Explos. Monit. Technol.*
- [66] L. Ranjbar, “A Two-element CZT-based Radionuclide Detection System for Nuclear Weapon Test Monitoring.”
- [67] S. Czyz, “A Compact Radionuclide Detection System Using CZT, an Array of SiPMs, and a Plastic Scintillator,” Oregon State University, 2016.
- [68] “PIPS Detectors Data Sheet and Specifications.” Canberra, Jun-2017.
- [69] M. Foxe, J. Hayes, M. Mayer, J. McIntyre, C. Sivals, and R. Suarez, “Characterization of a Commercial Silicon Beta Cell,” Pacific Northwest National Laboratory (PNNL), Richland, WA (US), PNNL-25297, Mar. 2016.
- [70] G. Knoll, *Radiation Detection and Measurement*, 4th ed. John Wiley and Sons, 2010.
- [71] Z. Huaiqiang, G. Liangquan, T. Bin, and L. Tingli, “Optimal choice of trapezoidal shaping parameters in digital nuclear spectrometer system,” *Nucl. Sci. Tech.*, vol. 6, pp. 109–114, 2013.
- [72] P. N. Luke, “Single-polarity charge sensing in ionization detectors using coplanar electrodes,” *Appl. Phys. Lett.*, vol. 65, no. 22, p. 2884, 1994.

- [73] P. N. Luke, "Unipolar charge sensing with coplanar electrodes-application to semiconductor detectors," *Nucl. Sci. IEEE Trans. On*, vol. 42, no. 4, pp. 207–213, 1995.
- [74] J. Schulze, M. Auer, and R. Werzi, "Low level radioactivity measurement in support of the CTBTO," *Appl. Radiat. Isot.*, vol. 53, no. 1, pp. 23–30, 2000.
- [75] J. I. McIntyre, T. W. Bowyer, and P. L. Reeder, *Calculation of minimum detectable concentration levels of radioxenon isotopes using the PNNL ARSA system*. Pacific Northwest National Laboratory, 2006.
- [76] L. Ranjbar, E. M. Becker, and A. Farsoni, "135Xe Measurements With a Two-Element CZT-based Radioxenon Detector for Nuclear Explosion Monitoring."
- [77] W. Hennig *et al.*, "Study of silicon detectors for high-resolution radioxenon measurements," *Nucl. Instrum. Methods Phys. Res. A*, vol. 652, pp. 216–220, 2011.

8. Appendices

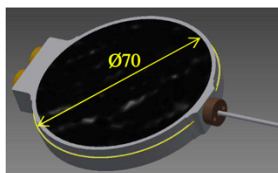
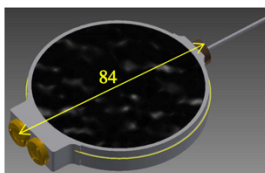
8.1 PIPSBox Specification Sheet



PIPS specification sheet

Series CD

Model: PIPSBOX-2x1200-500A



Assembly:	<i>2 detectors mounted in a low background housing covered by a carbon window</i>	
Total dimensions (LxWxH):	84 x 70 x 12	mm
Active volume between 2 detectors:	10.6	cm ³
Connectors in assembly:	LEMO EWV.00.250.NTLPV	
Fitting connectors:	LEMO FFA.00.250.CTAC22	
Tubing:	Inox 316L – id: 0.75 – od: 1.59	mm
Vacuum tightness (leak rate):	10E-10	mbar.l/s
Contact to junction:	wire bonding	
Active Area:	2 x 1200	mm ²
Detector model:	2 x PD1200-26-500	
Chip thickness:	2 x 500	µm
Depletion depth (min./max.):	475 / 515	µm
Junction window thickness:	< 50	nm
Ohmic window thickness:	< 1500	nm
Operating temperature:	-20 / +40	°C
Storage temperature:	-20 / +100	°C
Capacitance (typ.):	294	pF

Estimated detector performance:

	<i>min.</i>	<i>max.</i>	
Operating voltage:	100	150	Volts
Total current at 20°C (per detector):		50	nA
Electronic resolution (per detector):		12	keV at 2µs shaping time

- Standard tests are performed following IEEE Standard Test Procedures for Semiconductor Charged Particle Detectors No IEEE Std 300-1988.
- The electronic noise is approximated with a pulser resolution.

SSPOR074/A

CANBERRA Industries, 800 Research Parkway, Meriden, CT 06450, USA, Tel. (203) 238-2351; Fax. (203) 235-1347; <http://www.canberra.com>
 CANBERRA Semiconductor, N.V. Lanmerdries 25, 2250 Olen, Belgium, Tel. (32-14) 221975; Fax. (32-14) 221991; E-mail: csnv@canberra.com

8.2 PIPSBox with LEMO/BNC Cables



8.3 PIPSBox Gas Tube Connections



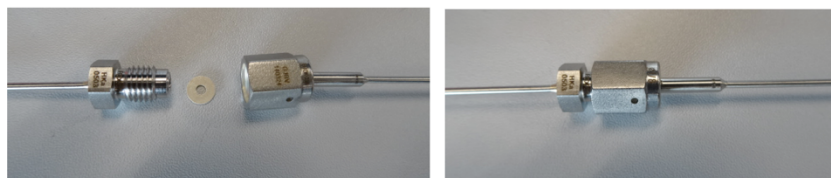
CUSTOM DESIGN PIPS DETECTORS

Model: PIPSBOX-2x1200-500A



ALWAYS WEAR GLOVES BEFORE HANDLING THE DETECTORS

Connection scheme gas tubing:



Male nut mounted over the gland Male nut screwed into female nut

Assembly:

1. Weld 1/8" SS tubing onto the gland (SS-G-FR2-TB2)
2. Mount gasket (SS-GT-FR2)
3. Mount Male nut (SS-MN-FR2) over the gland and screw into female nut of the PIPSBOX